



저작자표시-비영리-변경금지 2.0 대한민국

이용자는 아래의 조건을 따르는 경우에 한하여 자유롭게

- 이 저작물을 복제, 배포, 전송, 전시, 공연 및 방송할 수 있습니다.

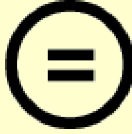
다음과 같은 조건을 따라야 합니다:



저작자표시. 귀하는 원저작자를 표시하여야 합니다.



비영리. 귀하는 이 저작물을 영리 목적으로 이용할 수 없습니다.



변경금지. 귀하는 이 저작물을 개작, 변형 또는 가공할 수 없습니다.

- 귀하는, 이 저작물의 재이용이나 배포의 경우, 이 저작물에 적용된 이용허락조건을 명확하게 나타내어야 합니다.
- 저작권자로부터 별도의 허가를 받으면 이러한 조건들은 적용되지 않습니다.

저작권법에 따른 이용자의 권리는 위의 내용에 의하여 영향을 받지 않습니다.

이것은 [이용허락규약\(Legal Code\)](#)을 이해하기 쉽게 요약한 것입니다.

[Disclaimer](#)

Doctoral Thesis

Doping engineering of hematite photoanodes by
controlling Sn diffusion for efficient
photoelectrochemical water splitting

Juhyung Park

School of Energy and Chemical Engineering
(Energy Engineering)

Ulsan National Institute of Science and Technology

2023

Doping engineering of hematite photoanodes by
controlling Sn diffusion for efficient
photoelectrochemical water splitting

Juhyung Park

School of Energy and Chemical Engineering
(Energy Engineering)

Ulsan National Institute of Science and Technology

Doping engineering of hematite photoanodes by controlling Sn diffusion for efficient photoelectrochemical water splitting

A thesis/dissertation submitted to
Ulsan National Institute of Science and Technology
in partial fulfillment of the
requirements for the degree of
Doctor of Philosophy

Juhyung Park

06.08.2023 of submission

Approved by

Advisor

Ji-Hyun Jang

Doping engineering of hematite photoanodes by controlling Sn diffusion for efficient photoelectrochemical water splitting

Juhyung Park

This certifies that the thesis/dissertation of Juhyung Park is approved.

06.08.2023 of submission

Signature

Advisor: Ji-Hyun Jang

Signature

Jin Young Kim

Signature

Jongnam Park

Signature

Jungki Ryu

Signature

Ji-Wook Jang

Abstract

Photoelectrochemical (PEC) water splitting is a promising approach for sustainable hydrogen production, utilizing solar energy. This process involves converting water into hydrogen and oxygen gases through the generation of electron-hole pairs. Hematite ($\alpha\text{-Fe}_2\text{O}_3$) has been received significant attention for its low cost, high stability, and unique electrochemical properties, making it a desirable semiconductor for PEC water splitting system. However, due to its low electrical conductivity and poor oxygen evolution reaction (OER) kinetics, the practical solar-to-hydrogen (STH) conversion efficiency is lower than the theoretical maximum value ($\sim 15\%$). Thus, improving the electronic properties of hematite is crucial to achieving higher STH conversion efficiency.

This dissertation focuses on the development of hematite through doping engineering, specifically by controlling the diffusion of Sn from the fluorine-doped tin oxide (FTO) substrate. The diffused Sn can act as an n-type dopant, introducing additional charge carriers and enhancing electron and hole transport within the hematite lattice. However, an excessive amount of Sn can cause lattice distortion due to its larger ionic size compared to Fe, and lead to the formation of additional energy levels between the conduction and valence bands, thereby acting as charge recombination centers.

In chapter 2, the negative effects of excess Sn on hematite are discussed. Initially, thin film hematite was fabricated for applications such as dual photoanodes and photoanode/solar cells. However, the thin film hematite exhibited lower PEC efficiency compared to the reference thick film, primarily due to the excessive amount of Sn. To maintain the benefits of Sn while mitigating its negative effects, precise control of Sn was achieved through non-metallic Si doping. The controlled Sn and Si co-doped thin film hematite exhibited improved PEC activity due to enhanced carrier concentration and electronic properties. Furthermore, the surface OER kinetics of hematite was accelerated by depositing a co-catalyst of NiFeO_x and highly efficient unbiased photoelectrochemical water splitting system was achieved by designing a tandem cell consisted of dual photoanode and perovskite solar cell.

In chapter 3, we focus on identifying the optimal dopant between Sn and Si for hematite. Based on the results from chapter 2, it was observed that Sn and Si co-doped hematite demonstrated higher efficiency compared to excess Sn-doped hematite. To determine which dopant, Sn or Si, exhibited superior catalytic activity, additional control of Sn was conducted. Since both Sn and Si diffuse into the hematite lattice through thermal annealing conditions, the Sn diffusion was controlled by adjusting the thermal annealing parameters. The results confirmed that hematite with a higher Si content exhibited better PEC performance, attributed to improved electronic properties at the surface, highlighting the superior catalytic activity of Si compared to Sn. Additionally, the potential use of hematite as an OER electrode in Zn-air batteries was investigated. Hematite exhibited significantly reduced charging potential

compared to the novel metal electrode (Ir/C), confirming its potential as an efficient OER electrode in Zn-air batteries.

In chapter 4, the research focuses on the design of co-catalysts on the surface of hematite. In addition to the poor electronic properties of hematite, limited hole transfer to the electrolyte is a major challenge for achieving high PEC efficiency. To overcome these challenges, oxygen evolution reaction OER co-catalysts are commonly employed. In this dissertation, we conducted research on 2D MXene sheets as potential co-catalysts for PEC systems, exploiting their high electrical properties and large functional groups. However, the practical utilization of 2D MXene sheets has been impeded by their high reactivity and structural mismatch with hematite, which is typically fabricated as 1D or 3D. To address this structural mismatch, we synthesized 0D nanofragmented MXene (NFMX) using a centrifuge-assisted method. Additionally, we resolved the high reactivity of NFMX by depositing a thin overlayer of NiFe(OH)_x . Through this co-catalyst design, we demonstrated the potential of composite co-catalyst design, integrating the exceptional electrical properties of previously challenging-to-use 2D materials, to enhance PEC performance. It provides valuable insights into the promising role of 2D materials with superior electrical characteristics as PEC catalysts.

I believe that the results and discussions presented in this dissertation can pave the way for enhancing the PEC efficiency of hematite and exploring its potential for various applications.

Table of Contents

Abstract.....	I
Table of Contents	IV
List of Figures	VI
List of Tables	XII
Chapter 1. Introduction	1
1.1 Climate change and green hydrogen.....	1
1.2 Photoelectrochemical water splitting metal oxide photoanode materials.....	6
1.3 Hematite ($\alpha\text{-Fe}_2\text{O}_3$) and research progress.....	10
1.4 Research outline	15
1.5 References.....	17
Chapter 2. A Highly Transparent Thin Film Hematite with Multi-Element Dopability for an Efficient Unassisted Water Splitting System	19
2.1 Introduction	19
2.2 Experimental section	21
2.3 Results and discussion.....	23
2.3.1 Hematite photoanode and PSC tandem cells	23
2.3.2 PEC activities of $\text{Ti-Fe}_2\text{O}_3(\text{t})$ vs. $\text{Ti-Fe}_2\text{O}_3(\text{T})$.....	24
2.3.3 Non-metallic Si doping effect on $\text{Ti-Fe}_2\text{O}_3(\text{t})$.....	25
2.3.4 PEC activities of $\text{NiFeO}_x@ \text{Ti:Si-Fe}_2\text{O}_3(\text{t})$.....	26
2.3.5 Dual $\text{NiFeO}_x@ \text{Ti:Si-Fe}_2\text{O}_3(\text{t})/\text{PSC}$ tandem cell	27
2.4 Conclusion	47
2.5 References.....	48
Chapter 3. Sn-Controlled Co-Doped Hematite for Efficient Solar-Assisted Chargeable Zn–Air Batteries	51

3.1 Introduction	51
3.2 Experimental section	52
3.3 Results and discussion.....	54
3.3.1 Sn and Si diffusion trends of Sn:Si-Fe₂O₃/1-/2	54
3.3.2 Sn and Si content and morphological features of Sn:Si-Fe₂O₃/1-/2.....	54
3.3.3 PEC activities of Sn:Si-Fe₂O₃/1-/2	56
3.3.4 Solar-assisted zinc-air battery assembled with hematite photoanode.....	56
3.4 Conclusion	70
3.5 References	71
Chapter 4. Boosting Charge Transfer Efficiency by Nanofragment MXene for Efficient Photoelectrochemical Water Splitting of NiFe(OH)_x Co-Catalyzed Hematite	74
4.1 Introduction	74
4.2 Experimental section	76
4.3 Results and discussion.....	78
4.3.1 Fabrication process and morphology of NFMX/Fe₂O₃.....	78
4.3.2 PEC activities of NFMX/Fe₂O₃.....	80
4.3.3 PEC activities of NiFe(OH)_x/NFMX/Fe₂O₃.....	81
4.4 Conclusion	101
4.5 References	102
Acknowledgements.....	106

List of Figures

Figure 1-1. Global surface temperature change in the last 50 years and global surface temperature change by human and natural drivers.

Figure 1-2. (a) The physical drives of climate change and (b) environmental phenomena caused by climate change.

Figure 1-3. Three types of hydrogen: grey, blue, and green hydrogen.

Figure 1-4. (a) The many uses of green hydrogen and (b) clean hydrogen projects and investment in 2021.

Figure 1-5. The production cost of green and blue hydrogen (\$/kg) from 2019 to 2050.

Figure 1-6. Schematic illustrations and charge flow routes of (a) PC, (b) PEC, and (c) PV-EC systems.

Figure 1-7. Schematic illustration of PEC water splitting system.

Figure 1-8. (a) Reported photocurrent density at 1.23 V_{RHE} and (b) theoretical photocurrent density and STH efficiency of metal oxide photoanode materials.

Figure 1-9. Energy band position of metal oxide photoanode materials.

Figure 1-10. Morphology engineering of hematite. (a) SEM images and corresponding schematic illustrations and (b) photocurrent density at 1.23 V vs. RHE of hematite nanostructures (B: Bulk, D: Dendrites, NP: Nanoparticles, MP: Mesoporous, NR: Nanorods, NW: Nanowires, NS: Nanosheets, NT: Nanotubes, NC: Nanocones, and CF: Cauliflower).

Figure 1-11. Surface modifications on hematite. Band structure of an (a) n-type semiconductor photoanode, (b) n-type semiconductor photoanode with co-catalyst, and (c) n-type semiconductor photoanode with surface passivation layer with an electrolyte. (d) J-V curves of Co-Pi/Fe₂O₃ and Fe₂O₃ under 1 SUN and dark conditions. (e) J-V curves of Fe₂O₃ (black), Al₂O₃/Fe₂O₃ (blue), and Co/Al₂O₃/Fe₂O₃ under 1 SUN and dark conditions.

Figure 2-1. Hematite photoanode and PSC tandem cells. (a) SEM images of Ti-Fe₂O₃(t) and Ti-Fe₂O₃(T) (left) and scheme for hematite/PSC tandem cell (right). (b) EQE of PSC and PSC behind hematite photoanodes (Ti-Fe₂O₃(t)/PSC and Ti-Fe₂O₃(T)/PSC). (c) J-V curves of PSC and hematite

photoanodes together under light illumination.

Figure 2-2. UV-Vis spectra of (a) PSC and (b) Ti-Fe₂O₃(T) and Ti-Fe₂O₃(t).

Figure 2-3. Top and cross-section SEM images of Ti-Fe₂O₃#1 to Ti-Fe₂O₃#5 (a:Ti-Fe₂O₃#1 b: Ti-Fe₂O₃#2 c: Ti-Fe₂O₃#3 d: Ti-Fe₂O₃#4 e: Ti-Fe₂O₃#5. Ti-Fe₂O₃#1-#5).

Figure 2-4. (a) Current density at 1.23 V_{RHE} and maximum transmittance at 400 nm for different thicknesses. (b) J-V curves, (c) UV-Vis absorption spectra, and (d) Transmittance (%) of Ti-Fe₂O₃#1 to #5.

Figure 2-5. Tauc plot of (a) Ti-Fe₂O₃(T) and (b) Ti-Fe₂O₃(t).

Figure 2-6. (a) J-V curves and (b) photovoltaic parameters of PSC and PSCs behind hematite photoanodes.

Figure 2-7. PEC activities of Ti-Fe₂O₃(T) and Ti-Fe₂O₃(t). (a) J-V curves under light and dark conditions, XPS spectra of (b) Ti 2*p* and (c) Sn 3*d*, (d) schematics of the Sn and Ti content, and charge separation efficiencies at the (e) surface region (η_{surface}) and (f) bulk region (η_{bulk}) of Ti-Fe₂O₃(T) and Ti-Fe₂O₃(t).

Figure 2-8. (a) TOF-SIMS depth profiles and (b) TOF-SIMS 3D images of Sn (TOF-SIMS etching rate: ~0.6 nm/s).

Figure 2-9. J-V curves under the front and back light conditions of (a) Ti-Fe₂O₃(T) and (b) Ti-Fe₂O₃(t).

Figure 2-10. Comparison of electrochemical properties of Ti-Fe₂O₃(t) with different Sn content. (a) UV-Vis absorption spectra, (b) XPS spectra of Sn 3*d*, (c) J-V curves, (d) close-up data in the rectangular region in **Figure 2-10c**, and charge separation efficiencies at the (e) surface region (η_{surface}) and (f) bulk region (η_{bulk}) of Ti-Fe₂O₃(t) with different Sn/Fe ratio.

Figure 2-11. (a) Schematics of atomic distribution, XPS spectra of (b) Si 2*p*, (c) Ti 2*p*, (d) Sn 3*d*, and (e) Fe 2*p*, (f) transient photocurrent density curves, and (g) Mott-Schottky plots of Ti-Fe₂O₃(t) and Ti-Fe₂O₃(T).

Figure 2-12. (a) XRD and (b) Raman spectra of Ti-Fe₂O₃(t) and Ti:Si-Fe₂O₃(t).

Figure 2-13. XPS depth profile of Ti:Si-Fe₂O₃(t) after removing SiO_x overlayer.

Figure 2-14. (a-b) VBM and (c-d) Tauc plot of Ti-Fe₂O₃(t) and Ti:Si-Fe₂O₃(t).

Figure 2-15. Schematic energy diagram of Ti-Fe₂O₃(t) and Ti:Si-Fe₂O₃(t).

Figure 2-16. PEC activities after non-metallic Si doping and NiFeO_x deposition on Ti-Fe₂O₃(t). (a) J-V curves under light and dark conditions, TEM images of (b) Ti:Si-Fe₂O₃(t) (left) and NiFeO_x@Ti:Si-Fe₂O₃(t) (right) (inset images show the low magnification TEM images of each sample), charge separation efficiencies at the (c) surface region (η_{surface}) and (d) bulk region (η_{bulk}), (e) EIS spectra at 1.23 V_{RHE}, and (f) IPCE spectra at 1.23 V_{RHE} of Ti-Fe₂O₃(t), Ti:Si-Fe₂O₃(t), and NiFeO_x@Ti:Si-Fe₂O₃(t). (g) J-V curves, (h) J-t measurement at 1.23 V_{RHE} during 8 h of single and dual NiFeO_x@Ti:Si-Fe₂O₃(t).

Figure 2-17. J-V curves of NiFeO_x@Ti:Si-Fe₂O₃(t) with different dilution concentration of NiFeO_x (dilution X2 = pristine NiFeO_x solution : hexane = 1:1 (v:v), dilution X4 = NiFeO_x dilution X2 solution : hexane = 1:1 (v:v))

Figure 2-18. J-V curves of Ti:Si-Fe₂O₃(t) with (a) different concentration and (b) dip coating time of APTMS (Si precursor) solution. (c) EIS spectra and (d) transient photocurrent density curves at 1.23 V_{RHE} of optimized hematite photoanodes at separate conditions.

Figure 2-19. Top and cross-section SEM images of (a₁-a₂) Ti:Si-Fe₂O₃(t) and (b₁-b₂) NiFeO_x@Ti:Si-Fe₂O₃(t).

Figure 2-20. HAADF-STEM and EDS elemental mapping images of NiFeO_x@Ti:Si-Fe₂O₃(t)

Figure 2-21. UV-Vis absorption spectra of Ti-Fe₂O₃(t), Ti:Si-Fe₂O₃(t), and NiFeO_x@Ti:Si-Fe₂O₃(t) .

Figure 2-22. XPS spectra (a) Fe 2p, (b) O 1s, (c) Ni 2p, and (d) Ti 2p of NiFeO_x@Ti:Si-Fe₂O₃(t).

Figure 2-23. (a) UV-Vis absorption spectra and (b) digital images of Ti-Fe₂O₃(T), single and dual NiFeO_x@Ti:Si-Fe₂O₃(t).

Figure 2-24. Dual NiFeO_x@Ti:Si-Fe₂O₃(t)/PSC tandem cell. (a) Scheme for the tandem cell configuration, (b) J-V curves of PSC and single and dual NiFeO_x@Ti:Si-Fe₂O₃(t) together under light illumination, (c) J-t measurements curves and STH conversion efficiencies of the tandem cells (dotted line: 2-electrode system; solid line: 3-electrode system at 0 V_{RHE}). (d) Faradaic efficiency and the amount of H₂ and O₂ gases for 3 h of assembled dual NiFeO_x@Ti:Si-Fe₂O₃(t).

Figure 3-1. Content and diffusion trends of Sn and Si in Sn:Si-Fe₂O₃/1-2. (a) Schematic illustration of fabrication procedures and Sn and Si diffusion trends of Sn:Si-Fe₂O₃/1-2. XPS depth profiles of (b) Sn and (c) Si. (d) TOF-SIMS 3d images of Sn and Si. (e) EDS line-scanning data of Sn and Si.

Figure 3-2. Schematic illustration of fabrication procedures of Sn-Fe₂O₃/1-2.

Figure 3-3. (a) XPS and (b) TOF-SIMS depth profiles of Ti in Sn:Si-Fe₂O₃/1-2 (TOF SIMS etching rate: ~ 0.6 nm/s).

Figure 3-4. J-V curves with various annealing step and repetition number annealed (a) at 800 °C for 5 min, (b) at 800 °C for 10min, and (c) at 800 °C for 20 min of Sn:Si-Fe₂O₃. (d) Current density at 1.23 V_{RHE} according to different annealing number.

Figure 3-5. J-V curves of (a) Fe₂O₃/1-2 and Sn:Si-Fe₂O₃/1-2 annealed at 600 °C and 700 °C.

Figure 3-6. TOF-SIMS depth profiles of Si (TOF-SIMS etching rate: ~ 0.6 nm/s).

Figure 3-7. Morphological features of Sn:Si-Fe₂O₃/1-2. (a-b) SEM images. (c) HRTEM image, (c-I) close-up image of **Figure 3-7c** in the rectangular region, and (c-II) EDS mapping images of Sn:Si-Fe₂O₃/1. (d) HRTEM image, (d-I) close-up image of **Figure 3-7d** in the rectangular region, and (d-II) EDS mapping images of Sn:Si-Fe₂O₃/2. (e) Fe-K edge XANES spectra. (f) Fourier transformations of Fe K-edge EXAFS. and (g) XPS spectra of Fe 2p.

Figure 3-8. Cross-section SEM images of (a) Sn:Si-Fe₂O₃/1 and (b) Sn:Si-Fe₂O₃/2.

Figure 3-9. TEM images of (a1-a2) Sn:Si-Fe₂O₃/1 and (b1-b2) Sn:Si-Fe₂O₃/2.

Figure 3-10. (a) XRD patterns and (b) Raman spectra of Sn-Fe₂O₃/1-2 and Sn:Si-Fe₂O₃/1-2.

Figure 3-11. (a) Fe-K edge XANES and (b) Fourier transformations of Fe K-edge EXAFS spectra of Sn-Fe₂O₃/1.

Figure 3-12. XPS (a) O 1s, (b) Sn 3d, and (c) Si 2p spectra of Sn:Si-Fe₂O₃/1-2.

Figure 3-13. PEC activities of Sn:Si-Fe₂O₃/1-2. (a) J-V curves. (b) EIS spectra at 1.23 V_{RHE}. (c) Surface charge separation efficiencies (η_{surface}). (d) Transient photocurrent density at 1.23 V_{RHE}. (e) ECSA values with different scan rates. (f) Mott-Schottky plots under dark condition. (g) J-V curves, (h) J-t measurements during 20 hours at 1.23 V_{RHE}, and (i) IPCE spectra of Sn:Si-Fe₂O₃/2 and NiFe(OH)_x@Sn:Si-Fe₂O₃/2.

Figure 3-14. PEC activities of Sn-Fe₂O₃/1-/2. (a) J-V curves. (b) EIS spectra at 1.23 V_{RHE}. (c) Surface charge separation efficiencies (η_{surface}). (d) Transient photocurrent density at 1.23 V_{RHE}.

Figure 3-15. Four-point probe sheet resistance of FTO with different annealing conditions at 800 °C.

Figure 3-16. ABPE curve of Sn:Si-Fe₂O₃/2 and NiFe(OH)_x@Sn:Si-Fe₂O₃/2.

Figure 3-17. J-V curves of (a) Sn:B-Fe₂O₃/1-/2, (b) Sn:Ge-Fe₂O₃/1-/2, and (c) Sn:Ti-Fe₂O₃/1-/2.

Figure 3-18. SEM images of (a₁-a₂) Sn:B-Fe₂O₃/1-/2, (b₁-b₂) Sn:Ge-Fe₂O₃/1-/2, and (c₁-c₂) Sn:Ti-Fe₂O₃/1-/2.

Figure 3-19. Solar-assisted zinc-air battery assembled with hematite photoelectrode. Schematic illustration of (a) zinc-air battery assembled by Ir/C and Pt/C, and (b) solar-assisted zinc-air battery assembled by Fe₂O₃ and Pt/C. Cycling performance of the (c) zinc-air battery with Ir/C and (d) solar-assisted zinc-air battery with Sn:Si-Fe₂O₃/2 under illumination for 20 hours. (e) Voltage gap of the zinc-air batteries with Ir/C and with Sn:Si-Fe₂O₃/2 at the first and last cycles for 20 hours (Electrolyte: 6 M KOH).

Figure 3-20. Cycling performance of zinc-air battery with Sn:Si-Fe₂O₃/2 in the dark condition (Electrolyte: 6 M KOH).

Figure 4-1. Fabrication process and morphology of NFMX/Fe₂O₃. (a) Fabrication process of NFMX/Fe₂O₃. SEM images of (b) MAX, (c) MXene sheets, (d) α -Fe₂O₃, and (e) NFMX/Fe₂O₃. TEM images of (f) α -Fe₂O₃, and (g) NFMX/Fe₂O₃ (the inset image shows the IFFT image of the selected area of **Figure 4-1g**). (h) HAADF-STEM-EDS mapping images of each element of NFMX/Fe₂O₃.

Figure 4-2. DLS measurement of an optimized NFMX solution.

Figure 4-3. TEM images of NFMX.

Figure 4-4. Fabrication methods of NFMX/Fe₂O₃. (a) Centrifuge coating method and (b) dip coating method. (c) SEM image of MXene sheet/Fe₂O₃. (d) J-V curves of α -Fe₂O₃ and MXene sheet/Fe₂O₃.

Figure 4-5. (a) TEM image, and (b) IFFT image of NFMX/Fe₂O₃.

Figure 4-6. XPS atomic percentage of (a) α -Fe₂O₃ and (b) NFMX/Fe₂O₃.

Figure 4-7. UV-Vis absorption spectra of α -Fe₂O₃ and NFMX/Fe₂O₃.

Figure 4-8. Characterization of NFMX/Fe₂O₃. (a) XRD patterns of α -Fe₂O₃ and NFMX/Fe₂O₃. XPS O 1s spectra of (b) α -Fe₂O₃ and (c) NFMX/Fe₂O₃. (d) XPS Ti 2p spectra of NFMX/Fe₂O₃. (e) FT-IR spectrum of MXene. (f) Fourier transformations of Fe K-edge EXAFS spectra of α -Fe₂O₃ and NFMX/Fe₂O₃.

Figure 4-9. (a) Raman spectra and (b) close-up image of the selected area in **Figure 4-9a**.

Figure 4-10. XPS Ti 2p spectrum of α -Fe₂O₃.

Figure 4-11. XPS spectra of (a) C 1s, and (b) F 1s of NFMX.

Figure 4-12. Fe-K edge XANES spectra of α -Fe₂O₃, and NFMX/Fe₂O₃.

Figure 4-13. Zeta potential of α -Fe₂O₃, NFMX/Fe₂O₃, and NFMX.

Figure 4-14. PEC activities of NFMX/Fe₂O₃. (a) J-V curves under 1 SUN and dark conditions. Charge separation efficiencies at the (b) bulk (η_{bulk}), and (c) surface (η_{surface}) region of α -Fe₂O₃ and NFMX/Fe₂O₃.

Figure 4-15. J-V curves of α -Fe₂O₃ and MQD/Fe₂O₃.

Figure 4-16. J-V curves of α -Fe₂O₃ and NFMX/Fe₂O₃ with 1.0 M NaOH (solid line) and with a solution mixture of 1.0 M NaOH and 0.2 M Na₂SO₃ (dotted lines).

Figure 4-17. PEC activities of NFMX/Fe₂O₃. (a) EIS measurements at 1.23 V_{RHE} (inset image shows the circuit model), (b) R_{trap}, (c) R_{ct}, (d) N_{ss} at different applied potentials under 1 SUN, (e) Mott-Schottky plots under dark condition, and (f) ECSA curves of α -Fe₂O₃, and NFMX/Fe₂O₃.

Figure 4-18. (a) Four-point-probe measurements, and (b) I-V characteristics of α -Fe₂O₃, and NFMX/Fe₂O₃.

Figure 4-19. (a) Fabrication procedure of MXene and electronic structure. (b) UPS of NFMX, and α -Fe₂O₃ under dry and wet surface conditions. Schematics of (c) Ohmic contact and (d) Schottky contact of NFMX/Fe₂O₃.

Figure 4-20. C_{trap} at different applied potentials.

Figure 4-21. (a) OCP measurements, (b) transient photocurrent density curves at 1.23 V_{RHE}, (c) cathodic photocurrent density at 1.23 V_{RHE} after instantaneous light-off condition, and (d) retention (%) of photocurrent density at 1.23 V_{RHE} for 120 minutes of α -Fe₂O₃ and NFMX/Fe₂O₃.

Figure 4-22. CV curves at 100 mV/s scan rate of (a) α -Fe₂O₃ and (b) NFMX/Fe₂O₃.

Figure 4-23. PEC activities of NiFe(OH)_x/NFMX/Fe₂O₃. (a) PEC reaction process of α -Fe₂O₃, NiFe(OH)_x/Fe₂O₃, and NiFe(OH)_x/NFMX/Fe₂O₃ (red arrow: surface charge transfer rate to the electrolyte, blue arrow: bulk charge transport rate, the thickness of each arrow illustrates the intensity of each process). TEM images of (b) NiFe(OH)_x/Fe₂O₃ and (c) NiFe(OH)_x/NFMX/Fe₂O₃. (d) J-V curves under 1 SUN and dark conditions. (e) J-t measurement for 60 hours, and (f) Evolved gases and faradaic efficiency for 120 minutes of NiFe(OH)_x/NFMX/Fe₂O₃ at 1.23 V_{RHE}.

Figure 4-24. UV-Vis absorption spectra of NFMX/Fe₂O₃, and NiFe(OH)_x/NFMX/Fe₂O₃.

Figure 4-25. XPS spectra of (a) Fe 2*p*, (b) O 1*s*, and (c) Ni 2*p* of NFMX/Fe₂O₃ and NiFe(OH)_x/NFMX/Fe₂O₃.

Figure 4-26. (a) J-V curves of NiFe(OH)_x/NFMX/Fe₂O₃ with 1.0 M NaOH (solid line) and with a solution mixture of 1.0 M NaOH and 0.2 M Na₂SO₃ (dotted lines), charge separation efficiencies at the (b) bulk (η_{bulk}), and (c) surface (η_{surface}) region of NiFe(OH)_x/NFMX/Fe₂O₃.

Figure 4-27. (a) J-V curves and (b) onset potential (determined at 0.2 mA cm⁻² from **Figure 4-27a**) of α -Fe₂O₃, NiFe(OH)_x/Fe₂O₃, and NiFe(OH)_x/NFMX/Fe₂O₃.

Figure 4-28. CV curves at 100 mV/s scan rate of (a) NiFe(OH)_x/Fe₂O₃ and (b) NiFe(OH)_x/NFMX/Fe₂O₃.

Figure 4-29. IPCE spectra of α -Fe₂O₃ and NiFe(OH)_x/NFMX/Fe₂O₃ at 1.23 V_{RHE}.

List of Tables

Table 1-1. Advantages and disadvantages of metal oxide photoanode materials for PEC water oxidation.

Table 1-2. Electrical properties of metal oxide photoanode materials.

Table 2-1. PEC performance comparison table of thin film hematite photoanodes under 100 nm.

Table 2-2. EIS values of Ti-Fe₂O₃(T), Ti-Fe₂O₃(t), Ti:Si-Fe₂O₃(t) and NiFeO_x@Ti:Si-Fe₂O₃(t).

Table 2-3. Tandem cell performance comparison table of hematite/PSC tandem cells.

Table 4-1. PEC performance comparison table on hematite-based photoanodes with co-catalyst. The photocurrent density was confirmed at 1.23 V_{RHE}.

Chapter 1. Introduction

1.1 Climate change and green hydrogen

In 21st century, climate change is the most global challenge, leading to significant threats to the environment, human health, and socioeconomic stability. While the Earth's climate has naturally varied over time, the unprecedented acceleration and intensity of climate change in recent decades can be attributed, to a large extent, to human activities (**Figure 1-1**). Among these activities, the combustion of fossil fuels for energy production and transportation has emerged as a primary contributor to the alteration of Earth's climate system.

Fossil fuels have been the backbone of industrialization and economic development since the onset of the Industrial Revolution. Their abundant availability and high energy density have fueled the rapid advancement of societies worldwide. However, the heavy reliance on fossil fuels has come at an immense cost, with far-reaching implications for the planet's delicate balance.¹ The combustion of fossil fuels releases significant amounts of greenhouse gases (GHGs) into the atmosphere, notably carbon dioxide (CO₂), methane (CH₄), and nitrous oxide (N₂O), and these GHGs act as a thermal blanket, trapping heat from the sun and causing the Earth's average temperature to rise, a phenomenon commonly referred to as global warming (**Figure 1-2a**).² The resulting climatic changes have been observed through bushfires, droughts, arctic warming, and desertification (**Figure 1-2b**).

Green hydrogen refers to hydrogen produced from renewable energy sources, such as solar, wind, or hydroelectric power. Unlike hydrogen derived from fossil fuels including blue and grey hydrogen, green hydrogen is entirely carbon-neutral, emitting only water vapor when used as an energy carrier (**Figure 1-3**). This unique characteristic makes it an attractive substitute for fossil fuels in multiple applications, including transportation, industrial processes, and energy storage.

The adoption of green hydrogen presents several significant advantages over traditional fossil fuel-based energy systems. First and foremost, green hydrogen production provides a sustainable and renewable energy source, as it relies on readily available water and clean electricity generated from renewable sources. By shifting to green hydrogen, we can substantially reduce the emission of greenhouse gas. Furthermore, green hydrogen offers versatility in its applications. It can be used as a direct replacement for fossil fuels in transportation, enabling the deployment of hydrogen fuel cell vehicles that produce zero emissions. In industrial sectors, green hydrogen can be utilized as a clean feedstock to produce ammonia, methanol, and other chemicals, reducing the carbon footprint of manufacturing processes. Additionally, green hydrogen can serve as an efficient energy storage solution, addressing the intermittent nature of renewable energy sources and providing grid stability and

resilience (**Figure 1-4a**). The global momentum towards green hydrogen is gaining traction as governments, industries, and research institutions worldwide recognize its transformative potential. Numerous countries have announced ambitious hydrogen strategies and investment plans, aiming to scale up production, reduce costs, and create hydrogen infrastructure. Collaborative initiatives and partnerships are being established to advance research, development, and deployment of green hydrogen technologies. (**Figure 1-4b**)

However, challenges remain in the widespread adoption of green hydrogen. The production process requires significant amounts of electricity, necessitating the expansion of renewable energy capacity to meet the growing demand. Additionally, cost competitiveness with fossil fuels, the development of efficient electrolysis technologies, and the establishment of a robust hydrogen supply chain pose technical and economic challenges that need to be addressed. Despite these hurdles, ongoing research and technological advancements are poised to overcome these barriers, making green hydrogen increasingly viable and cost-effective. (**Figure 1-5**)

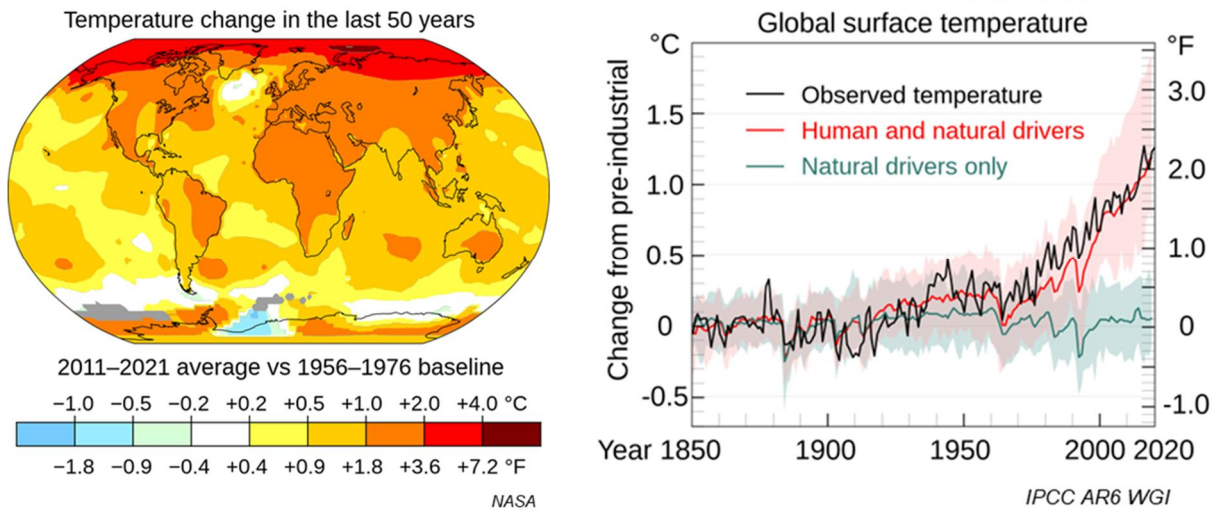


Figure 1-1. Global surface temperature change in the last 50 years and global surface temperature change by human and natural drivers.

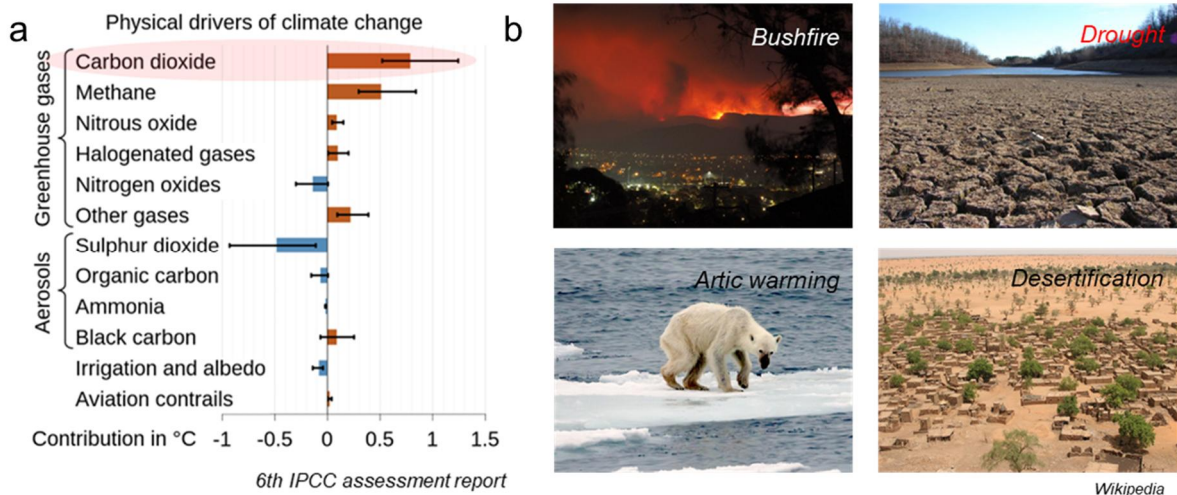


Figure 1-2. (a) The physical drives of climate change and (b) environmental phenomena caused by climate change.

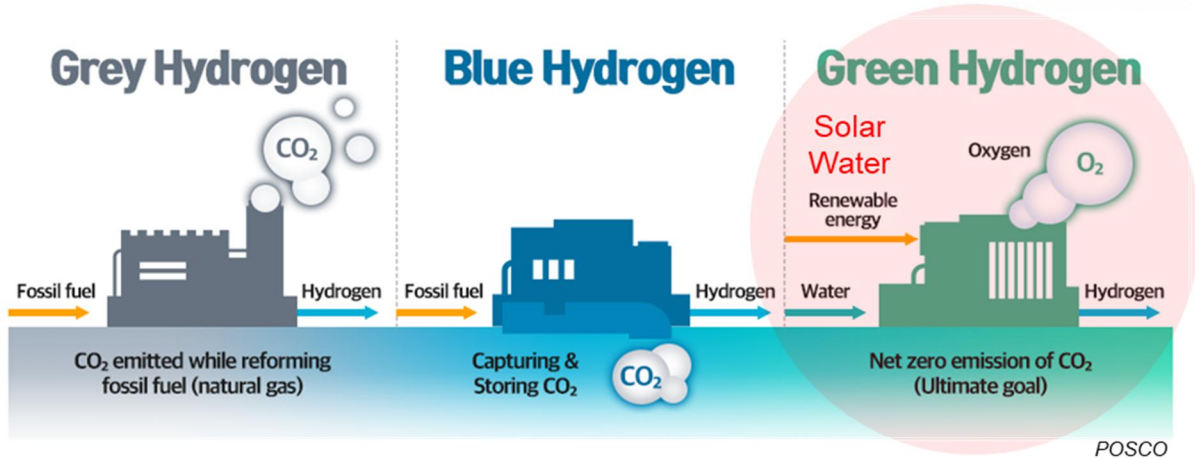


Figure 1-3. Three types of hydrogen: grey, blue, and green hydrogen.

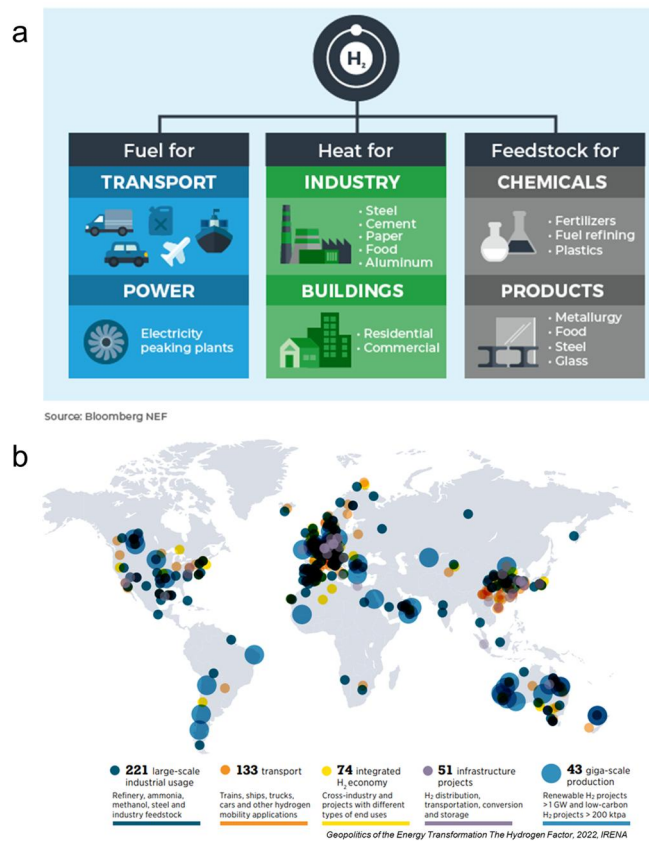


Figure 1-4. (a) The many uses of green hydrogen and (b) clean hydrogen projects and investment in 2021.

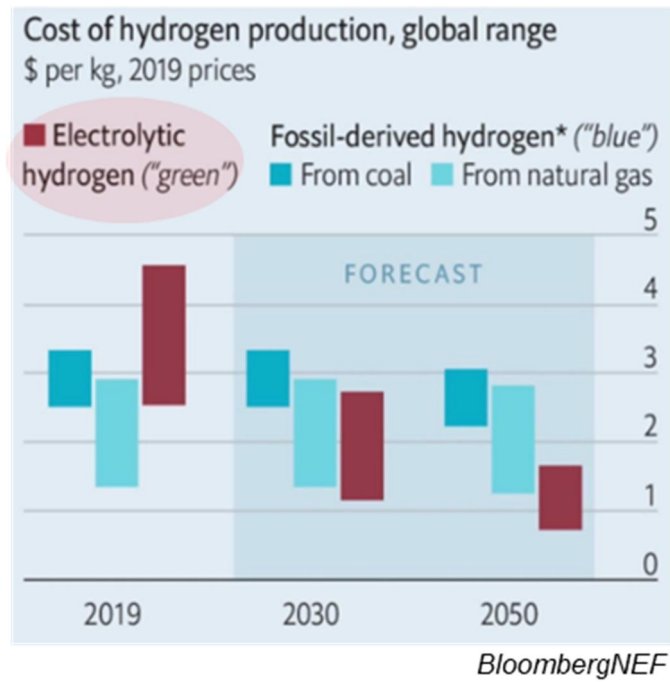


Figure 1-5. The production cost of green and blue hydrogen (\$/kg) from 2019 to 2050.

1.2 Photoelectrochemical water splitting metal oxide photoanode materials

There are representative three solar-to-hydrogen (STH) conversion routes of photocatalytic (PC), photoelectrochemical (PEC), and photovoltaic-electrolysis (PV-EC).³⁻⁶

In a PC system (**Figure 1-6a**), the dispersion of PC powders in the medium significantly shortens the charge transfer pathway compared to other systems with conventional charge collectors. In the PC system, separate gas separators are required as both H₂ and O₂ are generated from each of the PC particles. The scalability and cost-effectiveness of photocatalytic processes make them suitable for large-scale applications. However, PC system shows very low overall efficiency, which is often constrained by factors such as light absorption, catalytic activity, and stability.

PV-EC systems utilize photovoltaic cells to directly convert sunlight into electricity, which is subsequently employed to drive electrolysis reactions for water splitting (**Figure 1-6c**). This approach exhibits high STH conversion efficiencies and can be easily integrated with existing photovoltaic technologies. While it enables green hydrogen production as a versatile energy carrier and offers grid-scale energy storage capabilities, several challenges need to be addressed. These challenges include the high cost of photovoltaic cells, limited scalability, and the requirement for efficient and stable catalysts for the water splitting process.

PEC water splitting is based on the fundamental principles of semiconductor physics and electrochemistry. The photoelectrodes are linked to charge collectors, typically a semiconductor material, and absorb photons from sunlight, generating electron-hole pairs in a liquid medium (**Figure 1-6b**). The photoexcited electrons and holes undergo charge transfer processes for producing H₂ and O₂ from different photoelectrodes. To effectively separate the photogenerated charges and drive the desired redox reactions, the photoelectrodes play a pivotal role in achieving efficient and sustainable hydrogen production. While system complexity and overall efficiency of PEC cell are in the middle of PC and PV-EC systems, the development of the PEC water splitting system poses several challenges. First, the material must possess suitable energy band structures to facilitate efficient light absorption and charge separation. A narrow bandgap is desirable to capture a broad range of solar wavelengths, while a proper alignment of energy levels enables efficient charge transfer across the photoelectrode-electrolyte interface. Moreover, the photoanode material should exhibit long-term stability, corrosion resistance, and compatibility with the electrolyte environment.

In this dissertation, we mainly deal with the simple PEC water splitting system, which comprises a photoanode and a metal counter electrode system as shown in **Figure 1-7**. The PEC water splitting process consists of three main steps, namely, light absorption, charge separation and transportation, and surface reaction. During the light absorption step, the photoelectrode absorbs photons with higher

energy than the band gap (E_g), which generates photoexcited carriers (h^+ and e^-). Subsequently, the photogenerated carriers move from the bulk area to the surface area of the photoanode material for the photoelectrochemical oxidation reaction, then water oxidation occurred at the reaction surface.

By considering the several factors of three main steps (including light absorption property, charge separation and transport, and surface oxygen evolution reaction (OER) kinetics), the STH conversion efficiency is determined. As the various factors in the three steps are mainly due to the intrinsic properties of the material, finding the best photocatalyst is crucial for achieving higher STH conversion efficiency.

In recent years, significant advancements have been made in the design and synthesis of photoanode materials, leading to improved PEC water splitting performance. Metal oxides, such as titanium dioxide (TiO_2)^{7, 8}, bismuth vanadate ($BiVO_4$)⁹⁻¹¹, and tungsten trioxide (WO_3)^{12, 13}, and hematite ($\alpha-Fe_2O_3$)¹⁴⁻¹⁶ have received substantial attention due to their favorable band structures, stability, and abundance as summarized in **Table 1-1**. These materials offer promising prospects for achieving efficient charge separation and catalytic water oxidation. The selection and optimization of photoanode materials for PEC water splitting require a comprehensive understanding of their properties and performance metrics. It is because no material has met all the criteria of an ideal photocatalyst, and researchers are striving to enhance the STH conversion efficiency of photoanode materials. Thus, strategies such as bandgap engineering, doping, and surface functionalization have been employed to improve light absorption, charge transfer, and stability. Additionally, computational modeling and materials characterization techniques have contributed to the rational design and evaluation of photoanodes, enabling the identification of key parameters governing their performance.

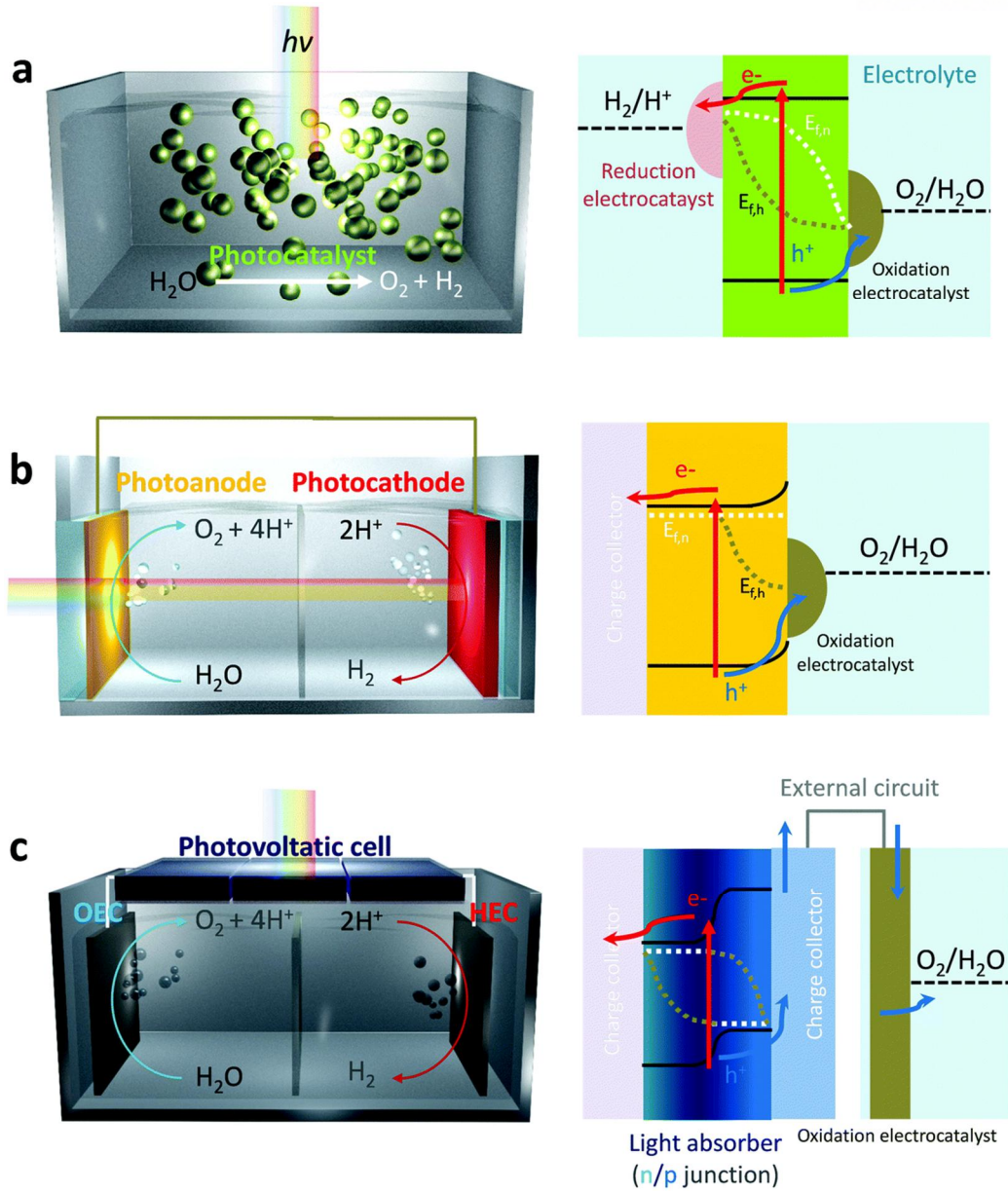


Figure 1-6. Schematic illustrations and charge flow routes of (a) PC, (b) PEC, and (c) PV-EC systems.³

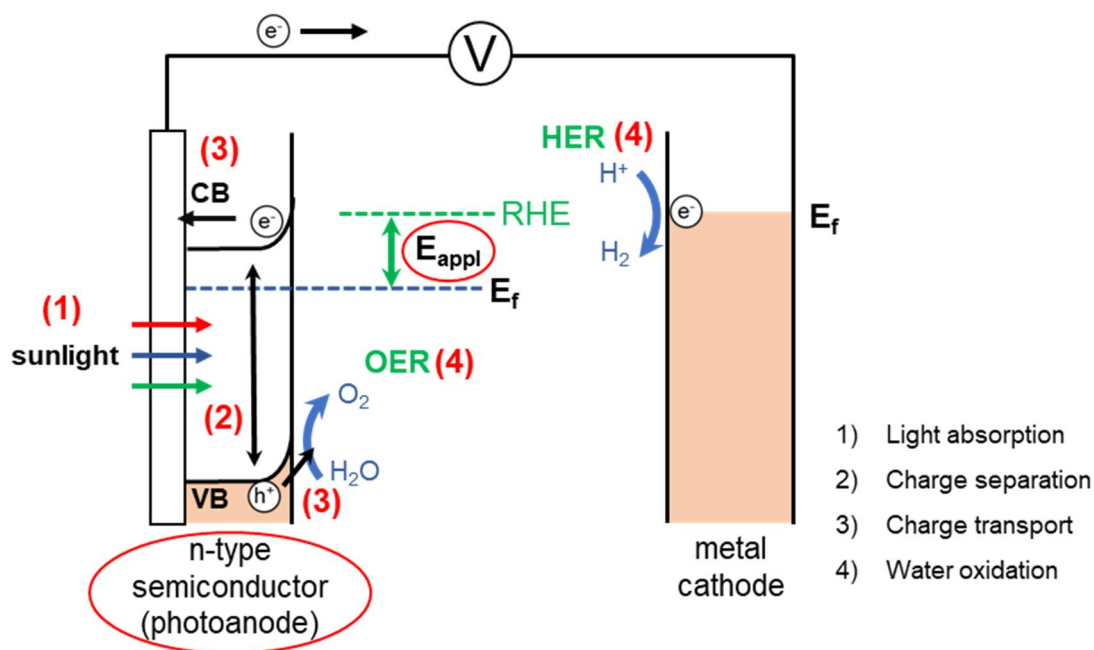


Figure 1-7. Schematic illustration of PEC water splitting system.

Photoanode	Advantages	Disadvantages
$\alpha\text{-Fe}_2\text{O}_3$	Low cost; Nontoxicity; High stability in alkaline electrolyte; Narrow bandgap (~ 2.1 eV);	Short hole diffusion length (2–4 nm); Low electron mobility ($\sim 10^{-1}$ cm ² V ⁻¹ s ⁻¹); slow water oxidation kinetics;
WO_3	Stable in acid conditions (pH < 4); Moderate hole-diffusion length (~ 150 nm); Good electron mobility;	Large band gap (~ 2.6 eV); Sluggish water oxidation kinetics; Rapid electron-hole recombination;
BiVO_4	Suitable bandgap of ~ 2.4 eV; relatively high conduction band edge (0.1–0.2 V _{NHE}); Low onset potential for OER;	Poor electrical conductivity; Sluggish water oxidation kinetics; Poor stability; Poor charge separation;
TiO_2	Stable against chemical- and photo-corrosion; Low cost; Suitable valence band edge; Good electrical properties;	Large bandgap of 3.0–3.2 eV; Low absorption for visible light; Poor charge separation;

Table 1-1. Advantages and disadvantages of metal oxide photoanode materials for PEC water oxidation.

1.3 Hematite ($\alpha\text{-Fe}_2\text{O}_3$) and research progress

In the PEC system, a high theoretical STH conversion efficiency is a crucial criterion for selecting appropriate photoanode material, as the commercialization benchmark for STH conversion efficiency is 10%. Among various metal oxide photoanode materials, until 2018, BiVO_4 or $\text{BiVO}_4/\text{WO}_3$ exhibited a photocurrent density of over 6 mA cm^{-2} at $1.23 \text{ V}_{\text{RHE}}$, but their low theoretical STH conversion efficiency limits their potential for practical applications (**Figure 1-8a**).⁹

In that point of view, hematite is considered the most promising candidate for photoanode material as it possesses a higher theoretical photocurrent density of 12.4 mA cm^{-2} (STH conversion efficiency of 15%) than other metal oxide photoanode materials as depicted in **Figure 1-8b**.⁹ Also, it shows high chemical stability in alkaline electrolytes, natural abundance, and non-toxicity. However, because of the short hole diffusion length (2-4 nm), low electrical conductivity, and sluggish water oxidation kinetics, the experimental STH conversion efficiency of hematite of $\sim 6\%$ is much lower than its theoretical STH value of $\sim 15\%$.¹⁷ Moreover, hematite needs an external potential of $\sim 0.4 \text{ V}$ because the level of conduction band is lower than the water reduction potential (**Figure 1-9**).¹⁸ Thus, the various strategies including morphology design, n-type doping, surface modifications (with surface passivation layer and incorporation of cocatalysts), and tandem design (with photocathode and solar cells) have been explored to enhance the PEC performance of hematite.

For resolving the short hole diffusion length, the different hematite nanostructures including dendrites, nanoparticles, mesoporous, nanorods, nanowires, nanosheets, nanotubes, nanocones, and cauliflower have been studied (**Figure 1-10a**).¹⁴ It was synthesized by various methods such as electrodeposition, anodization, colloidal synthesis, hydrothermal and ultrasonic spray pyrolysis, and APCVD (atmospheric pressure chemical vapor deposition) methods. These nanostructures can provide large active surface area and efficient charge transport property for efficient photoelectrochemical water splitting, leading to high photocurrent density compared to bulk structure as shown in **Figure 1-10b**.¹⁴ Among several nanostructures, one dimensional (1D) nanostructure can accelerate the charge transport behavior by minimizing the distance that charge carriers need to travel and charge recombination rate at grain boundaries. Overall, hematite nanostructuring in one-dimensional forms provides advantages such as efficient charge transport, enhanced light absorption, large surface area, potential for synergistic coupling with other materials, and flexibility in design and fabrication. These advantages make hematite 1D nanostructures promising candidates for high-performance PEC water splitting devices.

At the hematite surface, the large charge recombination is generated due to slow charge transfer and surface states (recombination center) (**Figure 1-11a**). Thus, the photogenerated hole can be injected into the electrolyte only at high applied potentials, leading to the large OER overpotential. Since the

low onset potential is another major challenge for an efficient PEC system, it can be handled by depositing OER co-catalyst^{19, 20} and surface overlayer (**Figures 1-11b,c**)²¹. Although the detailed mechanism of the co-catalyst and surface overlayer is quite different, as shown in **Figures 1-11d,e**, the cathodic shift of onset potential after depositing Co-Pi co-catalyst and Al₂O₃ overlayer implies the reduced charge recombination rate and enhanced hole transport. Besides the strategies of improving intrinsic electrical properties of hematite, the surface modifications with co-catalyst and surface overlayer are the crucial point to facilitate the hole transport to electrolyte and overall PEC performance.

As the hematite has low electrical properties compared to other metal oxide photoanode materials (**Table 1-2**)¹⁴, heteroatom doping is commonly used to boost the electrical properties of hematite. The introduction of dopants into the hematite lattice enhances both electronic and morphological properties, leading to improved photocatalytic activity. Various dopants such as Ti²², Sn²³, Si¹⁸, and Ge¹⁷ are commonly used to enhance PEC activities. Although heteroatom doping on hematite is a useful strategy for altering the properties of hematite, it is limited by various factors such as structural distortion caused by size difference between n-type dopants and Fe³⁺, and low doping limit.^{24,25} Moreover, for a highly efficient PEC system, the co-doping system of introducing two or more different dopant elements into the hematite lattice is a promising avenue for optimizing its properties and overcoming its limitations. The specific effects of co-doping can vary depending on the dopant elements used, their concentrations, and the fabrication techniques employed, necessitating detailed experimental investigations to fully understand and optimize the co-doping system in hematite. By carefully selecting the dopant elements and controlling their concentrations, the properties of hematite can be modified to improve its performance.

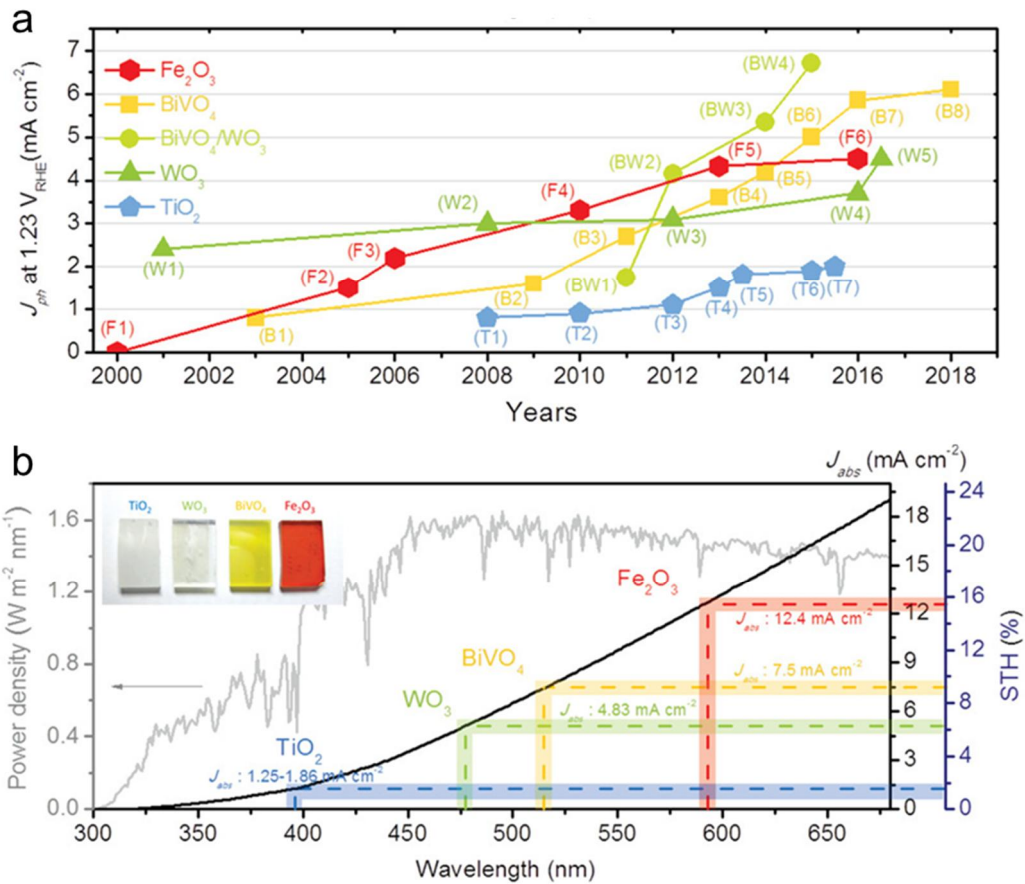


Figure 1-8. (a) Reported photocurrent density at 1.23 V_{RHE} and (b) theoretical photocurrent density and STH efficiency of metal oxide photoanode materials.⁹

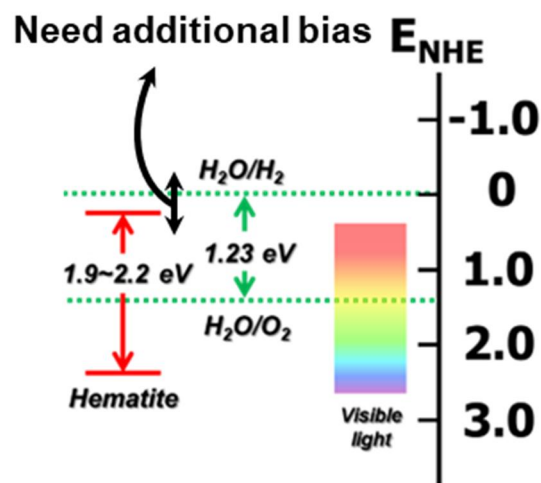


Figure 1-9. Energy band position of metal oxide photoanode materials.

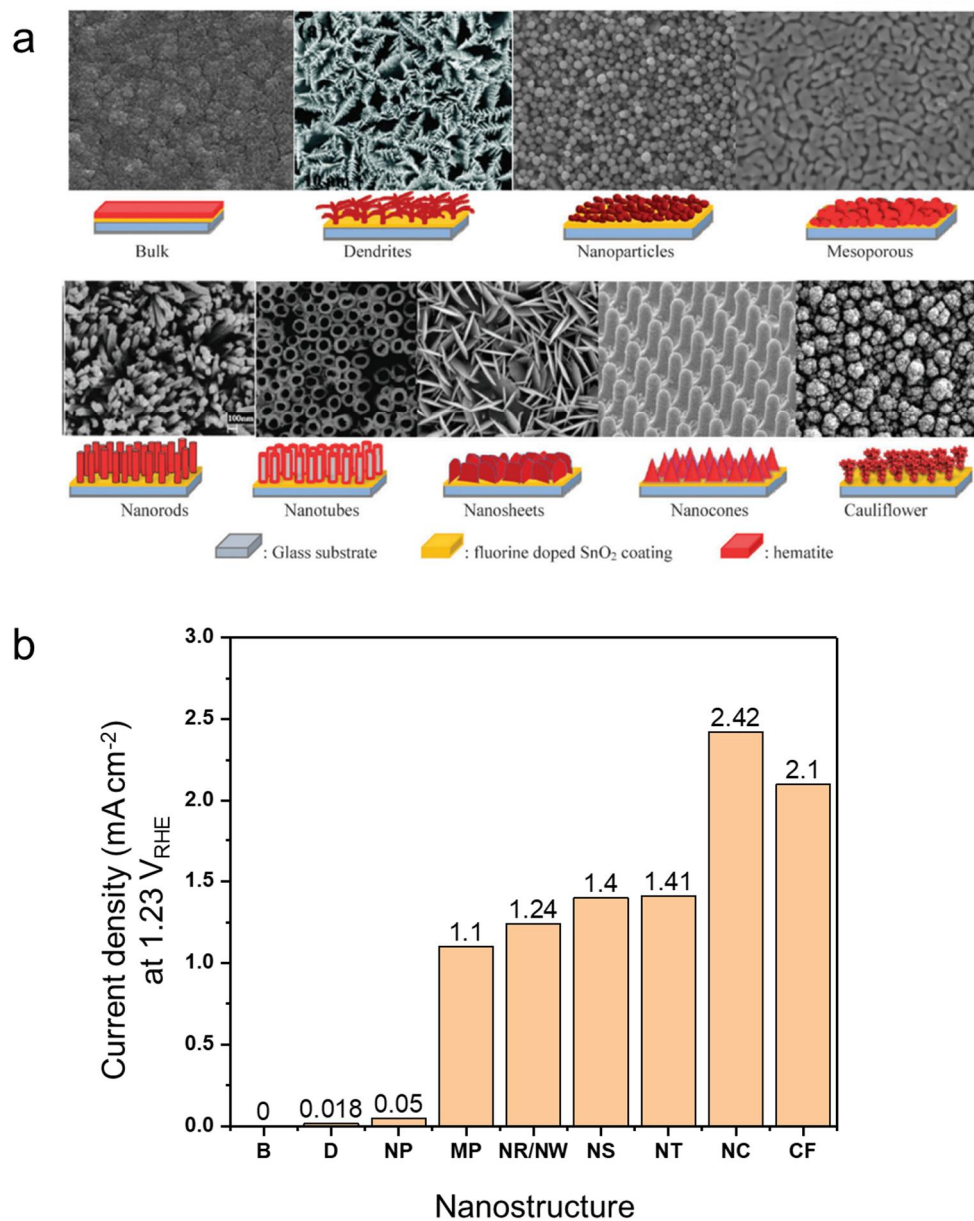


Figure 1-10. Morphology engineering of hematite. (a) SEM images and corresponding schematic illustrations and (b) photocurrent density at 1.23 V vs. RHE of hematite nanostructures (B: Bulk, D: Dendrites, NP: Nanoparticles, MP: Mesoporous, NR: Nanorods, NW: Nanowires, NS: Nanosheets, NT: Nanotubes, NC: Nanocones, and CF: Cauliflower).¹⁴

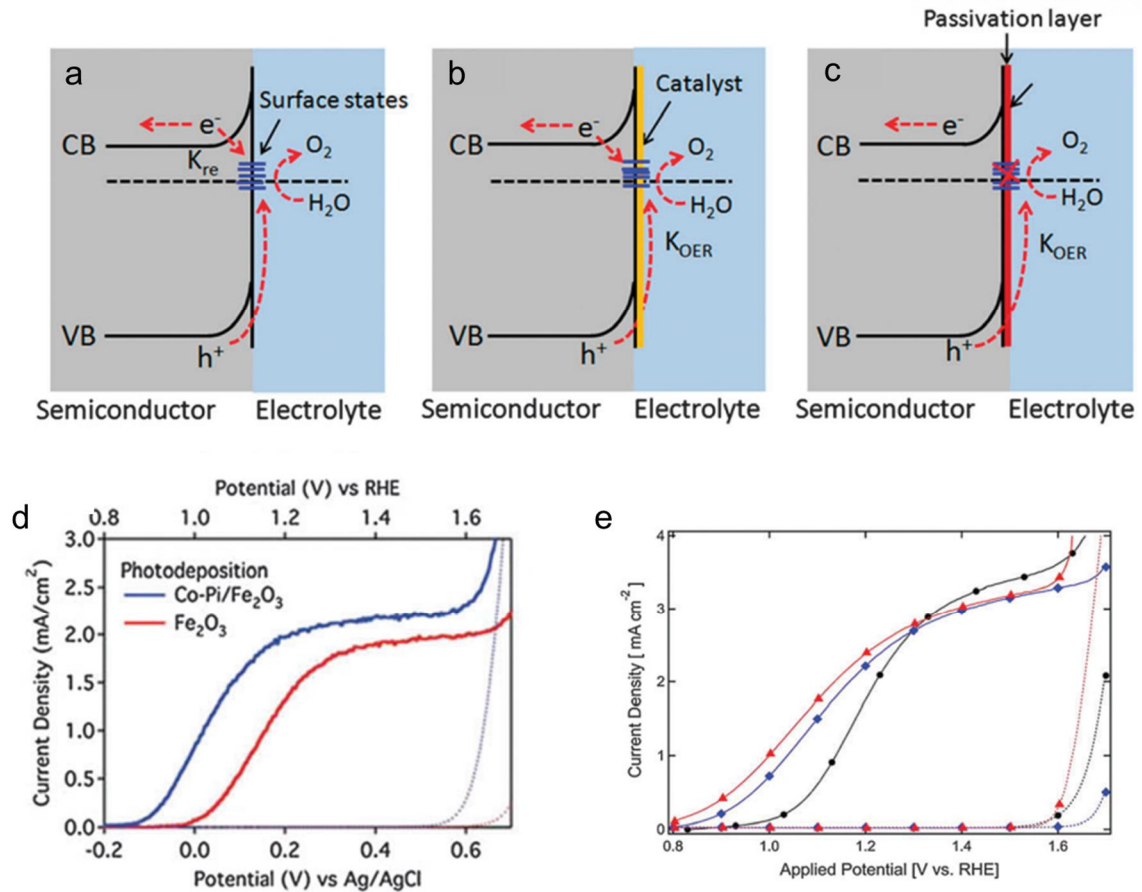


Figure 1-11. Surface modifications on hematite. Band structure of an (a) n-type semiconductor photoanode, (b) n-type semiconductor photoanode with co-catalyst, and (c) n-type semiconductor photoanode with surface passivation layer with an electrolyte.¹⁴ (d) J-V curves of Co-Pi/Fe₂O₃ and Fe₂O₃ under 1 SUN and dark conditions.²⁰ (e) J-V curves of Fe₂O₃ (black), Al₂O₃/Fe₂O₃ (blue), and Co/Al₂O₃/Fe₂O₃ under 1 SUN and dark conditions.²¹

Photoanode	Carrier mobility (cm ² V ⁻¹ s ⁻¹)	Carrier lifetime	Hole diffusion length (nm)
α-Fe ₂ O ₃	0.01-0.1	3-10 ps	2-4
WO ₃	16	1-9 ns	150
BiVO ₄	1	N/A	10-20
TiO ₂	0.2	40 ns	100

Table 1-2. Electrical properties of metal oxide photoanode materials.¹⁴

1.4 Research outline

In my dissertation, we aim to address the challenges associated with hematite-based PEC water splitting systems through a multifaceted approach. The research focuses on heteroatom doping, and OER co-catalyst deposition to improve the intrinsic electronic properties and charge injection properties at the interface of electrode/electrolyte.

In chapter 2, the aspect of this research involves non-metallic Si doping to control the excess content of unintentionally diffused Sn from the fluorine-doped tin oxide (FTO) substrate. We firstly fabricated highly transparent thin film hematite under 100 nm thickness for designing multi-photoanode (dual photoanodes) system. Through the fabrication of thin film hematite, high transparency was achieved, but it showed a low PEC efficiency compared to thick film hematite. It is due to the excess diffusion of Sn content about 5% from the FTO substrate compared to that of conventional thick film hematite (Sn ~2%). The excessive Sn content on the surface was controlled by SiO_x deposition and following Si doping to the hematite surface during high-temperature annealing. With controlled Sn content, the surface charge transfer efficiency of thin film hematite was greatly improved, and for further enhancement, NiFeO_x co-catalyst was deposited on the surface and assembled as a dual photoanode. By utilizing the dual hematite photoanode, a tandem design with perovskite solar cells (PSC) has been conducted. Through the high transparency of the hematite photoanode, the optical loss of PSC, which was a main drawback of the conventional hematite/PSC tandem cell, was resolved, and ultimately, a high STH conversion efficiency of 4.49% was achieved under an unbiased system.

In chapter 3, we figured out the improved PEC activities of Si and Sn co-doped hematite compared to that of Sn-doped hematite from the results of chapter 2. To determine which dopant, Sn and Si, exhibits better PEC activities on hematite, we controlled Sn and Si content through a two-step annealing process. Typically, Sn and Si diffuse from the FTO substrate and surface SiO_x overlayer, respectively during the one-step thermal annealing process. By adjusting the annealing steps (two-step annealing) to control the diffusion length of Sn, we were able to reduce the amount of Sn on the surface and increase the amount of Si. Through various electrochemical analyses, we confirmed that the two-step annealed samples with higher Si content exhibited superior PEC performance, highlighting the superiority of Si as a dopant compared to Sn. Additionally, we observed that when hematite electrodes were used as OER electrodes in a Zn-air battery system, the photoexcitation from hematite photoanode resulted in a charging potential of 1.45 V, which is lower than the theoretical charging potential of 1.65 V for the Zn-air battery. This observation indicates the potential for additional applications of hematite, further confirming its versatility.

In chapter 4, we synthesized MXene nanofragments (NFMX) and utilized NFMX as an OER co-catalyst. Generally, MXene ($\text{Ti}_3\text{C}_2\text{T}_x$; T: functional groups), as a two-dimensional (2D) material, possesses excellent electrical properties. However, due to its 2D sheet-like structure and micro-scale size, it is challenging to combine it with one-dimensional (1D) hematite, which typically has sizes in the range of tens to hundreds of nanometers. In this study, to mitigate this structural mismatch, we fabricated nanofragments with sizes below 10 nm and employed them as co-catalysts. The use of NFMX improved hole extraction and hole transport rates due to their numerous functional groups and favorable electrical properties. Furthermore, the stability and efficiency were enhanced by additional $\text{NiFe}(\text{OH})_x$ deposition as a co-catalyst.

In conclusion, photoelectrochemical water splitting holds great promise as a sustainable and efficient method for hydrogen production. The development of efficient photoanode materials is crucial for realizing the full potential of photoelectrochemical water splitting system. We have focused on resolving the drawbacks of hematite photoanode. The strategies of heteroatom (Sn and Si) doping, and co-catalyst ($\text{NiFe}(\text{OH})_x$, and MXene nanofragment) deposition are mainly considered to develop the PEC activities of hematite photoanodes. Also, application studies for hematite/PSC tandem cells and OER electrode of Zn-air batteries have been performed. By addressing these fundamental challenges, we aim to utilize the hematite photoanode as a viable and efficient material, contributing to the development of sustainable and clean energy solutions.

1.5 References

1. Welsby, D.; Price, J.; Pye, S.; Ekins, P. J. N., Unextractable fossil fuels in a 1.5° C world. **2021**, *597 (7875)*, 230-234.
2. Fawzy, S.; Osman, A. I.; Doran, J.; Rooney, D. W. J. E. C. L., Strategies for mitigation of climate change: a review. **2020**, *18*, 2069-2094.
3. Kim, J. H.; Hansora, D.; Sharma, P.; Jang, J.-W.; Lee, J. S. J. C. S. R., Toward practical solar hydrogen production—an artificial photosynthetic leaf-to-farm challenge. **2019**, *48 (7)*, 1908-1971.
4. Hisatomi, T.; Kubota, J.; Domen, K. J. C. S. R., Recent advances in semiconductors for photocatalytic and photoelectrochemical water splitting. **2014**, *43 (22)*, 7520-7535.
5. Tee, S. Y.; Win, K. Y.; Teo, W. S.; Koh, L. D.; Liu, S.; Teng, C. P.; Han, M. Y. J. A. s., Recent progress in energy-driven water splitting. **2017**, *4 (5)*, 1600337.
6. Ager, J. W.; Shaner, M. R.; Walczak, K. A.; Sharp, I. D.; Ardo, S. J. E.; Science, E., Experimental demonstrations of spontaneous, solar-driven photoelectrochemical water splitting. **2015**, *8 (10)*, 2811-2824.
7. Ahmad, M. S.; Pandey, A. K.; Abd Rahim, N. J. R.; Reviews, S. E., Advancements in the development of TiO₂ photoanodes and its fabrication methods for dye sensitized solar cell (DSSC) applications. A review. **2017**, *77*, 89-108.
8. Kment, S.; Riboni, F.; Pausova, S.; Wang, L.; Wang, L.; Han, H.; Hubicka, Z.; Krysa, J.; Schmuki, P.; Zboril, R. J. C. S. R., Photoanodes based on TiO₂ and α -Fe₂O₃ for solar water splitting—superior role of 1D nanoarchitectures and of combined heterostructures. **2017**, *46 (12)*, 3716-3769.
9. Kim, J. H.; Lee, J. S. J. A. M., Elaborately modified BiVO₄ photoanodes for solar water splitting. **2019**, *31 (20)*, 1806938.
10. Tan, H. L.; Amal, R.; Ng, Y. H. J. J. o. M. C. A., Alternative strategies in improving the photocatalytic and photoelectrochemical activities of visible light-driven BiVO₄: a review. **2017**, *5 (32)*, 16498-16521.
11. Xu, X. T.; Pan, L.; Zhang, X.; Wang, L.; Zou, J. J. J. A. S., Rational design and construction of cocatalysts for semiconductor-based photo-electrochemical oxygen evolution: a comprehensive review. **2019**, *6 (2)*, 1801505.
12. Kalanoor, B. S.; Seo, H.; Kalanur, S. S. J. M. S. f. E. T., Recent developments in photoelectrochemical water-splitting using WO₃/BiVO₄ heterojunction photoanode: A review. **2018**, *1 (1)*, 49-62.
13. Zheng, G.; Wang, J.; Liu, H.; Murugadoss, V.; Zu, G.; Che, H.; Lai, C.; Li, H.; Ding, T.; Gao, Q. J. N., Tungsten oxide nanostructures and nanocomposites for photoelectrochemical water

splitting. **2019**, *11* (41), 18968-18994.

14. Tamirat, A. G.; Rick, J.; Dubale, A. A.; Su, W.-N.; Hwang, B.-J. J. N. h., Using hematite for photoelectrochemical water splitting: a review of current progress and challenges. **2016**, *1* (4), 243-267.
15. Shen, S.; Lindley, S. A.; Chen, X.; Zhang, J. Z. J. E.; Science, E., Hematite heterostructures for photoelectrochemical water splitting: rational materials design and charge carrier dynamics. **2016**, *9* (9), 2744-2775.
16. Li, C.; Luo, Z.; Wang, T.; Gong, J. J. A. M., Surface, bulk, and interface: rational design of hematite architecture toward efficient photo-electrochemical water splitting. **2018**, *30* (30), 1707502.
17. Yoon, K.-Y.; Park, J.; Jung, M.; Ji, S.-G.; Lee, H.; Seo, J. H.; Kwak, M.-J.; Il Seok, S.; Lee, J. H.; Jang, J.-H. J. N. C., NiFeO_x decorated Ge-hematite/perovskite for an efficient water splitting system. **2021**, *12* (1), 4309.
18. Park, J.; Yoon, K.-Y.; Kim, T.; Jang, H.; Kwak, M.-J.; Kim, J. Y.; Jang, J.-H. J. N. E., A highly transparent thin film hematite with multi-element dopability for an efficient unassisted water splitting system. **2020**, *76*, 105089.
19. Zhang, J.; García-Rodríguez, R.; Cameron, P.; Eslava, S. J. E.; Science, E., Role of cobalt-iron (oxy) hydroxide (CoFeO_x) as oxygen evolution catalyst on hematite photoanodes. **2018**, *11* (10), 2972-2984.
20. Zhong, D. K.; Cornuz, M.; Sivula, K.; Grätzel, M.; Gamelin, D. R. J. E.; Science, E., Photo-assisted electrodeposition of cobalt-phosphate (Co-Pi) catalyst on hematite photoanodes for solar water oxidation. **2011**, *4* (5), 1759-1764.
21. Le Formal, F.; Tetreault, N.; Cornuz, M.; Moehl, T.; Grätzel, M.; Sivula, K. J. C. S., Passivating surface states on water splitting hematite photoanodes with alumina overlayers. **2011**, *2* (4), 737-743.
22. Yoon, K.-Y.; Ahn, H.-J.; Kwak, M.-J.; Kim, S.-I.; Park, J.; Jang, J.-H. J. J. o. M. C. A., A selectively decorated Ti-FeOOH co-catalyst for a highly efficient porous hematite-based water splitting system. **2016**, *4* (48), 18730-18736.
23. Li, M.; Yang, Y.; Ling, Y.; Qiu, W.; Wang, F.; Liu, T.; Song, Y.; Liu, X.; Fang, P.; Tong, Y. J. N. L., Morphology and doping engineering of Sn-doped hematite nanowire photoanodes. **2017**, *17* (4), 2490-2495.
24. Annamalai, A.; Lee, H. H.; Choi, S. H.; Lee, S. Y.; Gracia-Espino, E.; Subramanian, A.; Park, J.; Kong, K.-j.; Jang, J. S. J. S. r., Sn/Be sequentially co-doped hematite photoanodes for enhanced photoelectrochemical water oxidation: effect of Be²⁺ as co-dopant. **2016**, *6* (1), 23183.
25. Ling, Y.; Wang, G.; Wheeler, D. A.; Zhang, J. Z.; Li, Y. J. N. l., Sn-doped hematite nanostructures for photoelectrochemical water splitting. **2011**, *11* (5), 2119-2125.

Chapter 2. A Highly Transparent Thin Film Hematite with Multi-Element Dopability for an Efficient Unassisted Water Splitting System

*Chapter 2 is reproduced in part with permission from J. Park, et al., *Nano Energy*. **2020**, 76, 105089.

2.1 Introduction

The exploration of efficient and sustainable photoelectrochemical (PEC) systems for solar-driven water splitting has gained significant attention due to their potential for renewable hydrogen production. Hematite ($\alpha\text{-Fe}_2\text{O}_3$) has emerged as a promising material in PEC systems owing to its narrow bandgap (1.9-2.2eV), non-toxic nature, abundance, and excellent stability under water oxidation conditions.¹⁻⁴ However, despite these favorable characteristics, hematite suffers from critical drawbacks, including a sluggish oxygen evolution reaction (OER) process, high charge recombination rate, and a short hole diffusion length (2-4nm).⁵ The most significant disadvantage is the bandgap mismatch, with the conduction band energy level of hematite being 0.4-0.5 eV lower than the reduction potential of water, necessitating an additional bias for hydrogen gas generation.^{6,7}

To address the bandgap mismatch and enable unassisted solar-driven water splitting, a tandem system employing a combined hematite photoanode and perovskite solar cell configuration has been proposed.⁸ This configuration utilizes the external photovoltage generated from the solar cell to resolve the bandgap mismatch problem. However, the current tandem system suffers from low solar-to-hydrogen (STH) conversion efficiency due to the limited light absorption of the perovskite solar cell, resulting from the similar light absorption spectrum shared by hematite and perovskite.¹⁰ The majority of incident light is absorbed by the front-sided hematite photoanode, leading to diminished light reaching the back-sided perovskite solar cell (PSC). Consequently, the solar cell performance and overall STH efficiency are significantly reduced.

To achieve high STH efficiency in the tandem PEC system and enhance solar cell performance, a highly transparent hematite photoanode is essential for efficient light utilization by the solar cell. Previous studies have reported excellent structural stability and reproducibility of hematite thin films prepared by various techniques such as pulsed laser deposition (PLD)^{11, 12}, atomic layer deposition (ALD)¹³⁻¹⁵, spray pyrolysis^{16, 17}, and ultrasonic spray pyrolysis (USP)^{18, 19}. However, the performance of these thin film hematite photoanode has been limited to low photocurrent densities below 1 mA cm^{-2} at 1.23 V vs. RHE due to insufficient active area and poor light absorption. Thus, it is essential to optimize the performance of both the hematite photoanode and the perovskite solar cell while considering the trade-off relationship between the two components.

In chapter 2, we address the limitations of the tandem system by fabricating a highly transparent photoanode that exhibits excellent performance. To achieve this, we employ Si doping and deposit a transparent NiFeO_x co-catalyst onto a thin film hematite. The initial decrease in photocurrent density observed in the thin film compared to the pristine thick film is due to the excess Sn content. Through Si doping, we can reduce the Sn content and after depositing NiFeO_x co-catalyst, the optimized hematite photoanode exhibited improved electrical conductivity in the bulk and surface region.

For efficient tandem design, the dual hematite photoanodes are assembled with a perovskite solar cell. It exhibited a high solar-to-hydrogen (STH) efficiency of 4.49%, representing nearly five times the performance of the pristine hematite/perovskite solar cell configuration. It is attributed to the improved surface reaction kinetics, enhanced charge concentration, and optimized bulk transport properties achieved through the Sn control in hematite via non-metallic Si doping and the deposition of a transparent oxygen evolution reaction (OER) catalyst.

2.2 Experimental section

-Fabrication of Ti-Fe₂O₃(T) and Ti-Fe₂O₃(t) photoanodes

Ti-doped FeOOH was synthesized on FTO at 100 °C in oven using a 100 mL aqueous solution containing 150 mM FeCl₃·6H₂O and 7 μL TiCl₃ solution for 3 hours. The sample was washed with DI water and dried with N₂ gas before inserted into a tube furnace and annealed at 800 °C for 20 minutes to transform it into Ti-Fe₂O₃(T). Ti-Fe₂O₃(t) was prepared using the same procedure as Ti-Fe₂O₃(T) but with the use of 30 mM FeCl₃·6H₂O instead of 150 mM FeCl₃·6H₂O.

-Fabrication of Ti:Si-Fe₂O₃(t) photoanode

An thin amorphous SiO_x layer was formed on the hematite surface using the dip-coating process with an APTMS solution. The APTMS solution was prepared by mixing DI water and APTMS in a ratio of 100:1 (v:v%). Once the APTMS solution was uniformly spread over the hematite surface, a high-temperature annealing process was used to induce thermal diffusion of Si from the SiO_x overlayer to the Ti-Fe₂O₃(t) resulting in the formation of Ti:Si-Fe₂O₃(t).

-Fabrication of NiFeO_x@Ti:Si-Fe₂O₃ photoanode

To decorate the NiFeO_x catalyst, a mixture of Iron(III) 2-ethylhexanoate (50% w/w in mineral spirits, Strem Chemicals) and nickel(II) 2-ethylhexanoate (78% w/w in 2-ethylhexanoic acid, Strem Chemicals) in a hexane solution was used to create a total concentration of 15% w/w metal complex. The as-prepared solution was diluted with hexane and then irradiated under UV light before being annealed at 100 °C for 1 hour.

-Fabrication of Perovskite solar cells

The SnO₂ nanoparticle layer was deposited on the ITO substrates through spin-coating at 3000 rpm for 30 seconds and then annealed at 150 °C for 30 minutes. The perovskite precursor solution was prepared by dissolving 213.8 mg of FAI, 28.4 mg of MABr, 691.3 mg of PbI₂ and 110 mg of PbBr₂ in 1 mL of DMF and DMSO (8:2 v/v%) solvent. The solution was then coated onto the SnO₂/ITO substrate through a two-step spin-coating process at 3000 and 5000 rpm for 15 and 20 seconds, respectively. After the first spin-coating step, the substrate was treated with ethyl acetate drop-casting, and then dried on a hot plate at 100 °C for 10 minutes. The spiro-OMeTAD solution prepared by dissolving 82 mg spiro-OMeTAD, 19.6 μL bis(trifluoromethane) sulfonimide lithium salt (540 mg LI-TFSI in 1 mL acetonitrile) and 33.8 μL 4-tert-butylpyridine in 1 mL of CB solvent, was coated on the perovskite layer at 3000 rpm for 30 seconds. Finally, an Au electrode with a thickness of 60 nm was deposited on the hole transporting

layer under vacuum ($<10^{-6}$ Torr) through thermal evaporation.

-Electrochemical measurements

All photoelectrochemical (PEC) measurements were conducted in a three-electrode under front-side simulated Air Mass 1.5 Global (AM 1.5 G) illumination. The cell comprised of an Ag/AgCl (KCl sat.) reference electrode and a Pt mesh counter electrode. The photoanode had an exposed area of 0.44 cm^2 , which was achieved by using an O-ring in a homemade PEC kit and 1.0 M NaOH solution served as a pH 13.6 electrolyte. The potential vs. RHE was calculated using the Nernst equation $E_{\text{RHE}} = E_{\text{Ag/AgCl}} + 0.0591(\text{pH}) + 0.1976 \text{ V}$. The current density-voltage (J-V) curve was recorded at a scan rate of 20 mV s^{-1} . Photocurrent stability tests were performed by measuring the photocurrent under AM 1.5 G illumination at a 1.23 V vs. RHE. Electrochemical impedance spectroscopy (EIS) was carried out using a potentiostat at a frequency range of 100 kHz to 0.1 Hz. The experimental EIS data were analyzed and fitted using Zview software. The incident photon to current conversion efficiency (IPCE) was measured under monochromatic light by a Xe lamp, and the intensity of the monochromatic light was measured by a luminometer. The J-V characteristics of the solar cells were measured using a Keithley 2635A Source Measure Unit. The solar cell performance was tested under illumination by an AM 1.5 G solar simulator with an irradiation intensity of 100 mW/cm^2 .

2.3 Results and discussion

2.3.1 Hematite photoanode and PSC tandem cells

Figure 2-1a illustrates a schematic image of a tandem cell consisting of a perovskite solar cell (PSC) and hematite films with two different thicknesses of 350 nm and 70 nm, respectively. Previous studies have shown that the similar light absorption spectra of the PSC and hematite (**Figure 2-2**) can result in severe degradation of PSC performance in hematite/PSC tandem cells. In this study, it was hypothesized that the use of highly efficient and transparent hematite could potentially enhance the performance of PSC, resulting in an overall efficient hematite/PSC tandem cell performance.

To fabricate the highly transparent hematite films, the thickness was controlled from 350 nm to 10 nm by varying the concentration of the $\text{FeCl}_3 \cdot 6\text{H}_2\text{O}$ solution (**Figure 2-3**). The thicknesses of 350 nm and 70 nm were selected based on optimizing the photocurrent density and transmittance of hematite films. These thick and thin hematite films were denoted as $\text{Ti-Fe}_2\text{O}_3(\text{T})$ and $\text{Ti-Fe}_2\text{O}_3(\text{t})$, respectively (**Figure 2-4**), and they exhibited a similar bandgap of 2.15 eV and 2.1 eV, respectively, as shown by the Tauc plot analysis (**Figure 2-5**).

To evaluate the performance of the tandem cell with respect to the light absorption properties of PSC and hematite films, we measured the external quantum efficiency (EQE) and the current density-voltage (J-V) curves of PSC behind $\text{Ti-Fe}_2\text{O}_3(\text{T})$ and $\text{Ti-Fe}_2\text{O}_3(\text{t})$ (**Figure 2-2b,c**). A PSC with a photoconversion efficiency of 15.46%, short-circuit current (J_{sc}) of 22.1 mA cm^{-2} , open-circuit voltage (V_{oc}) of 1.17, and fill factor of 0.61 was utilized²⁰, and the photovoltaic parameters of PSC behind several types of hematite photoanodes are summarized in **Figure 2-6**.

In **Figure 2-2b**, the PSC without a hematite film exhibited a high EQE of over 70% within the 350-550 nm light spectrum range, while the PSC behind $\text{Ti-Fe}_2\text{O}_3(\text{T})$ had a very low EQE of less than 5% within the same range. The J_{sc} of the PSC behind $\text{Ti-Fe}_2\text{O}_3(\text{T})$ dropped sharply to 4.74 mA cm^{-2} from its initial value of 22.1 mA cm^{-2} . However, the PSC behind $\text{Ti-Fe}_2\text{O}_3(\text{t})$ exhibited the J_{sc} of 15.5 mA cm^{-2} , which is 3.3-fold higher than the PSC behind $\text{Ti-Fe}_2\text{O}_3(\text{T})$ due to the high transparency of $\text{Ti-Fe}_2\text{O}_3(\text{t})$ (**Figure 2-2c**). Furthermore, $\text{Ti-Fe}_2\text{O}_3(\text{t})$ exhibited a larger V_{oc} of 1.16 compared to $\text{Ti-Fe}_2\text{O}_3(\text{T})$ with a V_{oc} of 1.08. These results demonstrate the advantages of using a thin film hematite ($\text{Ti-Fe}_2\text{O}_3(\text{t})$) to improve the PSC performance.

The tandem cell operating current density (J_{op}) is determined at the intersection point of the J-V curves of hematite and the PSC in **Figure 2-2c**. Despite the PSC behind $\text{Ti-Fe}_2\text{O}_3(\text{t})$ exhibiting a higher photocurrent density than the PSC behind $\text{Ti-Fe}_2\text{O}_3(\text{T})$, the J_{op} (0.9 mA cm^{-2}) of $\text{Ti-Fe}_2\text{O}_3(\text{t})$ (J_{op_t}) was

only slightly higher than that of J_{op} (0.75 mA cm^{-2}) of $\text{Ti-Fe}_2\text{O}_3(\mathbf{T})$ (J_{op_T}), as shown in the inset of **Figure 2-2c**. This was due to the low photoelectrochemical (PEC) water splitting performance of $\text{Ti-Fe}_2\text{O}_3(\mathbf{t})$. In order to achieve high-performance unbiased water-splitting tandem cells, it is necessary to have both high PEC efficiency and high transmittance.

2.3.2 PEC activities of $\text{Ti-Fe}_2\text{O}_3(\mathbf{t})$ vs. $\text{Ti-Fe}_2\text{O}_3(\mathbf{T})$

In **Figure 2-7a**, $\text{Ti-Fe}_2\text{O}_3(\mathbf{t})$ showed a lower photocurrent density of 1.1 mA cm^{-2} at 1.23 V vs. RHE ($1.23 \text{ V}_{\text{RHE}}$) and an anodic shift in the onset potential compared to that of $\text{Ti-Fe}_2\text{O}_3(\mathbf{T})$. We attributed the low PEC activities of $\text{Ti-Fe}_2\text{O}_3(\mathbf{t})$ to the reduced number of electron-hole pairs caused by the low light absorption of $\text{Ti-Fe}_2\text{O}_3(\mathbf{t})$ (**Figure 2-4c**) and different metal content, which was revealed by X-ray photoelectron spectroscopy (XPS) analysis.

As Ti dopant was added during the nucleation of Ti-FeOOH process, there is no significant difference in the content of Ti between $\text{Ti-Fe}_2\text{O}_3(\mathbf{t})$ and $\text{Ti-Fe}_2\text{O}_3(\mathbf{T})$ (**Figure 2-7b**). Then, we investigated the presence of unintentional Sn dopant from the FTO (fluorine-doped tin oxide) substrate during the high-temperature annealing process^{21,22}, which is often neglected in many studies. As shown in **Figure 2-7c**, we detected Sn peaks in both $\text{Ti-Fe}_2\text{O}_3(\mathbf{t})$ and $\text{Ti-Fe}_2\text{O}_3(\mathbf{T})$ and discovered the higher Sn content in $\text{Ti-Fe}_2\text{O}_3(\mathbf{t})$ (4.88%) compared to $\text{Ti-Fe}_2\text{O}_3(\mathbf{T})$ (2.21%). Further confirmation of higher Sn content in $\text{Ti-Fe}_2\text{O}_3(\mathbf{t})$ was obtained using Time-of-Flight Secondary Ion Mass Spectrometry (TOF-SIMS) in **Figure 2-8**. It is due to the shorter Sn diffusion pathway of $\text{Ti-Fe}_2\text{O}_3(\mathbf{t})$, as depicted in **Figure 2-7d**.

In previous reports, the excess metal dopants in hematite can lead to high charge recombination rate by creating extra energy levels between conduction and valence band.^{23,24} Based on the XPS and TOF-SIMS results, we have concluded that the poor PEC activities of $\text{Ti-Fe}_2\text{O}_3(\mathbf{t})$ are primarily due to the increased number of metal dopants in the surface region. To figure out the effect of higher Sn content in hematite photoanode, the surface (η_{surface}) and bulk (η_{bulk}) charge separation efficiencies were measured by the J-V curves with a 1.0 M NaOH electrolyte solution including $0.2 \text{ M Na}_2\text{SO}_3$ as the hole scavenger. In **Figures 2-7e,f**, $\text{Ti-Fe}_2\text{O}_3(\mathbf{t})$ with higher Sn content at the surface region, showed lower surface charge separation efficiency and higher bulk charge separation efficiency compared to $\text{Ti-Fe}_2\text{O}_3(\mathbf{T})$. The higher photocurrent density of $\text{Ti-Fe}_2\text{O}_3(\mathbf{t})$ than that of $\text{Ti-Fe}_2\text{O}_3(\mathbf{T})$ under the back-illumination condition confirms the high charge separation efficiency of $\text{Ti-Fe}_2\text{O}_3(\mathbf{t})$ in the bulk region (**Figure 2-9**). It means that the higher Sn content of $\text{Ti-Fe}_2\text{O}_3(\mathbf{t})$ can increase the conductivity of hematite in the bulk region by increasing donor density and vacancies, while it also creates recombination sites at the surface region. Therefore, it is crucial to suppress unintentional Sn doping at

the surface region to achieve high PEC activities.

2.3.3 Non-metallic Si doping effect on Ti-Fe₂O₃(t)

To control the metal (especially Sn) dopability at the surface region and systematically reduce recombination, we carried out non-metal Si doping into Ti-Fe₂O₃(t). Previous studies have suggested that non-metallic atom doping can reduce the excess metal dopants in hematite surface.^{25,26} To achieve non-metallic Si-doping, we coated the sample with a SiO_x overlayer and annealed it at a high temperature.²⁷ Because of the Si doping from the SiO_x overlayer, the Sn diffusion from the FTO substrate was suppressed, leading to a less Sn content at the surface region, as shown in **Figure 2-11a**.

To observe each element of Ti-Fe₂O₃(t) and Si-doped Ti-Fe₂O₃(t) (Ti:Si-Fe₂O₃(t)), XPS analysis was performed. The presence of Si was confirmed by the Si 2*p* peak at 101.9 eV of Ti:Si-Fe₂O₃(t) in **Figure 2-11b**. After etching the SiO_x overlayer of Ti:Si-Fe₂O₃(t) using a concentrated NH₄HF₂ and HF solution, the atomic percent of Si was estimated to ~1.5% (**Figure 2-13**).²⁸ Notably, the intensity of Ti 2*p* and Sn 3*d* peaks in Ti:Si-Fe₂O₃(t) were considerably reduced after Si-doping. After Si doping, the atomic percent of Ti and Sn was reduced from 1.16% to 0.76% (Ti⁴⁺) and 4.88% to 1.48% (Sn⁴⁺), respectively, indicating that Si doping can regulate the concentration of metal dopants on the surface of hematite, as confirmed in **Figures 2-11c,d**. The schematic diagram of the atomic arrangement in **Figure 2-11a** demonstrates that the overall metallic Ti and Sn content in the surface region is lower in Ti:Si-Fe₂O₃(t) by introducing non-metallic Si atoms. The Fe 2*p* spectra of Ti-Fe₂O₃(t) and Ti:Si-Fe₂O₃(t) at 710.9 eV and 724.5 eV, which correspond to Fe 2*p*_{3/2} and Fe 2*p*_{1/2}, respectively, were used to confirm the reduced content of Ti and Sn, as illustrated in **Figure 2-11e**. Previous studies have suggested that the Fe²⁺ state is related to a concentration of high-valent metal dopants, which is introduced to preserve the charge neutrality.²⁹⁻³¹ Consequently, the lower intensity of Fe²⁺ (716 eV) peak implies a smaller amount of Ti⁴⁺ and Sn⁴⁺ dopants at the surface region of Ti:Si-Fe₂O₃(t).

By Si doping, Ti:Si-Fe₂O₃(t) have different dopant ratio of metallic and non-metallic dopants at the surface and bulk region. Thus, an internal electric field was created, leading to easy hole extraction. To confirm it, the energy band structure was calculated from the results of XPS and Tauc plot (**Figure 2-14**). As shown in **Figure 2-15**, Ti:Si-Fe₂O₃(t) had 0.27 eV higher valence band maximum (VBM) compared to Ti-Fe₂O₃(t), indicating the creation of an internal electric field and fast charge separation efficiency. In the transient photocurrent density curve (0.001 point/s) at 1.23 V_{RHE} (**Figure 2-11f**), Ti:Si-Fe₂O₃(t) exhibited a smaller spike than Ti-Fe₂O₃(t) after the instantaneous light-on, proving the excellent charge transfer property at the surface region (**Figure 2-11f**). Also, after Si doping, Ti:Si-Fe₂O₃(t) has a

higher carrier density compared to Ti-Fe₂O₃(t), which is illustrated in Mott-Schottky plots in **Figure 2-11g**.

2.3.4 PEC activities of NiFeO_x@Ti:Si-Fe₂O₃(t)

Figure 2-16a illustrates a comparison of the PEC water oxidation efficiency of the samples under 1 SUN (AM 1.5 G) and dark conditions in 1.0 M NaOH using a three-electrode system. Ti:Si-Fe₂O₃(t) showed a photocurrent density of 2.36 mA cm⁻² at 1.23 V_{RHE}, which is 2.1-fold higher than that of Ti-Fe₂O₃(t) (1.1 mA cm⁻²). An efficient oxygen evolution reaction (OER) catalyst, NiFeO_x, was deposited on the surface of Ti:Si-Fe₂O₃(t) by a photochemical method³² to increase the surface charge transfer. The thickness of the NiFeO_x overlayer was controlled to maintain its original transparent property (**Figure 2-17**).

The similar morphological features and the same lattice spacings of Ti:Si-Fe₂O₃(t) and NiFeO_x@Ti:Si-Fe₂O₃(t) were revealed in scanning electron microscope (SEM) and high-resolution transmission electron microscope (HR-TEM) images, respectively in **Figures 2-19,16b**. These results imply that the hematite's lattice remains unchanged after NiFeO_x deposition. Additionally, high-angle annular dark-field scanning TEM-energy-dispersive spectroscopy (HAADF-STEM-EDS) mapping images in **Figure 2-20** revealed the uniform deposition of NiFeO_x.

Both Ti:Si-Fe₂O₃(t) and NiFeO_x@Ti:Si-Fe₂O₃(t) showed similar light absorption properties, which can be attributed to the high transparency of the NiFeO_x co-catalyst (**Figure 2-21**), despite the SiO_x amorphous overlayer thickening from 1-2 nm to 2-4 nm after NiFeO_x deposition (**Figure 2-16b**). The additional XPS characterization of NiFeO_x@Ti:Si-Fe₂O₃(t) was presented in **Figure 2-22**.

NiFeO_x co-catalyst deposition on hematite not only resulted in a high photocurrent density of 2.6 mA cm⁻² at 1.23 V_{RHE} but also reduced the onset potential to 0.71 V_{RHE}, making it suitable for a tandem system. To the best of our knowledge, this value is the highest photocurrent density achieved to date for thin film hematite under 100 nm thickness (**Table 2-1**). NiFeO_x@Ti:Si-Fe₂O₃(t) exhibited an improved surface (η_{surface}) and bulk (η_{bulk}) charge separation efficiencies of 72% and 21%, respectively (**Figures 2-16c,d**) and showed reduced R_{trap} and R_{ct} values in Nyquist plot (**Figure 2-16e**)³³, which are related to the rate of trapping holes of surface states and the charge transfer resistance between electrolyte/hematite interfaces, respectively, compared to other samples. These electrochemical data demonstrated the Si doping and NiFeO_x co-catalyst deposition effect at the surface and bulk region. The incident photon to current conversion efficiency (IPCE) was measured to evaluate the photoconversion efficiency of hematite in **Figure 2-16f** and NiFeO_x@Ti:Si-Fe₂O₃(t) showed improved photo-response

in the range of 300 to 500 nm.

To enhance the PEC activities and fully utilize the high transparency of $\text{NiFeO}_x@\text{Ti:Si-Fe}_2\text{O}_3(\text{t})$ which shows better transparency than single $\text{Ti-Fe}_2\text{O}_3(\text{T})$, $\text{NiFeO}_x@\text{Ti:Si-Fe}_2\text{O}_3(\text{t})$ was assembled. As shown in **Figure 2-16g**, dual $\text{NiFeO}_x@\text{Ti:Si-Fe}_2\text{O}_3(\text{t})$ achieved a maximum photocurrent density of 4.0 mA cm^{-2} at $1.23 \text{ V}_{\text{RHE}}$ due to better light transparency in the wavelength of 300-500 nm and showed good stability for 8 hours (**Figure 2-16h**).

2.3.5 Dual $\text{NiFeO}_x@\text{Ti:Si-Fe}_2\text{O}_3(\text{t})/\text{PSC}$ tandem cell

Figure 2-24a shows the schematic configuration of a hematite/PSC tandem cell. Utilization of the photovoltage from PSC instead of the external voltage, the hydrogen and oxygen are generated from the counter electrode (Pt) and the working electrode (hematite), respectively. The J_{op} value of the dual $\text{NiFeO}_x@\text{Ti:Si-Fe}_2\text{O}_3(\text{t})/\text{PSC}$ tandem cell was estimated to 3.65 mA cm^{-2} , which is 1.51-fold higher than that of a single $\text{NiFeO}_x@\text{Ti:Si-Fe}_2\text{O}_3(\text{t})/\text{PSC}$ tandem cell (**Figure 2-24b**). The feasibility of unbiased water splitting in tandem cells was verified by testing it in a 1.0 M NaOH electrolyte in three-electrode and two-electrode systems under 1 SUN (**Figure 2-24c**). The J_{op} values of tandem cells in **Figure 2-24b** closely match with the photocurrent density values in J-t measurement (**Figure 2-24c**), confirming that the tandem cell worked well. The dual $\text{NiFeO}_x@\text{Ti:Si-Fe}_2\text{O}_3(\text{t})/\text{PSC}$ tandem cell reached a solar-to-hydrogen (STH) conversion efficiency of 4.49% in an unbiased system, which is the highest value achieved in hematite/PSC tandem cells (**Table 2-3**). In **Figure 2-24d**, $\text{NiFeO}_x@\text{Ti:Si-Fe}_2\text{O}_3(\text{t})$ showed a high faradaic efficiency of 90-92% for 3 hours. The remarkable performance of tandem cells in this study was attributed to the utilization of highly transparent dual thin film hematite modified by Si doping and NiFeO_x deposition.

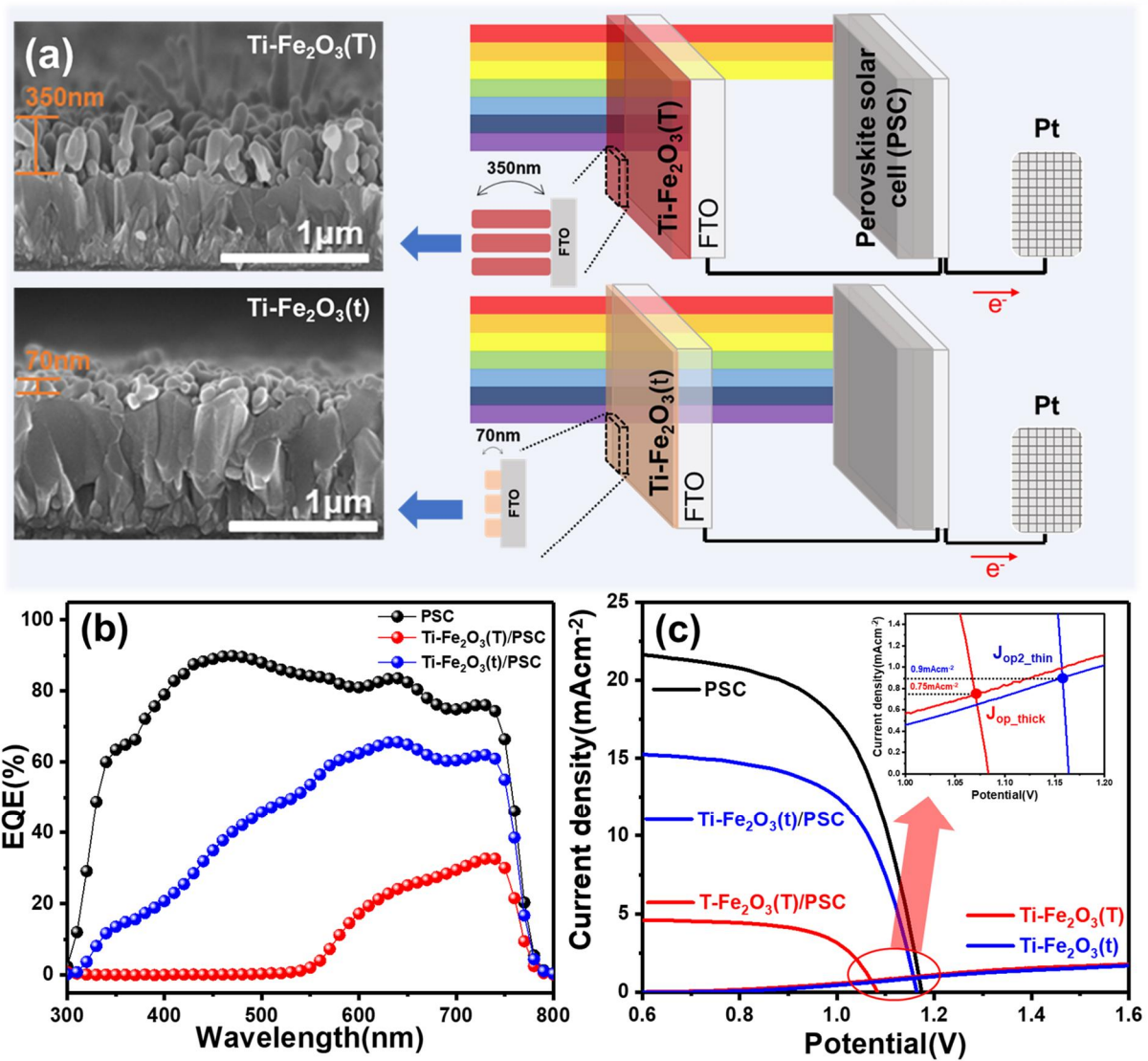


Figure 2-1. Hematite photoanode and PSC tandem cells. (a) SEM images of $\text{Ti-Fe}_2\text{O}_3(\text{t})$ and $\text{Ti-Fe}_2\text{O}_3(\text{T})$ (left) and scheme for hematite/PSC tandem cell (right). (b) EQE of PSC and PSC behind hematite photoanodes ($\text{Ti-Fe}_2\text{O}_3(\text{t})/\text{PSC}$ and $\text{Ti-Fe}_2\text{O}_3(\text{T})/\text{PSC}$). (c) J-V curves of PSC and hematite photoanodes together under light illumination.

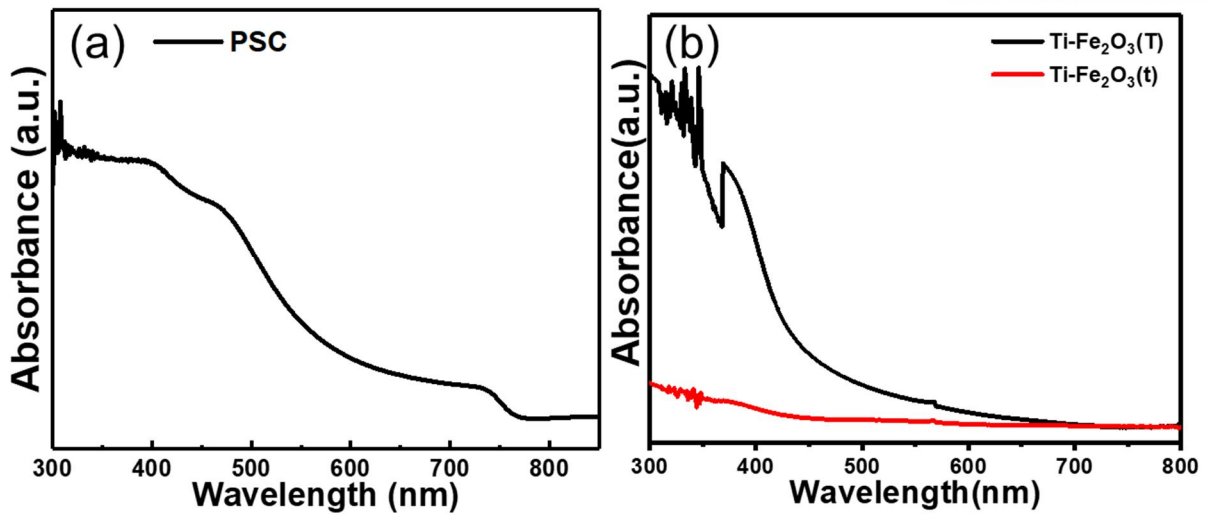


Figure 2-2. UV-Vis spectra of (a) PSC and (b) Ti-Fe₂O₃(T) and Ti-Fe₂O₃(t).

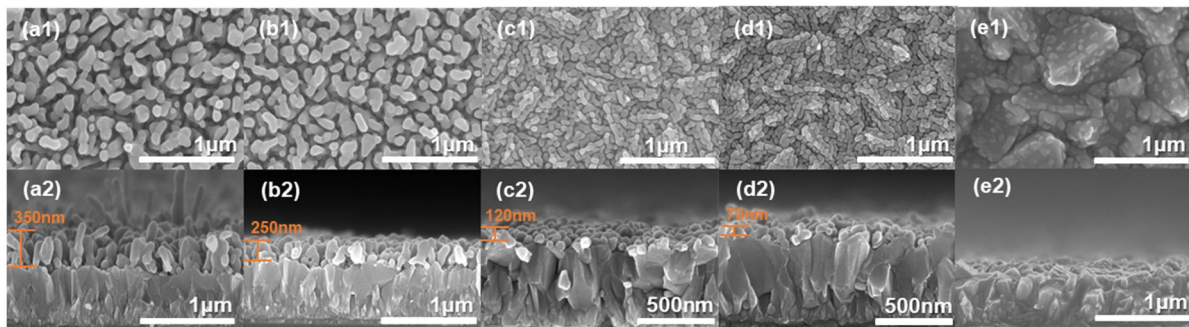


Figure 2-3. Top and cross-section SEM images of Ti-Fe₂O₃#1 to Ti-Fe₂O₃#5 (a:Ti-Fe₂O₃#1 b: Ti-Fe₂O₃#2 c: Ti-Fe₂O₃#3 d: Ti-Fe₂O₃#4 e: Ti-Fe₂O₃#5. Ti-Fe₂O₃#1-#5).

Note: We fabricated hematite photoanodes with various thicknesses ranging from 350 to 10 nm by controlling the concentration of FeCl₃·6H₂O (150 mM Ti-Fe₂O₃#1, 100 mM Ti-Fe₂O₃#2, 50mM Ti-Fe₂O₃#3, 30 mM Ti-Fe₂O₃#4, and 10 mM Ti-Fe₂O₃#5). Considering the transmittance and photocurrent density, we selected Ti-Fe₂O₃#4 (Ti-Fe₂O₃(t)) with a thickness of 70 nm as the optimal choice for tandem cells. As a reference for comparison, we used Ti-Fe₂O₃#1 (Ti-Fe₂O₃(T)) with a thickness of 350 nm.

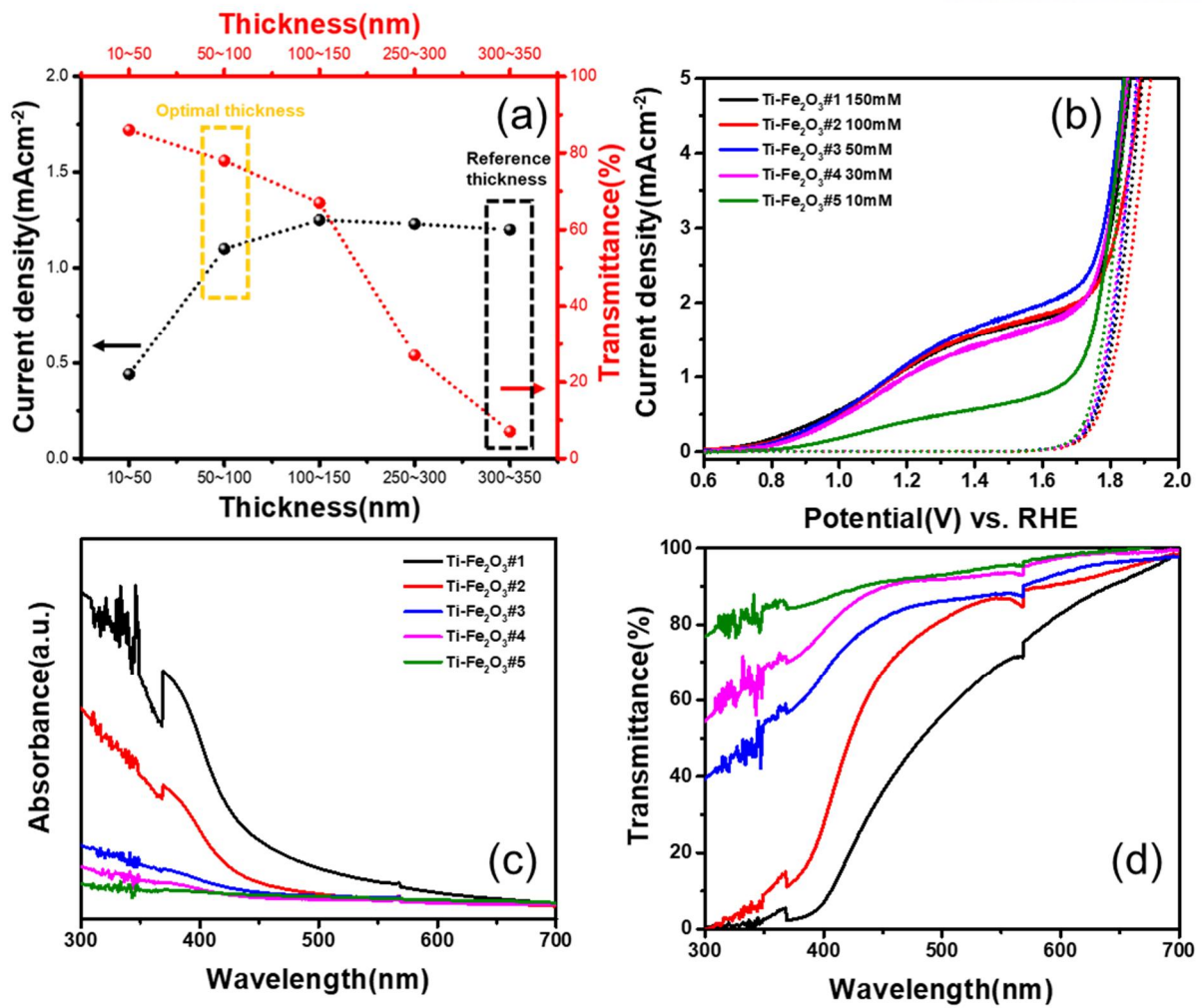


Figure 2-4. (a) Current density at 1.23 V_{RHE} and maximum transmittance at 400 nm for different thicknesses. (b) J-V curves, (c) UV-Vis absorption spectra, and (d) Transmittance (%) of Ti-Fe₂O₃#1 to #5.

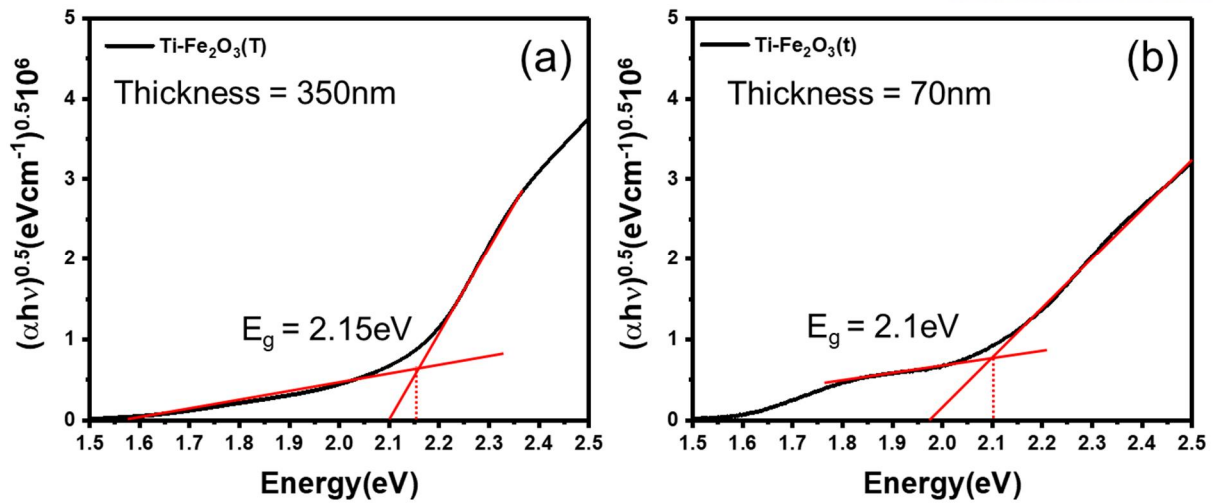


Figure 2-5. Tauc plot of (a) Ti-Fe₂O₃(T) and (b) Ti-Fe₂O₃(t).

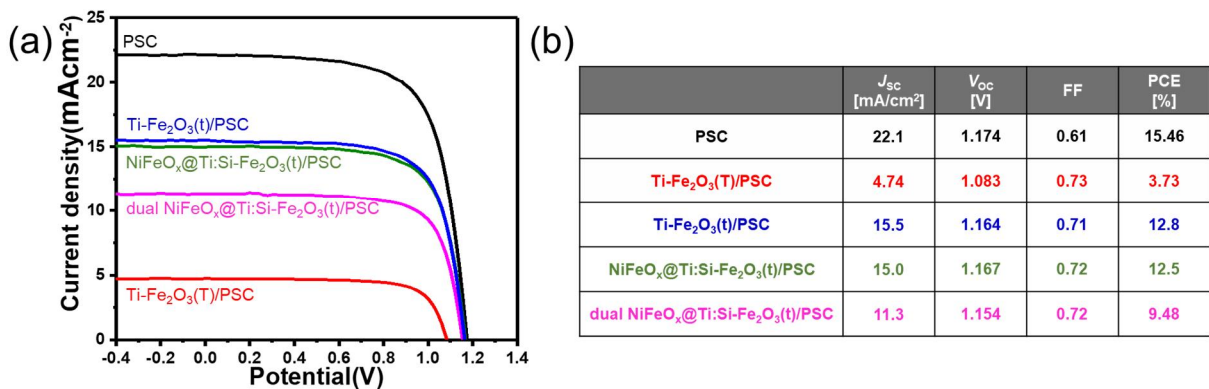


Figure 2-6. (a) J-V curves and (b) photovoltaic parameters of PSC and PSCs behind hematite photoanodes.

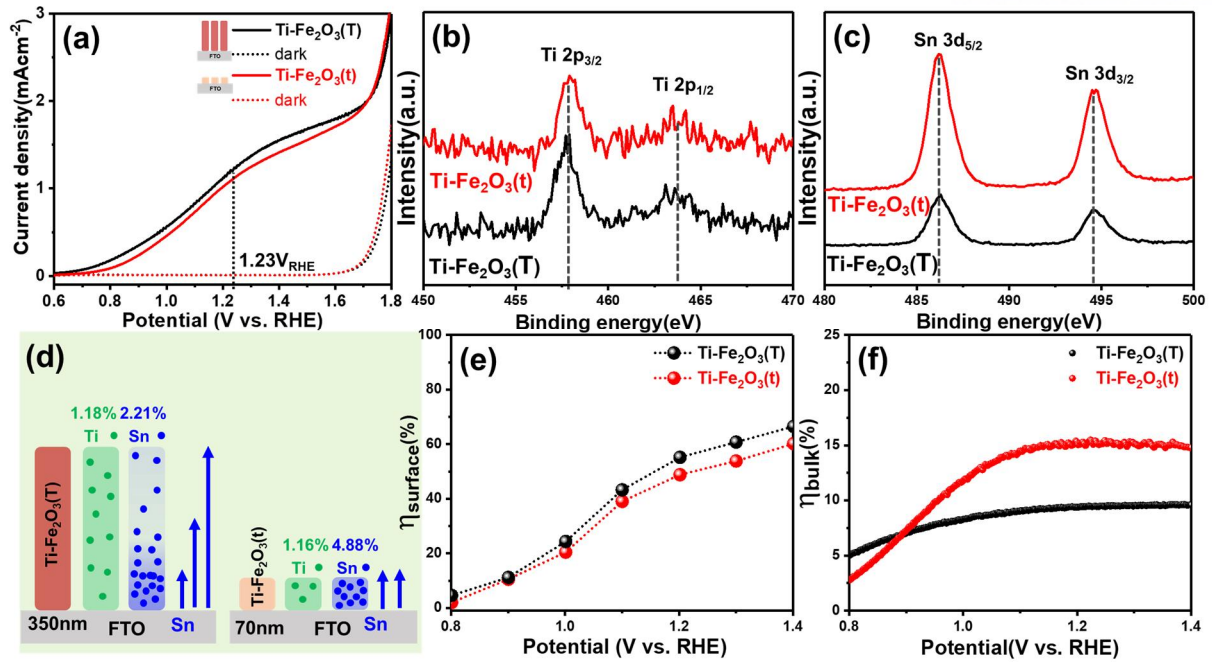


Figure 2-7. PEC activities of Ti-Fe₂O₃(T) and Ti-Fe₂O₃(t). (a) J-V curves under light and dark conditions, XPS spectra of (b) Ti 2*p* and (c) Sn 3*d*, (d) schematics of the Sn and Ti content, and charge separation efficiencies at the (e) surface region (η_{surface}) and (f) bulk (η_{bulk}) region of Ti-Fe₂O₃(T) and Ti-Fe₂O₃(t).

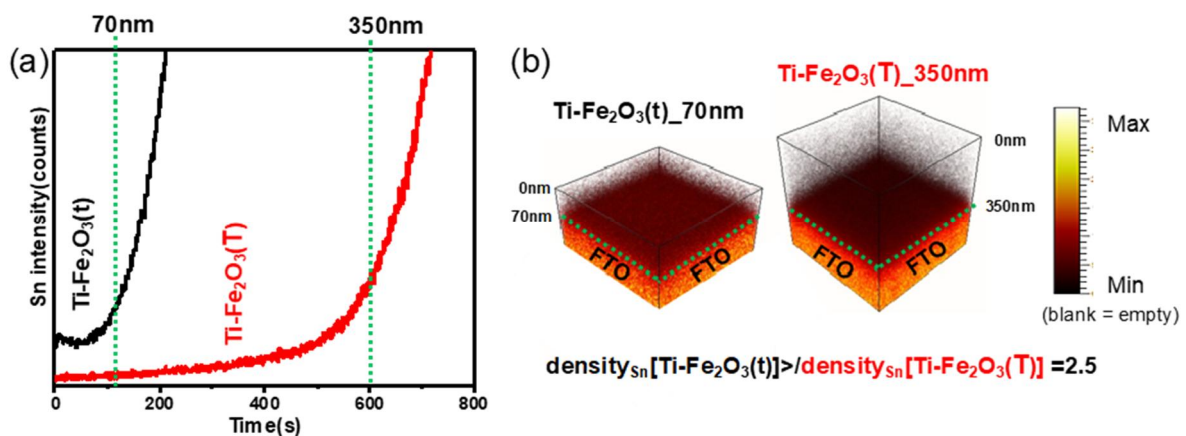


Figure 2-8. (a) TOF-SIMS depth profiles and (b) TOF-SIMS 3D images of Sn (TOF-SIMS etching rate: ~ 0.6 nm/s).

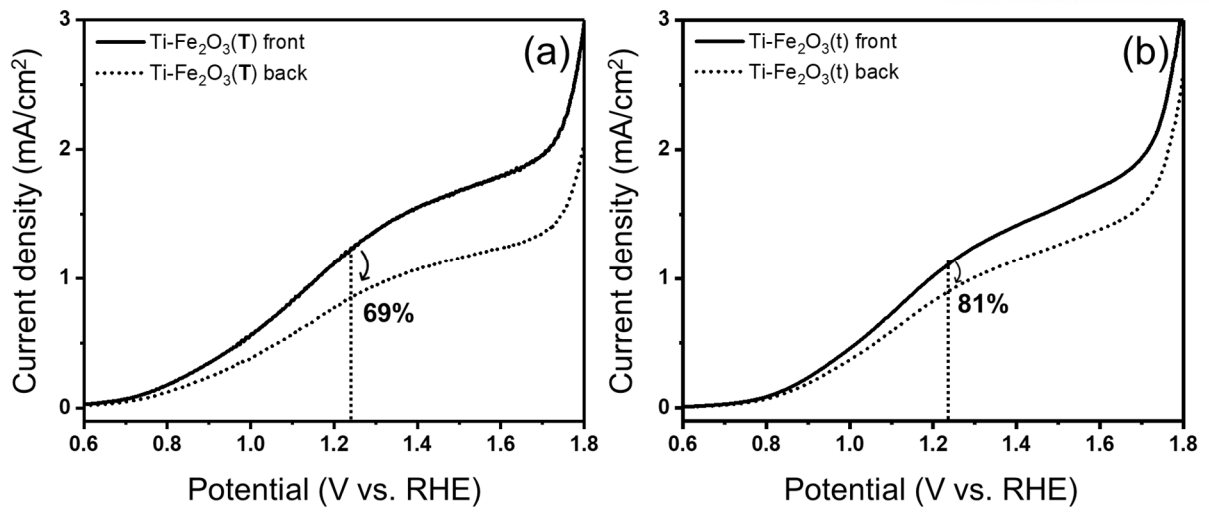


Figure 2-9. J-V curves under the front and back light conditions of (a) Ti-Fe₂O₃(T) and (b) Ti-Fe₂O₃(t).

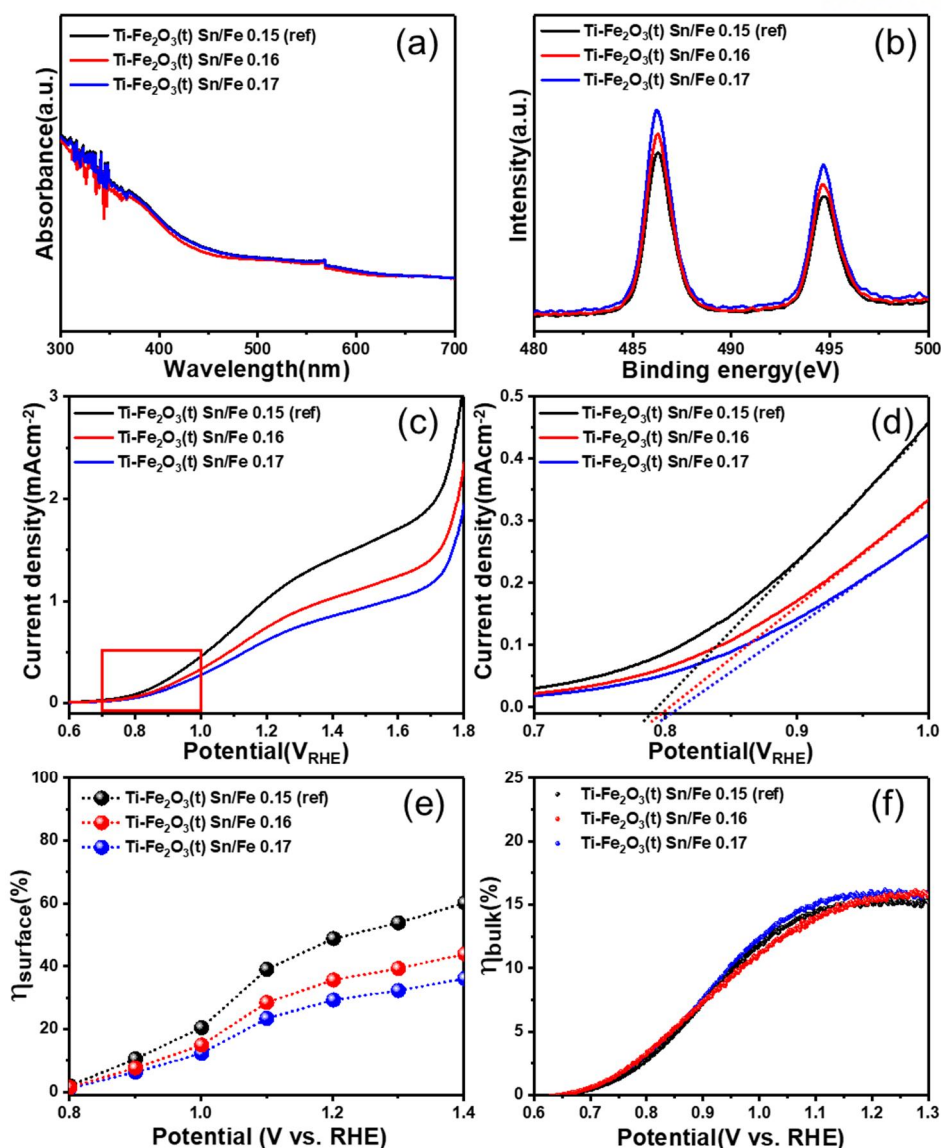


Figure 2-10. Comparison of electrochemical properties of Ti-Fe₂O₃(t) with different Sn content. (a) UV-Vis absorption spectra, (b) XPS spectra of Sn 3d, (c) J-V curves, (d) close-up data in the rectangular region in **Figure 2-10c**, and charge separation efficiencies at the (e) surface region (η_{surface}) and (f) bulk region (η_{bulk}) of Ti-Fe₂O₃(t) with different Sn/Fe ratio.

Note: Ti-Fe₂O₃(t) with the Sn/Fe ratio of 0.15 is the reference sample that we used in this study. Ti-Fe₂O₃(t) with higher Sn content with the Sn/Fe ratio of 0.16 and 0.17 showed lower PEC activities compared to that of reference Ti-Fe₂O₃(t) (**Figures 2-10c,d**). It elucidates that the excess Sn content in hematite photoanodes reduces the PEC activities by lowering the surface charge separation efficiencies while the bulk charge separation efficiencies remain constant (**Figures 2-10e,f**).

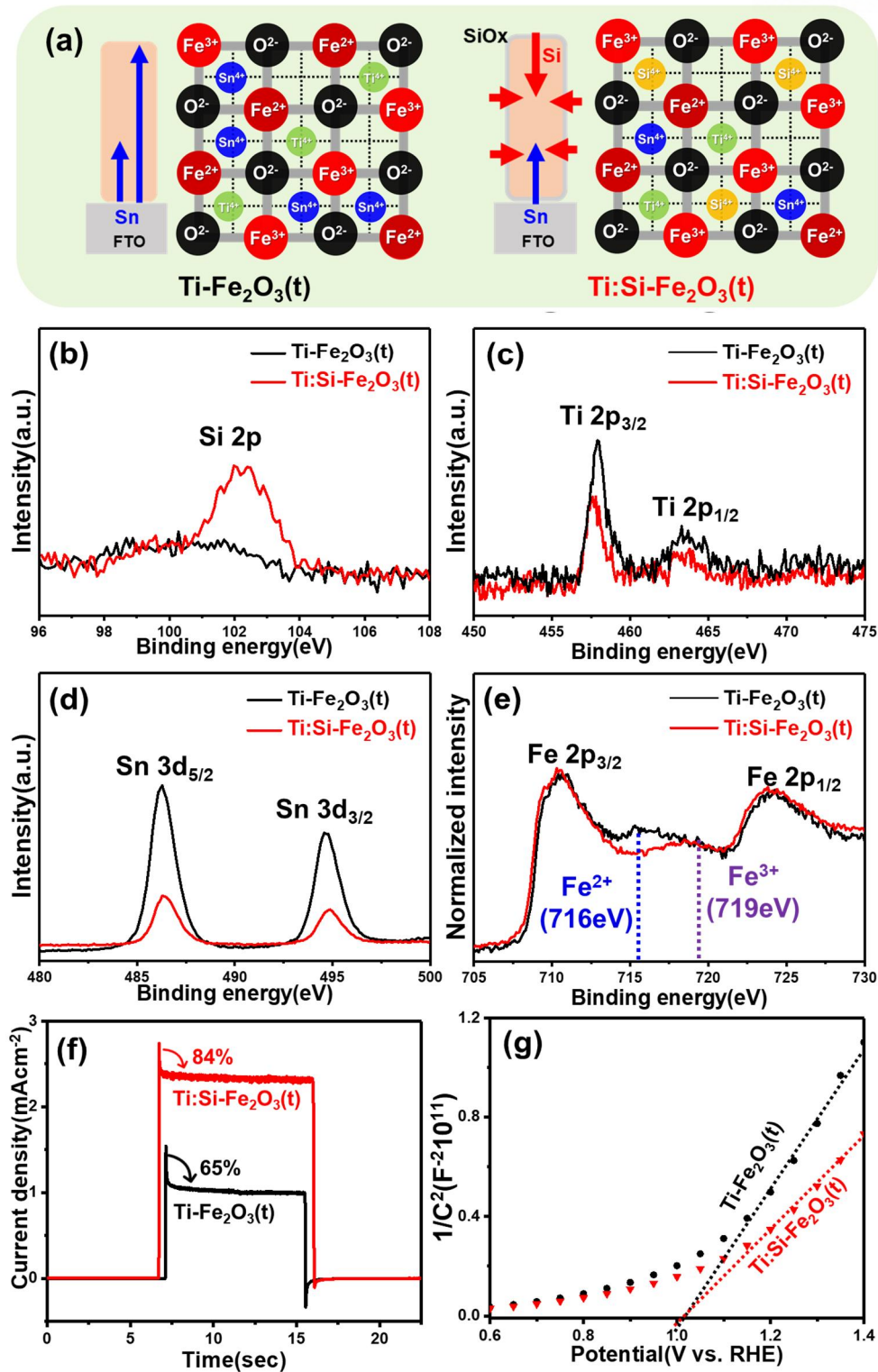


Figure 2-11. (a) Schematics of atomic distribution, XPS spectra of (b) $\text{Si } 2p$, (c) $\text{Ti } 2p$, (d) $\text{Sn } 3d$, and (e) $\text{Fe } 2p$, (f) transient photocurrent density curves, and (g) Mott-Schottky plots of $\text{Ti-Fe}_2\text{O}_3(\text{t})$ and $\text{Ti-Fe}_2\text{O}_3(\text{T})$.

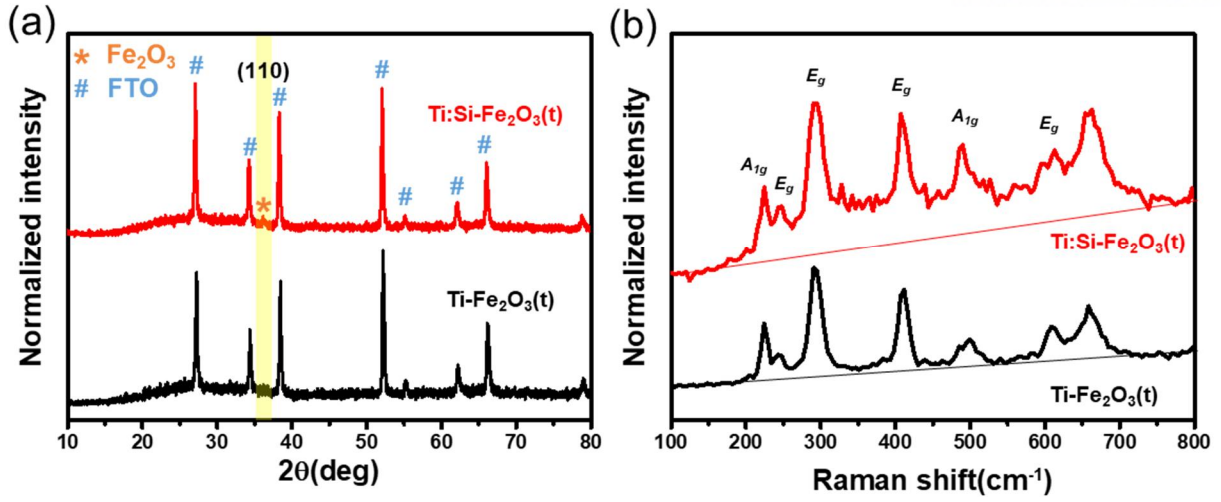


Figure 2-12. (a) XRD and (b) Raman spectra of Ti-Fe₂O₃(t) and Ti:Si-Fe₂O₃(t).

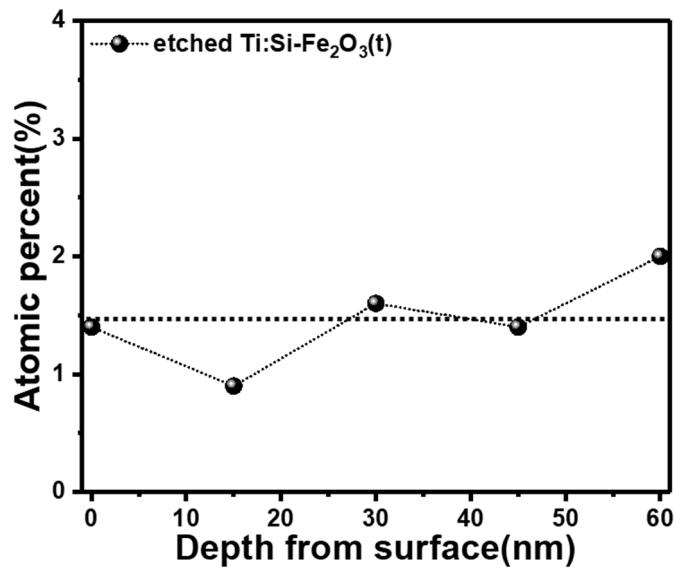


Figure 2-13. XPS depth profile of Ti:Si-Fe₂O₃(t) after removing SiO_x overlayer.

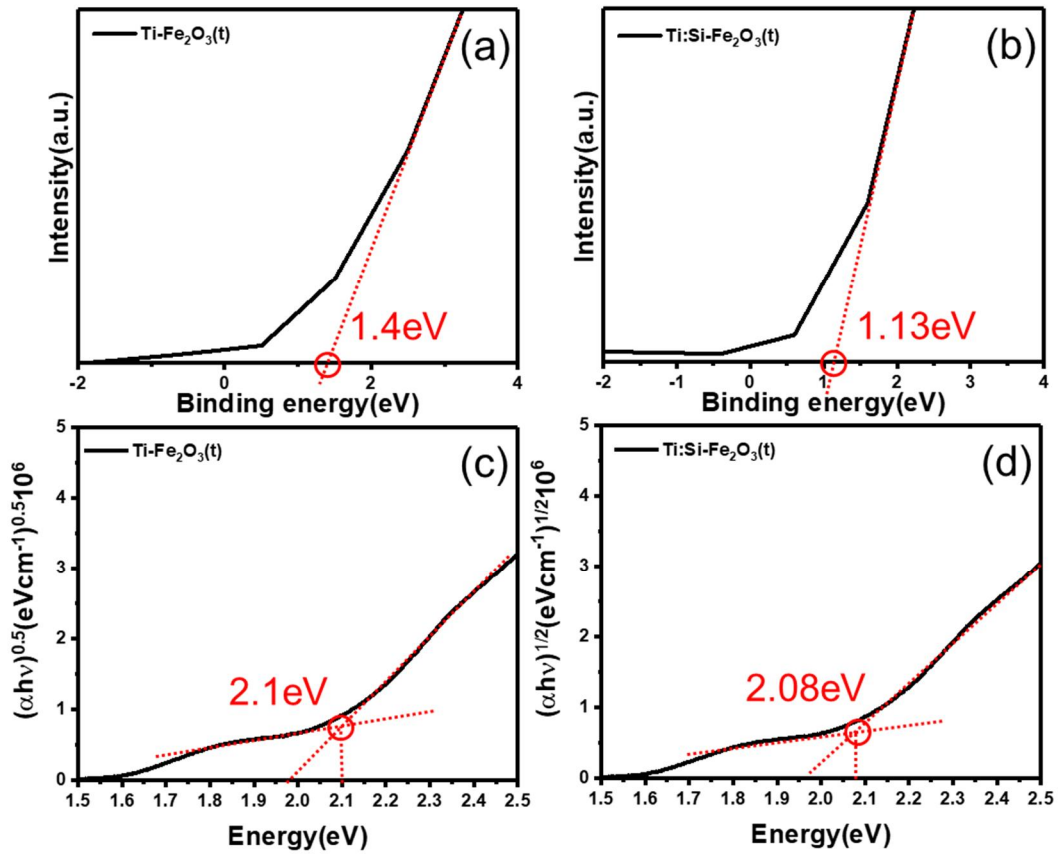


Figure 2-14. (a-b) VBM and (c-d) Tauc plot of Ti-Fe₂O₃(t) and Ti:Si-Fe₂O₃(t).

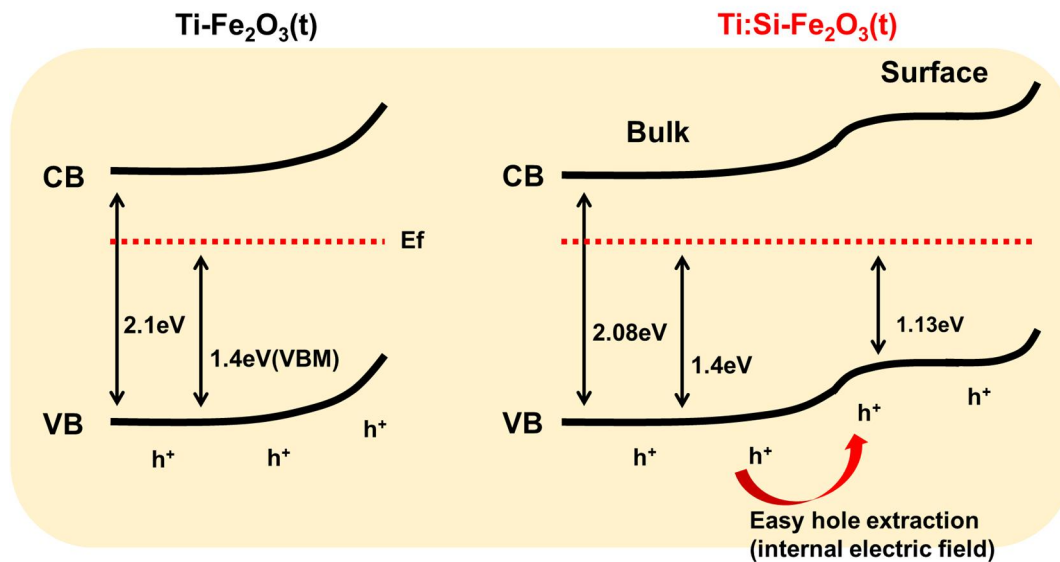


Figure 2-15. Schematic energy diagram of Ti-Fe₂O₃(t) and Ti:Si-Fe₂O₃(t).

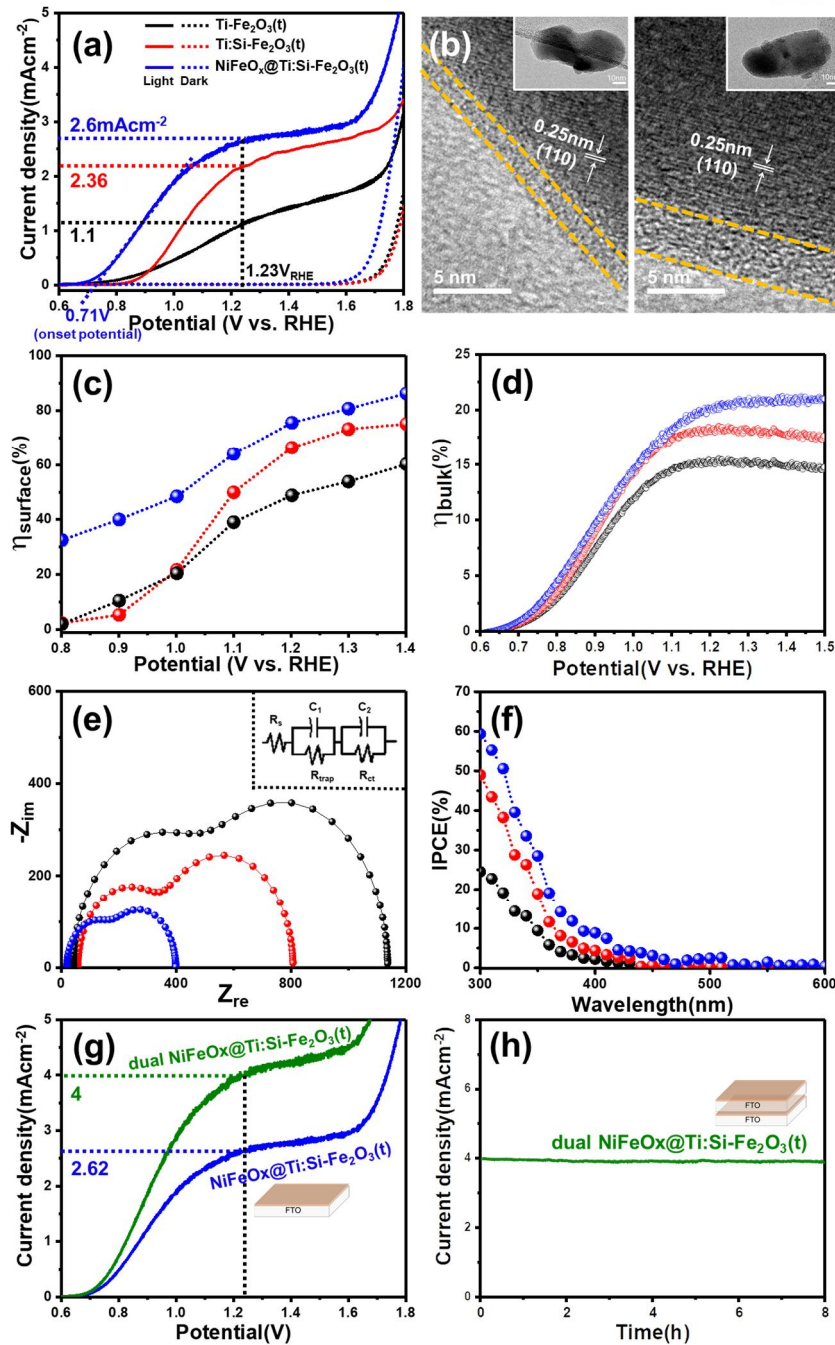


Figure 2-16. PEC activities after non-metallic Si doping and NiFeO_x deposition on Ti-Fe₂O₃(t). (a) J-V curves under light and dark conditions, TEM images of (b) Ti:Si-Fe₂O₃(t) (left) and NiFeO_x@Ti:Si-Fe₂O₃(t) (right) (inset images show the low magnification TEM images of each sample), charge separation efficiencies at the (c) surface region (η_{surface}) and (d) bulk region (η_{bulk}), (e) EIS spectra at 1.23 V_{RHE}, and (f) IPCE spectra at 1.23 V_{RHE} of Ti-Fe₂O₃(t), Ti:Si-Fe₂O₃(t), and NiFeO_x@Ti:Si-Fe₂O₃(t). (g) J-V curves, (h) J-t measurement at 1.23 V_{RHE} during 8 h of single and dual NiFeO_x@Ti:Si-Fe₂O₃(t).

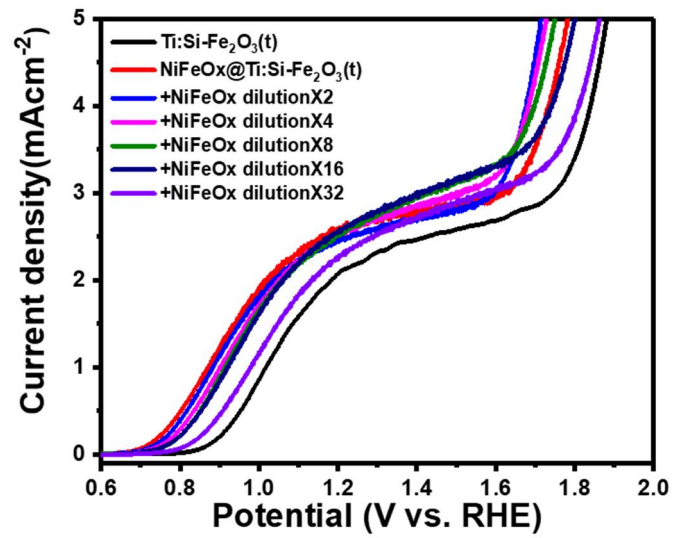


Figure 2-17. J-V curves of NiFeO_x@Ti:Si-Fe₂O₃(t) with different dilution concentration of NiFeO_x (dilution X2 = pristine NiFeO_x solution : hexane = 1:1 (v:v), dilutionX4 = NiFeO_x dilutionX2 solution : hexane = 1:1 (v:v))

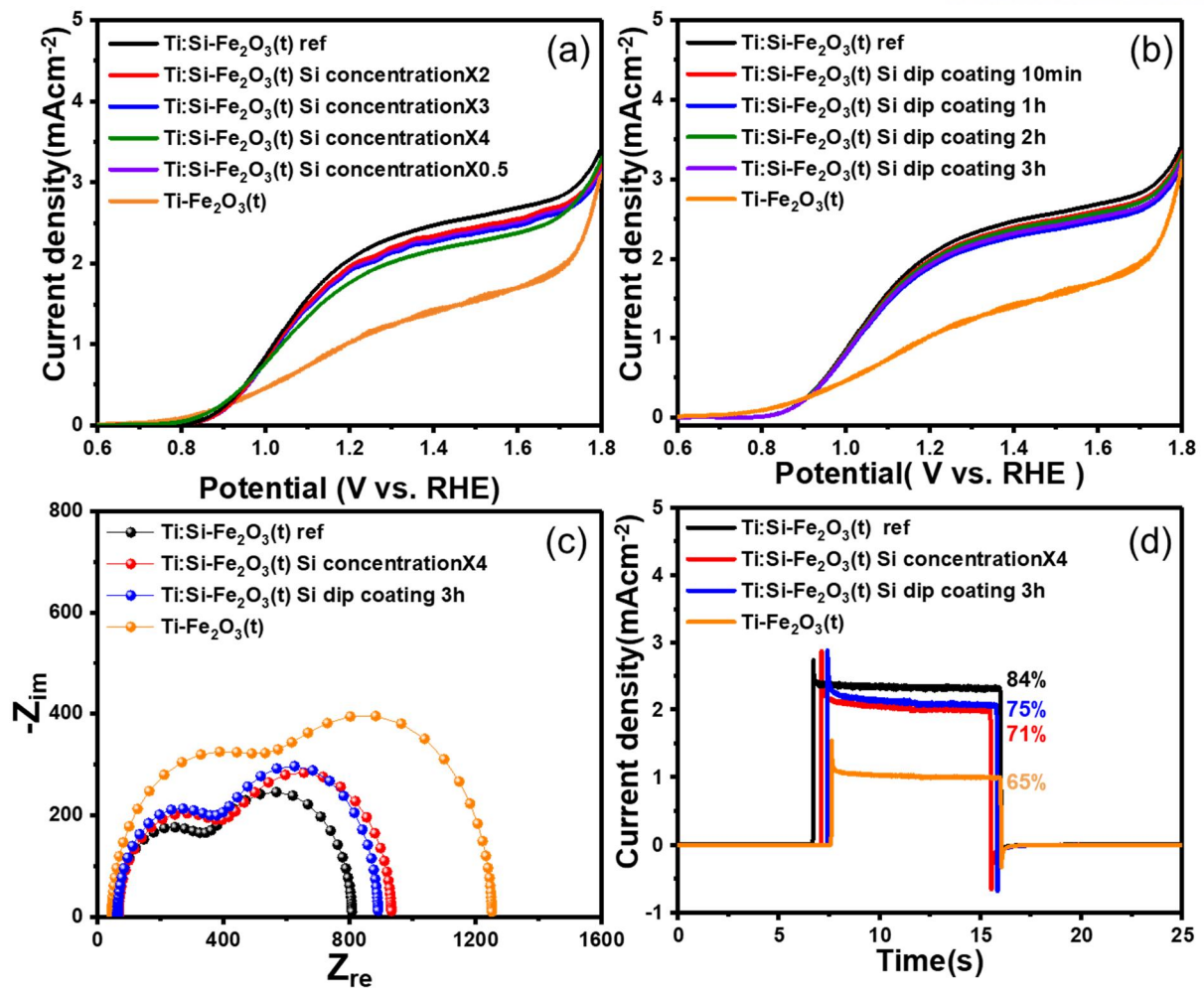


Figure 2-18. J-V curves of Ti:Si-Fe₂O₃(t) with (a) different concentration and (b) dip coating time of APTMS (Si precursor) solution. (c) EIS spectra and (d) transient photocurrent density curves at 1.23 V_{RHE} of optimized hematite photoanodes at separate conditions.

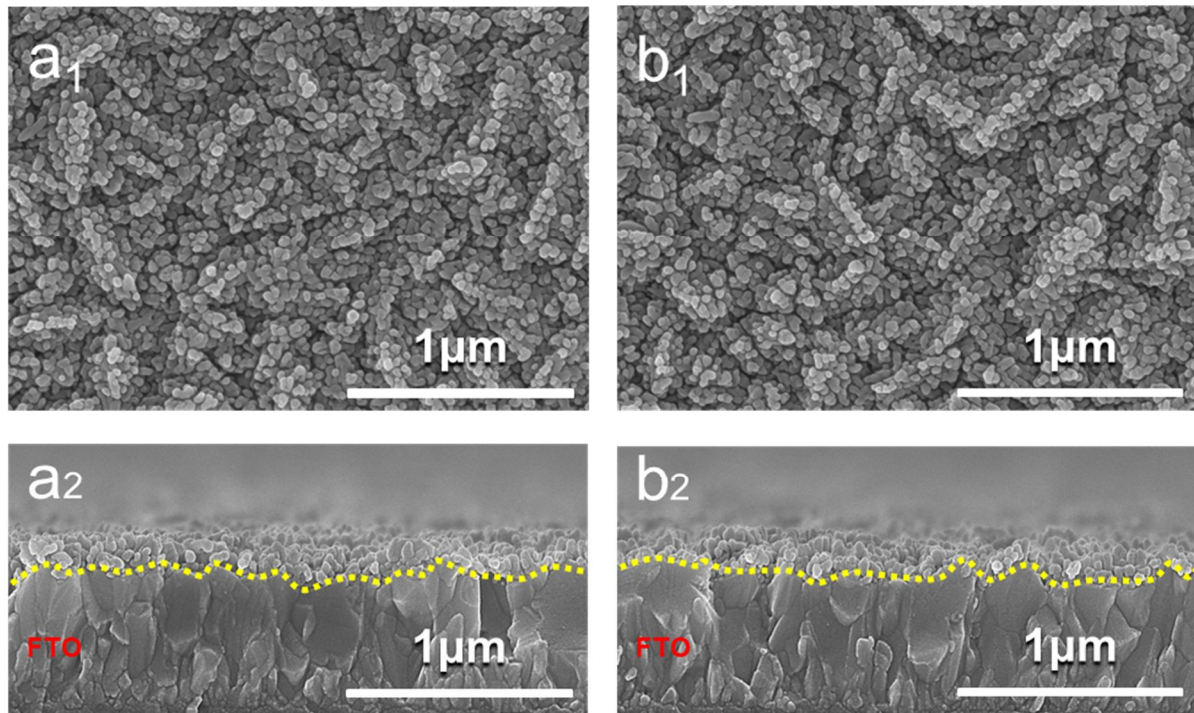


Figure 2-19. Top and cross-section SEM images of (a₁-a₂) Ti:Si-Fe₂O₃(t) and (b₁-b₂) NiFeO_x@Ti:Si-Fe₂O₃(t).

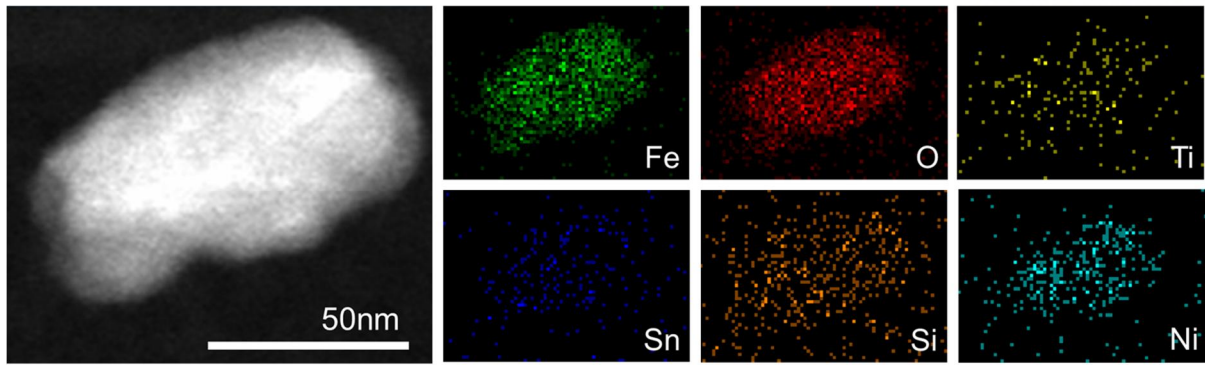


Figure 2-20. HAADF-STEM and EDS elemental mapping images of $\text{NiFeO}_x@ \text{Ti:Si-Fe}_2\text{O}_3(\text{t})$

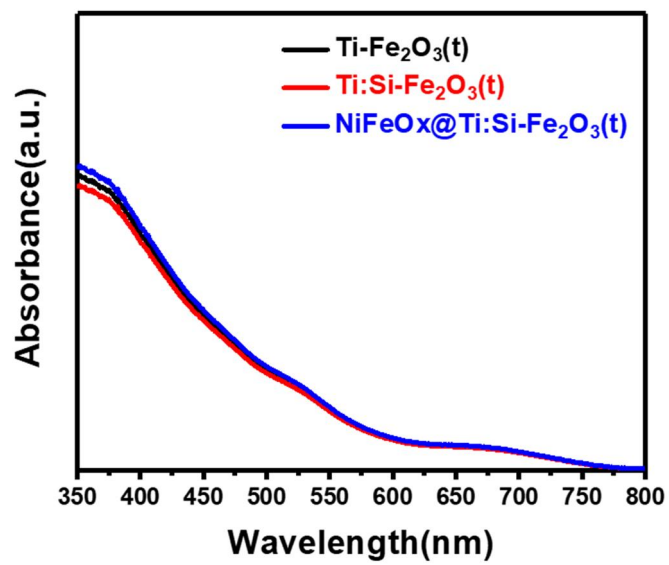


Figure 2-21. UV-Vis absorption spectra of $\text{Ti-Fe}_2\text{O}_3(\text{t})$, $\text{Ti:Si-Fe}_2\text{O}_3(\text{t})$, and $\text{NiFeO}_x@ \text{Ti:Si-Fe}_2\text{O}_3(\text{t})$.

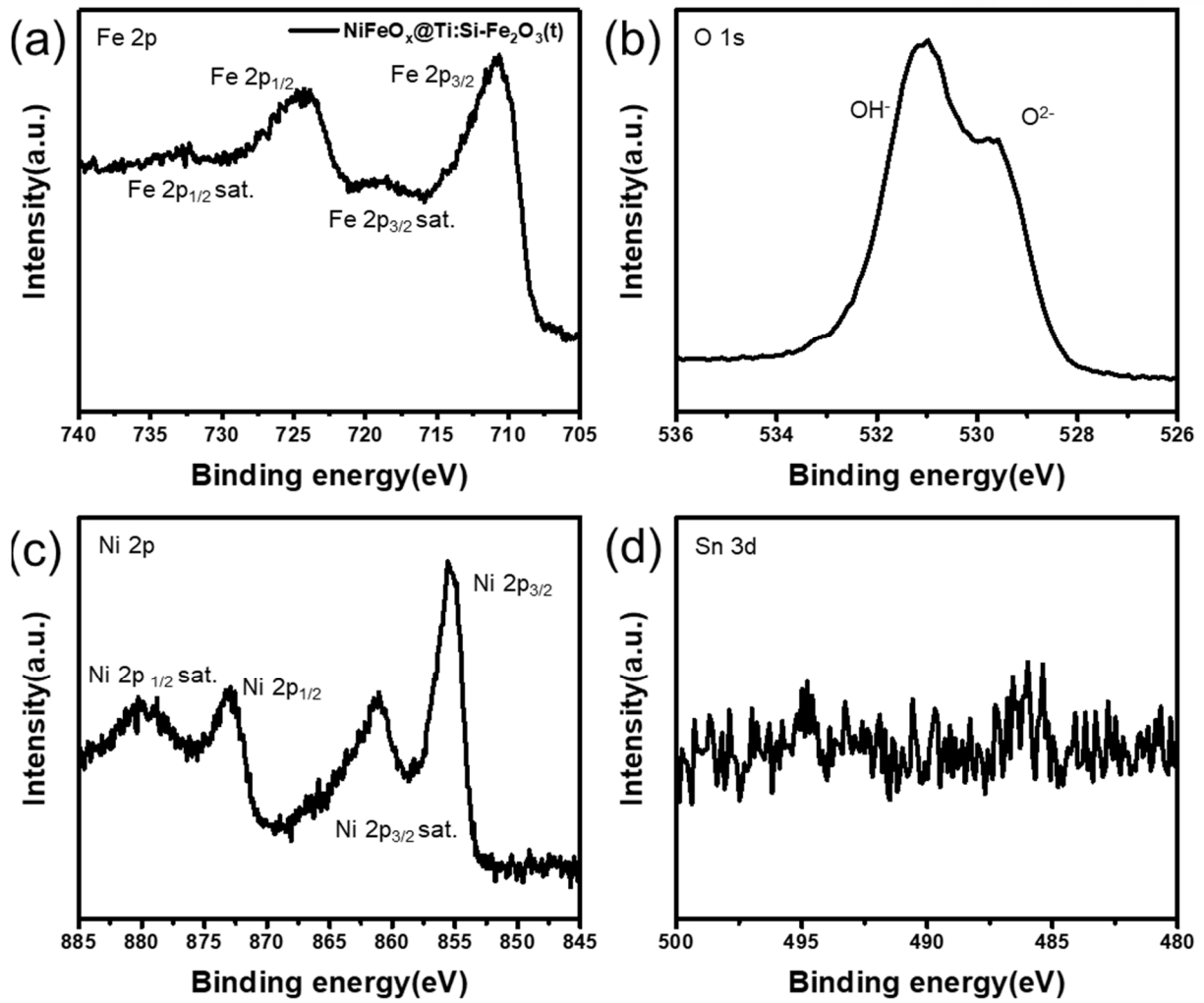


Figure 2-22. XPS spectra (a) Fe 2p, (b) O 1s, (c) Ni 2p, and (d) Ti 2p of $\text{NiFeO}_x@\text{Ti:Si-Fe}_2\text{O}_3(\text{t})$.

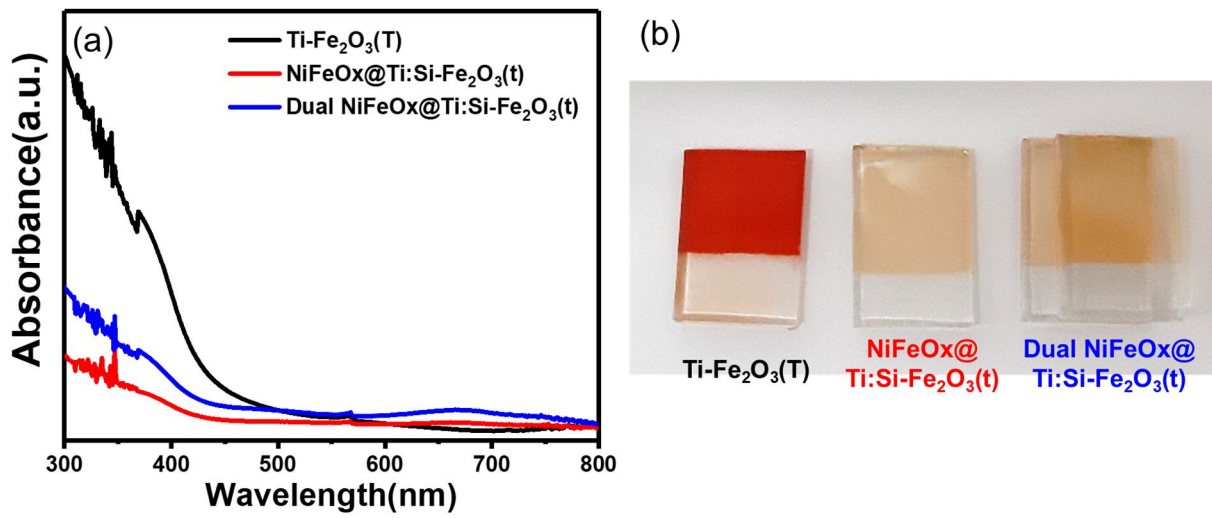


Figure 2-23. (a) UV-Vis absorption spectra and (b) digital images of Ti-Fe₂O₃(T), single and dual NiFeO_x@Ti:Si-Fe₂O₃(t).

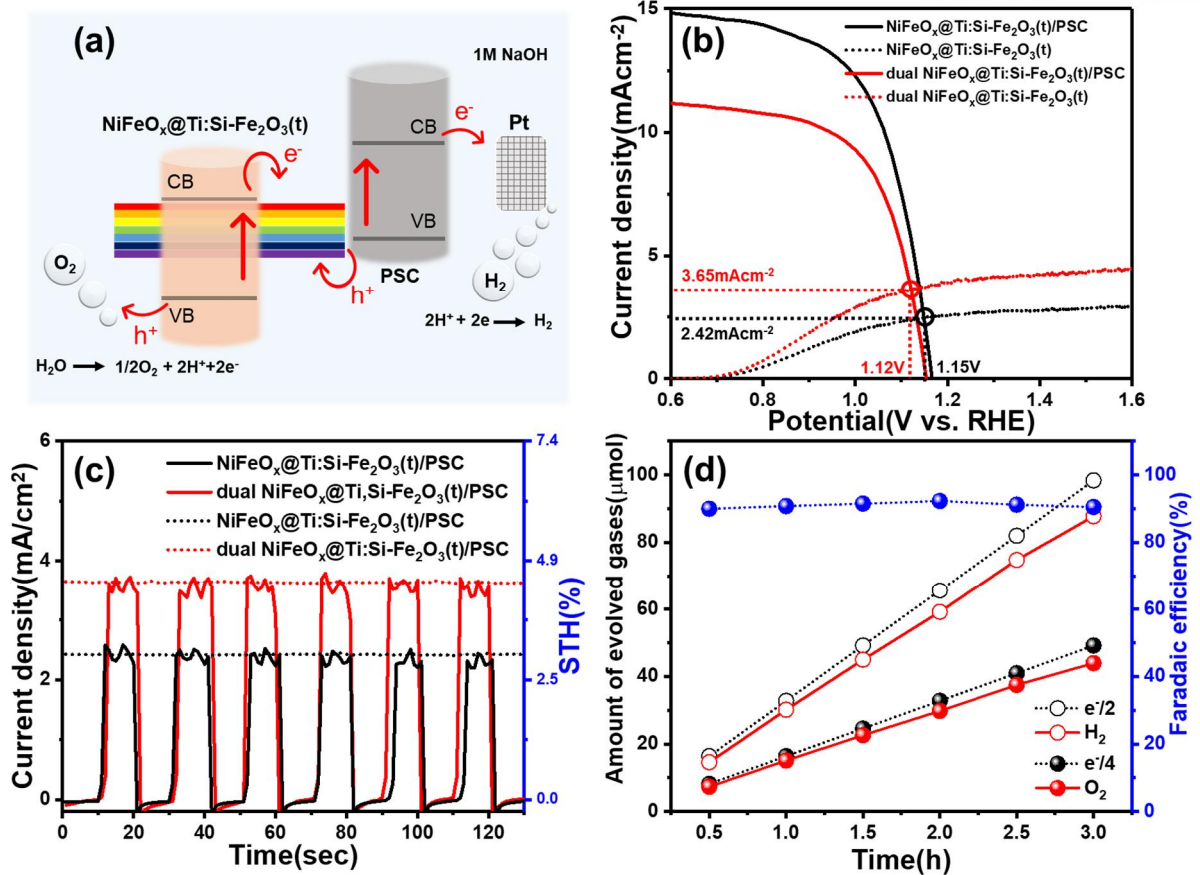


Figure 2-24. Dual $\text{NiFeO}_x@Ti:Si-Fe_2O_3(t)/PSC$ tandem cell. (a) Scheme for the tandem cell configuration, (b) J-V curves of PSC and single and dual $\text{NiFeO}_x@Ti:Si-Fe_2O_3(t)$ together under light illumination, (c) J-t measurements curves and STH conversion efficiencies of the tandem cells (dotted line: 2-electrode system; solid line: 3-electrode system at 0 V_{RHE}). (d) Faradaic efficiency and the amount of H_2 and O_2 gases for 3 h of assembled dual $\text{NiFeO}_x@Ti:Si-Fe_2O_3(t)$.

Photoanode	Photocurrent density (at 1.23V _{RHE})	Thickness	Fabrication methods	
p-i-n-Fe ₂ O ₃ heterojunction	0.5mAcm ⁻²	~30nm	Pulsed Laser Deposition (PLD)	
Fe ₂ O ₃	0.01mAcm ⁻²	~20nm	Atomic layer deposition(ALD)	
Fe ₂ O ₃ /SiO _x (under layer)	0.42mAcm ⁻²	~20nm	Spray Pyrolysis	
Fe ₂ O ₃ /TiO ₂ (under layer)	0.35mAcm ⁻²	~100nm	Spray Pyrolysis	
Ga ₂ O ₃ -Fe ₂ O ₃ -Nb ₂ O ₃ (under, overlayer)	0.5mAcm ⁻²	~30nm	Ultrasonic Spray Pyrolysis (USP)	
NiFeO_x@Ti:Si- Fe₂O₃(t)	2.6mAcm⁻²	~70nm	Hydrothermal	This work

Table 2-1. PEC performance comparison table of thin film hematite photoanodes under 100 nm.

Photoanode	R _s (Ω)	R _{trap} (Ω)	R _{ct} (Ω)
Ti-Fe ₂ O ₃ (t)	41.62	461.6	634
Ti:Si-Fe ₂ O ₃ (t)	57.59	294.3	455.5
NiFeO _x @Ti:Si-Fe ₂ O ₃ (t)	19.05	159.1	220.2

Table 2-2. EIS values of Ti-Fe₂O₃(T), Ti-Fe₂O₃(t), Ti:Si-Fe₂O₃(t) and NiFeO_x@Ti:Si-Fe₂O₃(t).

Photoanode	Photocurrent density (at 1.23V _{RHE})	In tandem with	Tandem operating photocurrent density (J _{op})	
Co-Pi/Mn-Fe ₂ O ₃	3.5mA cm ⁻²	PSC	1.93mAcm ⁻²	
Co-Pi/Sn-Fe ₂ O ₃	3.1mA cm ⁻²	PSC	2.8mAcm ⁻²	
FeNiOx/Al ₂ O ₃ /Si-Fe ₂ O ₃	2.8mA cm ⁻²	PSC	1.54mAcm ⁻²	
NiFeO_x@ Ti:Si-Fe₂O₃(t)	2.6mAcm⁻²	PSC	2.08mAcm⁻²	This work
dual NiFeO_x@ Ti:Si-Fe₂O₃(t)	4.0mAcm⁻²	PSC	3.65mAcm⁻²	This work

Table 2-3. Tandem cell performance comparison table of hematite/PSC tandem cells.

2.4 Conclusion

In summary, we found that the low PEC activities of thin film hematite ($\text{Ti-Fe}_2\text{O}_3(\text{t})$) are mainly due to the excess Sn content in the surface region, which was diffused from the FTO substrate. We used non-metallic Si doping to reduce the excess Sn content and the PEC activities of $\text{Ti-Fe}_2\text{O}_3(\text{t})$ were further improved by decorating an efficient OER co-catalyst of NiFeO_x . As a result, $\text{NiFeO}_x@\text{Ti:Si-Fe}_2\text{O}_3(\text{t})$ showed highly enhanced surface and bulk charge separation efficiencies and a photocurrent density of 2.6 mA cm^{-2} at $1.23 \text{ V}_{\text{RHE}}$.

For better hematite/PSC tandem cell performance, we assembled the dual thin film hematite photoanodes (dual $\text{NiFeO}_x@\text{Ti:Si-Fe}_2\text{O}_3(\text{t})$). Dual $\text{NiFeO}_x@\text{Ti:Si-Fe}_2\text{O}_3(\text{t})$ showed a maximum photocurrent density of 4.0 mA cm^{-2} at $1.23 \text{ V}_{\text{RHE}}$ and we achieved an outstanding tandem PEC performance with an unbiased 4.49% STH conversion efficiency, which is the highest value attained in the hematite/PSC tandem cell system. In this study, we have concluded that highly transparent thin film hematite with enhanced PEC performance is crucial for achieving efficient hematite/PSC tandem cell performance.

2.5 References

1. Grave, D. A.; Yatom, N.; Ellis, D. S.; Toroker, M. C.; Rothschild, A., The “rust” challenge: On the correlations between electronic structure, excited state dynamics, and photoelectrochemical performance of hematite photoanodes for solar water splitting. *Advanced Materials* **2018**, *30* (41), 1706577.
2. Tsyganok, A.; Klotz, D.; Malviya, K. D.; Rothschild, A.; Grave, D. A., Different Roles of Fe_{1-x}Ni_xOOH Cocatalyst on Hematite (α -Fe₂O₃) Photoanodes with Different Dopants. *ACS Catalysis* **2018**, *8* (4), 2754-2759.
3. Iandolo, B.; Hellman, A., The role of surface states in the oxygen evolution reaction on hematite. *Angewandte Chemie International Edition* **2014**, *53* (49), 13404-13408.
4. Zhang, Y.; Zhang, H.; Ji, H.; Ma, W.; Chen, C.; Zhao, J., Pivotal role and regulation of proton transfer in water oxidation on hematite photoanodes. *Journal of the American Chemical Society* **2016**, *138* (8), 2705-2711.
5. Liu, R.; Zheng, Z.; Spurgeon, J.; Yang, X., Enhanced photoelectrochemical water-splitting performance of semiconductors by surface passivation layers. *Energy & Environmental Science* **2014**, *7* (8), 2504-2517.
6. Du, C.; Yang, X.; Mayer, M. T.; Hoyt, H.; Xie, J.; McMahon, G.; Bischoff, G.; Wang, D., Hematite-based water splitting with low turn-on voltages. *Angewandte Chemie International Edition* **2013**, *52* (48), 12692-12695.
7. Yoon, K.-Y.; Ahn, H.-J.; Kwak, M.-J.; Kim, S.-I.; Park, J.; Jang, J.-H., A selectively decorated Ti-FeOOH co-catalyst for a highly efficient porous hematite-based water splitting system. *Journal of Materials Chemistry A* **2016**, *4* (48), 18730-18736.
8. Sabba, D.; Kumar, M. H.; Wong, L. H.; Barber, J.; Grätzel, M.; Mathews, N., Perovskite–hematite tandem cells for efficient overall solar driven water splitting. *Nano letters* **2015**, *15* (6), 3833-3839.
9. John, R. A.; Boix, P. P.; Yi, C.; Shi, C.; Scott, M.; Veldhuis, S. A.; Minor, A. M.; Zakeeruddin, S. M.; Wong, L. H.; Grätzel, M., Atomically Altered Hematite for Highly Efficient Perovskite Tandem Water-Splitting Devices. *ChemSusChem* **2017**, *10* (11), 2449-2456.
10. Morales-Guio, C. G.; Mayer, M. T.; Yella, A.; Tilley, S. D.; Grätzel, M.; Hu, X., An optically transparent iron nickel oxide catalyst for solar water splitting. *Journal of the American Chemical Society* **2015**, *137* (31), 9927-9936.
11. Seki, M.; Yamahara, H.; Tabata, H., Enhanced photocurrent in Rh-substituted α -Fe₂O₃ thin films grown by pulsed laser deposition. *Applied Physics Express* **2012**, *5* (11), 115801.

12. Kay, A.; Grave, D. A.; Ellis, D. S.; Dotan, H.; Rothschild, A., Heterogeneous doping to improve the performance of thin-film hematite photoanodes for solar water splitting. *ACS Energy Letters* **2016**, *1* (4), 827-833.
13. Lie, M.; Fjellvåg, H.; Kjekshus, A., Growth of Fe₂O₃ thin films by atomic layer deposition. *Thin Solid Films* **2005**, *488* (1-2), 74-81.
14. Martinson, A. B.; DeVries, M. J.; Libera, J. A.; Christensen, S. T.; Hupp, J. T.; Pellin, M. J.; Elam, J. W., Atomic layer deposition of Fe₂O₃ using ferrocene and ozone. *The Journal of Physical Chemistry C* **2011**, *115* (10), 4333-4339.
15. Avila, J. R.; Kim, D. W.; Rimoldi, M.; Farha, O. K.; Hupp, J. T., Fabrication of thin films of α -Fe₂O₃ via atomic layer deposition using iron bisamidinate and water under mild growth conditions. *ACS applied materials & interfaces* **2015**, *7* (30), 16138-16142.
16. Le Formal, F.; Grätzel, M.; Sivula, K., Controlling photoactivity in ultrathin hematite films for solar water-splitting. *Advanced Functional Materials* **2010**, *20* (7), 1099-1107.
17. Wang, D.; Zhang, X.-T.; Sun, P.-P.; Lu, S.; Wang, L.-L.; Wei, Y.-A.; Liu, Y.-C., Enhanced photoelectrochemical water splitting on hematite thin film with layer-by-layer deposited ultrathin TiO₂ underlayer. *International Journal of Hydrogen Energy* **2014**, *39* (28), 16212-16219.
18. Cesar, I.; Kay, A.; Gonzalez Martinez, J. A.; Grätzel, M., Translucent thin film Fe₂O₃ photoanodes for efficient water splitting by sunlight: nanostructure-directing effect of Si-doping. *Journal of the American Chemical Society* **2006**, *128* (14), 4582-4583.
19. Steier, L.; Herraiz-Cardona, I.; Gimenez, S.; Fabregat-Santiago, F.; Bisquert, J.; Tilley, S. D.; Grätzel, M., Understanding the role of underlayers and overlayers in thin film hematite photoanodes. *Advanced Functional Materials* **2014**, *24* (48), 7681-7688.
20. Kim, M.; Kim, G.-H.; Lee, T. K.; Choi, I. W.; Choi, H. W.; Jo, Y.; Yoon, Y. J.; Kim, J. W.; Lee, J.; Huh, D., Methylammonium Chloride Induces Intermediate Phase Stabilization for Efficient Perovskite Solar Cells. *Joule* **2019**.
21. Ling, Y.; Wang, G.; Wheeler, D. A.; Zhang, J. Z.; Li, Y., Sn-doped hematite nanostructures for photoelectrochemical water splitting. *Nano letters* **2011**, *11* (5), 2119-2125.
22. Tamirat, A. G.; Su, W.-N.; Dubale, A. A.; Chen, H.-M.; Hwang, B.-J., Photoelectrochemical water splitting at low applied potential using a NiOOH coated codoped (Sn, Zr) α -Fe₂O₃ photoanode. *Journal of Materials Chemistry A* **2015**, *3* (11), 5949-5961.
23. Kleiman-Shwarscstein, A.; Huda, M. N.; Walsh, A.; Yan, Y.; Stucky, G. D.; Hu, Y.-S.; Al-Jassim, M. M.; McFarland, E. W., Electrodeposited aluminum-doped α -Fe₂O₃ photoelectrodes: experiment and theory. *Chemistry of Materials* **2009**, *22* (2), 510-517.
24. Liao, P.; Toroker, M. C.; Carter, E. A., Electron transport in pure and doped hematite. *Nano Letters*

2011, *II* (4), 1775-1781.

25. Ahn, H.-J.; Yoon, K.-Y.; Kwak, M.-J.; Park, J.; Jang, J.-H., Boron doping of metal-doped hematite for reduced surface recombination in water splitting. *ACS Catalysis* **2018**, *8* (12), 11932-11939.
26. Zhang, Y.; Jiang, S.; Song, W.; Zhou, P.; Ji, H.; Ma, W.; Hao, W.; Chen, C.; Zhao, J., Nonmetal P-doped hematite photoanode with enhanced electron mobility and high water oxidation activity. *Energy & Environmental Science* **2015**, *8* (4), 1231-1236.
27. Ahn, H. J.; Yoon, K. Y.; Kwak, M. J.; Jang, J. H., A Titanium-Doped SiO_x Passivation Layer for Greatly Enhanced Performance of a Hematite-Based Photoelectrochemical System. *Angewandte Chemie International Edition* **2016**, *55* (34), 9922-9926.
28. Li, M.; Yang, Y.; Ling, Y.; Qiu, W.; Wang, F.; Liu, T.; Song, Y.; Liu, X.; Fang, P.; Tong, Y., Morphology and doping engineering of Sn-doped hematite nanowire photoanodes. *Nano letters* **2017**, *17* (4), 2490-2495.
29. Tilley, S. D.; Cornuz, M.; Sivula, K.; Grätzel, M., Light-induced water splitting with hematite: improved nanostructure and iridium oxide catalysis. *Angewandte Chemie International Edition* **2010**, *49* (36), 6405-6408.
30. Zhou, Z.; Huo, P.; Guo, L.; Prezhdo, O. V., Understanding hematite doping with group IV elements: a DFT+ U study. *The Journal of Physical Chemistry C* **2015**, *119* (47), 26303-26310.
31. Song, S.; Kim, J.; Lee, D.; Lee, J.; Min, T.; Chae, J. A.; Bae, J. S.; Lee, J.; Lee, J. S.; Park, S., The effect of Fe²⁺ state in electrical property variations of Sn-doped hematite powders. *Journal of the American Ceramic Society* **2017**, *100* (9), 3928-3934.
32. Hajibabaei, H.; Schon, A. R.; Hamann, T. W., Interface Control of Photoelectrochemical Water Oxidation Performance with Ni_{1-x}Fe_xO_y Modified Hematite Photoanodes. *Chemistry of Materials* **2017**, *29* (16), 6674-6683.
33. Xu, Z.; Wang, H.; Wen, Y.; Li, W.; Sun, C.; He, Y.; Shi, Z.; Pei, L.; Chen, Y.; Yan, S., Balancing Catalytic Activity and Interface Energetics of Electrocatalyst-Coated Photoanodes for Photoelectrochemical Water Splitting. *ACS applied materials & interfaces* **2018**, *10* (4), 3624-3633.

Chapter 3. Sn-Controlled Co-Doped Hematite for Efficient Solar-Assisted Chargeable Zn–Air Batteries

*Chapter 3 is reproduced in part with permission from J. Park, et al., *ACS Appl. Mater. Interfaces*, **2021**, 13, 46, 54906-54915.

3.1 Introduction

In chapter 3, we conducted a detailed investigation of the co-doping effect of Sn and Si on hematite based on the results from chapter 2. In order to alleviate lattice distortion caused by Sn doping, the co-doping of smaller heteroatoms such as Si¹⁻³ and Ge⁴⁻⁶ has been proposed to balance the ionic radius between Fe and Sn.^{7,8} However, in co-doped systems, the unintentionally diffused Sn can interfere with the intentional doping of heteroatoms, occupying vacant sites in the hematite lattice and making it challenging to achieve optimal doping concentrations.⁹ Furthermore, the higher overall concentration of dopants in co-doped systems introduces more hole-electron recombination centers, exacerbating the negative impact on photoelectrochemical (PEC) performance.¹⁰ Therefore, it is crucial to systematically control the unintentionally doped Sn content during the preparation of the photocatalyst to maximize PEC performance.

We present a facile method to control the Sn content diffused from the fluorine-doped tin oxide (FTO) substrate by employing a two-step annealing process. Through this method, the thermal diffusion length of Sn was limited to the bulk region, leading to a successful reduction in the Sn content (Sn/(Sn+Fe)) in hematite from 6.8% to approximately 1.9% at the surface region. The reduction of unintentionally diffused Sn on the hematite surface increased the solubility of the intentional dopant (Si) and minimized structural disorder, resulting in improved surface charge transport compared to Sn and Si co-doped hematite using a one-step annealing process.

Furthermore, the optimized hematite photoanode was utilized as an oxygen evolution reaction (OER) electrode in a zinc-air battery under light illumination. The charging potential of the battery was notably decreased to 1.45 V, which is lower than the theoretical charging potential of a zinc-air battery (1.65 V). This highlights the potential of our hematite photoanodes for efficient energy storage and extended battery operation.

3.2 Experimental section

-Fabrication of Sn-Fe₂O₃/1-/2

A previously reported method was used to synthesize Sn-Fe₂O₃/1 on the FTO substrate. Briefly, FeOOH was synthesized on FTO at 100 °C by using a 150 mM FeCl₃·6H₂O solution for 3 hours (in the case of Ti-doped FeOOH, 7 μL of TiCl₃ was added to the solution). The sample was then cleaned with DI water and dried with N₂ gas before being inserted into a tube furnace and annealed at 800 °C for 20 minutes to convert it to Sn-Fe₂O₃/1. Similarly, Sn-Fe₂O₃/2 was produced by repeating the same procedure with a shorter annealing time. After the first step was completed, the sample was cooled down to room temperature, and the annealing process was repeated.

-Fabrication of Sn:Si-Fe₂O₃/1-/2

The Ti-FeOOH surface was coated with a SiO_x overlayer using a dip-coating process with a solution of APTMS in DI water at a ratio of 5:1 (DI water: APTMS; v:v%). Subsequently, Sn:Si-Fe₂O₃/1 was synthesized by annealing the SiO_x coated Ti-FeOOH at 800 °C for 20 minutes. During high-temperature annealing, Si was doped into a hematite lattice from the SiO_x overlayer and Sn was doped into a hematite lattice from the FTO substrate. To create Sn:Si-Fe₂O₃/2, the same procedure as for Sn:Si-Fe₂O₃/1 was followed but with a shorter annealing time of 10 minutes at 800 °C. Once the first step was completed, the sample was cooled to room temperature, and the Si dip-coating and annealing steps were repeated at 800 °C for 10 minutes.

-Fabrication of Sn:M-Fe₂O₃/1-/2 (M: B, Ge, and Ti)

The fabrication of Sn:M-Fe₂O₃/1 and Sn:M-Fe₂O₃/2 (M: B, Ge, and Ti) followed the same procedure used for Sn:Si-Fe₂O₃, with the exception of the precursor solution used. Specifically, a 10 mM boric acid solution was used for B-doping, a 30 mM GeO₂ solution for Ge-doping, and a 10 mM TiCl₃ solution for Ti-doping.

-Fabrication of NiFe(OH)_x@ Sn:Si-Fe₂O₃/2

To decorate the NiFe(OH)_x co-catalyst, a solution of iron(III) 2-ethylhexanoate and nickel(II) 2-ethylhexanoate in a hexane solution (total metal complex concentration of 15% w/w) was drop-casted onto the surface using 10 μL of solution. The solution was diluted with hexane and exposed to UV light before being annealed at 100 °C for 1 hour.

- Electrochemical measurements

All photoelectrochemical (PEC) measurements were conducted in a three-electrode under front-side simulated Air Mass 1.5 Global (AM 1.5 G) illumination. The cell comprised an Ag/AgCl (KCl sat.) reference electrode and a Pt mesh counter electrode. The photoanode had an exposed area of 0.44 cm², which was achieved by using an O-ring in a homemade PEC kit and 1.0 M NaOH solution served as a pH 13.6 electrolyte. The potential vs. RHE was calculated using the Nernst equation $E_{\text{RHE}} = E_{\text{Ag/AgCl}} + 0.0591(\text{pH}) + 0.1976 \text{ V}$. The current density-voltage (J-V) curve was recorded at a scan rate of 20 mV s⁻¹. Photocurrent stability tests were performed by measuring the photocurrent under AM 1.5 G illumination at 1.23 V vs. RHE. Electrochemical impedance spectroscopy (EIS) was carried out using a potentiostat at a frequency range of 100 kHz to 0.1 Hz. The experimental EIS data were analyzed and fitted using Zview software. The incident photon to current conversion efficiency (IPCE) was measured under monochromatic light by a Xe lamp, and the intensity of the monochromatic light was measured by a luminometer.

3.3 Results and discussion

3.3.1 Sn and Si diffusion trends of Sn:Si-Fe₂O₃/1-2

The fabrication process of Sn and Si co-doped hematite (Sn:Si-Fe₂O₃/1-2) was shown in **Figure 3-1a**. Due to the similar Ti content of both samples synthesized by the *in-situ* hydrothermal reaction (**Figure 3-3**), the effect of Ti was not considered in this limited study for simplicity.

The fluorine-doped tin oxide (FTO) substrate was deformed during the high-temperature annealing process, leading to an unintentional Sn diffusion to hematite. Although Sn can improve the photoelectrochemical (PEC) activities of hematite by playing the role of an n-type dopant, the excess Sn can hinder the PEC activities by trapping holes and disrupting crystallinity.^{11, 12} Moreover, the unintentional diffusion of Sn can interfere with the active doping of intentional dopants by occupying the vacancy sites in the hematite lattice.

In this study, we employed a consecutive two-step annealing process at 800 °C for 10 minutes to control the diffusion of unintentional Sn, especially at the surface region, and the annealing conditions such as temperature, time, and step were adjusted to regulate the diffusion length of Sn (**Figures 3-4,5**). The conventional Sn and Si co-doped one-step annealed hematite is used as a reference hematite photoanode to compare the Sn control effect of the two-step annealing process.

Despite the same thermal energy of Sn and Si co-doped one-step (Sn:Si-Fe₂O₃/1) and two-step annealed hematite (Sn:Si-Fe₂O₃/2), both samples showed different Sn diffusion trends as shown in **Figure 3-1a**. At the A-1 process for fabricating Sn:Si-Fe₂O₃/1, Sn can easily diffuse from the FTO substrate to the hematite lattice, but the diffusion of Si from the surface overlayer is limited by pre-occupied Sn. In contrast, Sn:Si-Fe₂O₃/2 had the majority of Sn at the bulk region at the B-1 step, not the surface region due to the reduced Sn diffusion length. Then, during the B-2 step, the pre-occupied Sn at the bulk region can not diffuse to the surface region due to the high bonding energy of Sn-O,¹³⁻¹⁵ and Si diffusion is facilitated due to the many vacant sites at the surface region (B-2), overcoming the limitations of conventional one-step annealing process.^{16, 17}

3.3.2 Sn and Si content and morphological features of Sn:Si-Fe₂O₃/1-2

To verify our assumptions, X-ray photoelectron spectroscopy (XPS) depth profiles were performed in **Figures 3-1b,c** to determine the Sn content. In **Figure 3-1b**, the Sn/(Sn+Fe) ratio of Sn:Si-Fe₂O₃/2 sharply decreased to 1.9% from 6.8% of Sn:Si-Fe₂O₃/1 at the surface region, and the content of Sn in the bulk region was also reduced through two-step annealing. Differently, the content of Si increased

significantly, as shown in **Figure 3-1c**. The change of Si content is further proved by the time-of-flight secondary ion mass spectrometry (TOF-SIMS) data in **Figure 3-6**.

The bright region of TOF-SIMS 3d images of Sn:Si-Fe₂O₃/2 indicated Si diffusion from the SiO_x overlayer (top) to the bulk (bottom) and Sn diffusion from the FTO substrate (bottom) to the surface (top) (**Figure 3-1d**), which agrees with the results of energy dispersive X-ray spectroscopy (EDS) line-scanning data in **Figure 3-1e**.

The morphology of each sample was examined using scanning electron microscopy (SEM) and high-resolution transmission electron microscopy (HRTEM). In SEM (**Figures 3-7a,b**) and TEM images (**Figures 3-7c,d**), both Sn:Si-Fe₂O₃/1-/2 showed similar morphological features of porous structures with a uniform thickness of 500 nm (**Figure 3-8**) and a diameter of 100 nm. The porous structure in Sn:Si-Fe₂O₃/1 and Sn:Si-Fe₂O₃/2 was formed due to the random injection of gases during the high-temperature annealing process beneath the rigid thin amorphous SiO_x overlayer (**Figure 3-9**). The same d-spacing of 0.25 nm, corresponding to the hematite (110) plane¹⁸, between one-step and two-step annealed samples confirmed the similar crystallinity (**Figures 3-7c-I,d-I**), which was further confirmed by X-ray diffraction (XRD) and Raman data in **Figure 3-10**. The EDS analysis of Sn:Si-Fe₂O₃/1 and Sn:Si-Fe₂O₃/2 in **Figures 3-7c-II, d-II** revealed a uniform distribution of Si and Sn, although both samples have different densities of Sn and Si contents due to the subdivision of heat treatment. These characterization data demonstrated that the variation of the annealing condition does not affect the morphological features except for the Sn and Si contents.

Fe K-edge measurements, including X-ray absorption near edge structure (XANES) and extended X-ray absorption fine structure (EXAFS), were performed to explore the structural disorder. Both samples illustrated a pre-edge peak at 7115 eV in XANES, which was attributed to the presence of Fe³⁺ and 1s to 4p dipole-allowed transitions (**Figure 3-7e**).^{19,20} However, the slight shift at 7131-7134 eV indicated the absorption energies change (**Figure 3-11**).²¹ In EXAFS, the two peaks at 0.8-2.1 Å and 2.1-3.9 Å observed, indicating the nearest Fe-O bonds and contribution of Fe-Fe and Fe-O bonds at a longer distance, respectively (**Figure 3-7f**). It is known that when the Sn permeated in the hematite lattice caused stronger backscattering, leading to an increased EXAFS signal, and the lower intensity of EXAFS peaks for Sn:Si-Fe₂O₃/2 suggested reduced structure distortion due to the reduced content of injected Sn.⁴⁸ In XPS spectra in **Figure 3-7g**, Sn:Si-Fe₂O₃/2 exhibited a lower satellite peak of Fe²⁺ than Sn:Si-Fe₂O₃/1, confirming the low content of Sn in the hematite lattice.²² XPS spectra of O 1s, Sn 3d, and Si 2p in **Figure 3-12** showed decreased Sn content and increased Si content in Sn:Si-Fe₂O₃/2 compared to Sn:Si-Fe₂O₃/1. Based on these results, positive structure ordering of Sn:Si-Fe₂O₃/2 due to reduced Sn content was demonstrated.

3.3.3 PEC activities of Sn:Si-Fe₂O₃/1-/2

PEC activities of hematite photoanodes were tested using linear scan voltammetry (LSV) in a three-electrode system in **Figure 3-13a**. Sn:Si-Fe₂O₃/2 exhibited a 1.3-fold higher photocurrent density of 3.0 mA cm⁻² compared to the Sn:Si-Fe₂O₃/1 at 1.23 V_{RHE}. This result was attributed to improved charge transfer properties and reduced structural disorder, which were verified by various electrochemical analyses in **Figure 3-13b-d**. The Nyquist plot in **Figure 3-13b**, fitted by an equivalent circuit model, demonstrated that Sn:Si-Fe₂O₃/2 had reduced surface charge trapped holes and increased charge transfer efficiency than Sn:Si-Fe₂O₃/1. The high surface separation efficiencies of Sn:Si-Fe₂O₃/2 (80%), which were tested using a hole scavenger of 0.2 M Na₂SO₃ in a 1.0 M NaOH solution, compared to Sn:Si-Fe₂O₃/1 (60%) showed the enhanced charge transfer of Sn:Si-Fe₂O₃/2. The improved charge transfer was further supported by the transient photocurrent density curve (0.0001 points/s) at 1.23 V_{RHE}, as shown in **Figure 3-13d**. In the transient photocurrent density curve, the higher I_t/I_i value of Sn:Si-Fe₂O₃/2 (0.8) than Sn:Si-Fe₂O₃/1 (0.73) implies an improved charge transfer at the hematite surface.

In order to further investigate the electrochemical active surface area and carrier density of hematite photoanodes, the electrochemical active surface area (ECSA) and Mott-Schottky plots were performed under dark conditions in **Figures 3-13e,f**. Sn:Si-Fe₂O₃/2 exhibited enhanced ECSA values (**Figure 3-13e**), which were determined under different scan rates from 5 mV/s to 200 mV/s, compared to Sn:Si-Fe₂O₃/1. This explains a large active surface area and alternation in electronic structure. The Mott-Schottky plot in **Figure 3-13f** was used to calculate the carrier density of hematite photoanodes. The positive slope demonstrated an n-type semiconductor, and the lower slope of Sn:Si-Fe₂O₃/2 compared to Sn:Si-Fe₂O₃/1 indicated a rise in the carrier concentration from 2.51 X 10²⁰ cm⁻³ to 2.90 X 10²⁰ cm⁻³.

A NiFe(OH)_x co-catalyst was deposited photochemically on the Sn:Si-Fe₂O₃/2 and it achieved a photocurrent density of 3.57 mA cm⁻² (**Figure 3-13g**).²³ NiFe(OH)_x@Sn:Si-Fe₂O₃/2 showed excellent stability for 20 hours as shown in **Figure 3-13h**. Incident photon-to-current efficiency (IPCE) curves illustrated a high photo-response of NiFe(OH)_x@Sn:Si-Fe₂O₃/2 in the range of 300 to 400 nm and the applied bias photon-to-current conversion efficiency (ABPE) curves in **Figure 3-16** further confirmed the higher photon efficiencies of NiFe(OH)_x@Sn:Si-Fe₂O₃/2 than that of Sn:Si-Fe₂O₃/2 at lower applied bias.

3.3.4 Solar-assisted zinc-air battery assembled with hematite photoanode

Zinc-air batteries are a promising battery system that uses an aqueous electrolyte, owing to their high energy densities and better safety compared to Li-ion batteries. However, several drawbacks including

poor cyclability, low OER activities, and expensive price of the air electrodes limit the overall energy efficiencies of the zinc-air battery.

In this study, we anticipate that the high OER activities, excellent stability, and cheap price (~1% price of Ir; Alibaba) of hematite photoelectrode will significantly enhance the energy efficiency of a zinc-air battery as the charge electrode under light illumination.²⁴

Before testing the potential for hematite photoelectrodes as charge electrode of a zinc-air battery, a zinc-air battery was assembled using novel electrodes of Ir/C and Pt/C for charge and discharge electrodes, respectively as shown in **Figure 3-19a**.²⁵ In a conventional zinc-air battery, the Ir/C electrode exhibited a charging potential of 1.68 V, which is close to the theoretical value of a zinc-air battery, and the round-trip efficiency over 80% during the initial charging process due to the superior activities of the novel electrode (Ir/C and Pt/C). The zinc-air battery assembled with hematite photoelectrode can utilize solar energy to create electron-hole pairs. The generated holes and electrons travel to the hematite and Zn, respectively, causing the oxidation of H₂O to O₂ and the reduction of Zn(OH)₄²⁻ to Zn, as depicted in **Figure 3-19b**. This leads to a significant reduction in the high overpotential of the zinc-air battery by promoting the oxidation process. The zinc-air battery assembled with hematite photoelectrode showed a significantly reduced charging potential of 1.45 V, while the discharge potential remained constant (using the same Pt/C electrode), and a higher round-trip efficiency over 95% compared to that of conventional zinc-air battery without hematite photoelectrode. The reduction in charging potential was due to the photoexcitation of the hematite photoelectrode under illumination, which was lower than the theoretical cell voltage of zinc-air batteries. Furthermore, the zinc-air battery with hematite photoelectrode exhibited excellent long-term cyclability for 20 hours under light (**Figure 3-19d**) and dark conditions (**Figure 3-20**). In contrast, the conventional zinc-air batteries showed poor cyclability, mainly due to the degradation of Ir/C (**Figure 3-19c**).²⁶ The high stable cyclability was further confirmed by the voltage gap (ΔV) profiles between charge (OER)/discharge (oxygen reduction reaction; ORR) in **Figure 3-19e**. The voltage gap value of 0.07 V for the zinc-air battery with hematite photoelectrode was maintained for 20 hours, whereas the voltage gap of the conventional zinc-air battery increased dramatically from 0.31 V to 0.45 V. Based on these results, the solar-assisted zinc-air battery assembled hematite photoelectrode can be a promising solution to improve the overall energy efficiencies of zinc-air batteries.

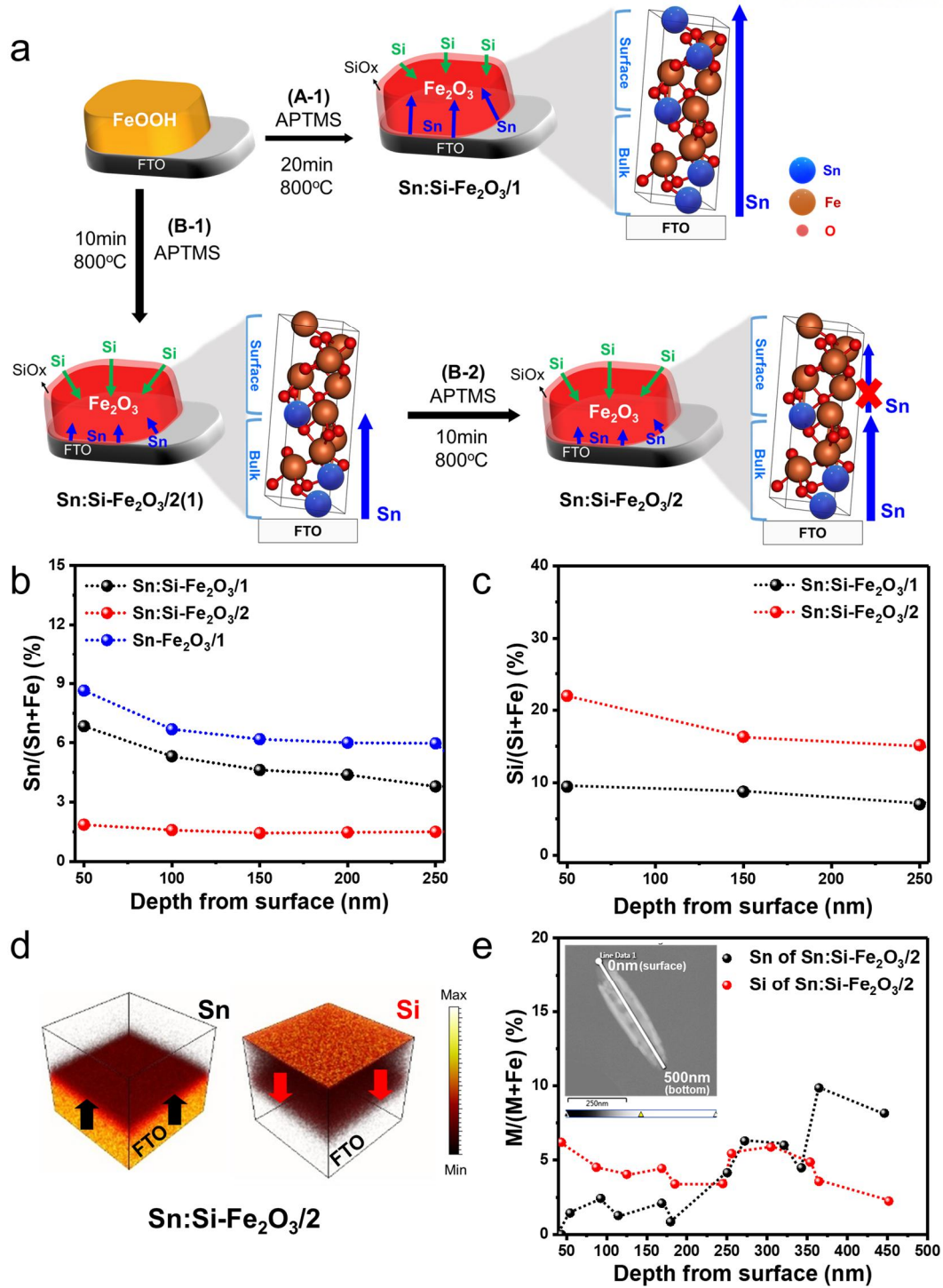


Figure 3-1. Content and diffusion trends of Sn and Si in Sn:Si-Fe₂O₃/1-2. (a) Schematic illustration of fabrication procedures and Sn and Si diffusion trends of Sn:Si-Fe₂O₃/1-2. XPS depth profiles of (b) Sn and (c) Si. (d) TOF-SIMS 3d images of Sn and Si. (e) EDS line-scanning data of Sn and Si.

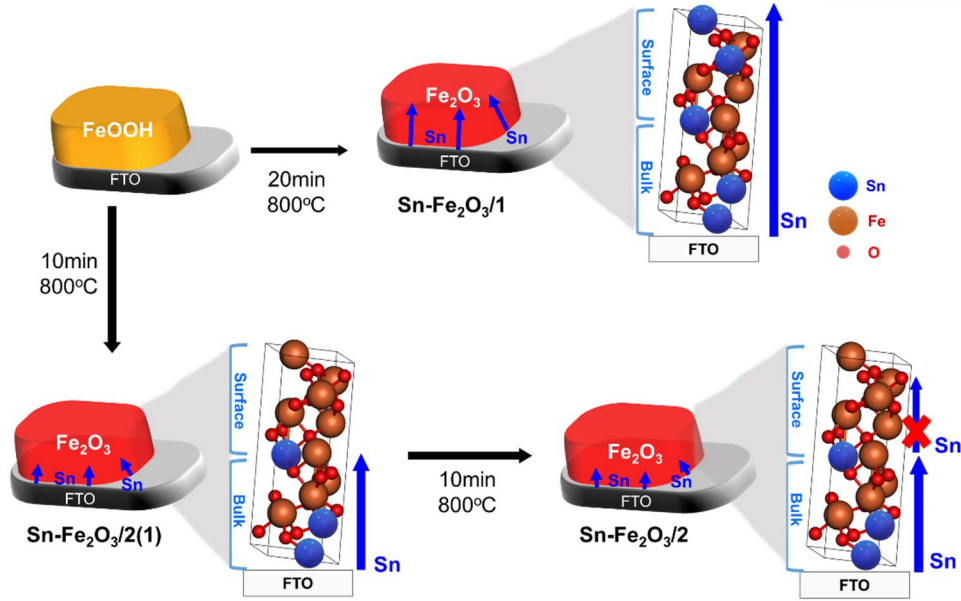


Figure 3-2. Schematic illustration of fabrication procedures of Sn-Fe₂O₃/1-/2.

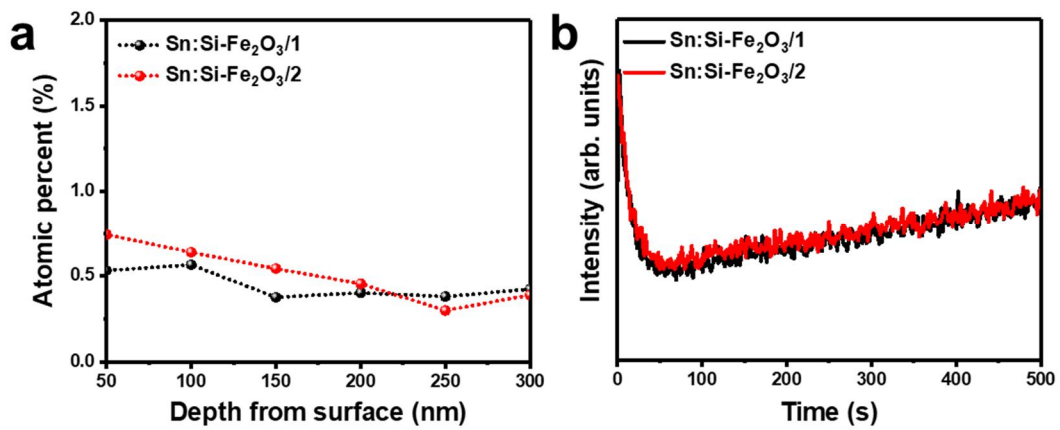


Figure 3-3. (a) XPS and (b) TOF-SIMS depth profiles of Ti in Sn:Si-Fe₂O₃/1-/2 (TOF SIMS etching rate: ~ 0.6 nm/s).

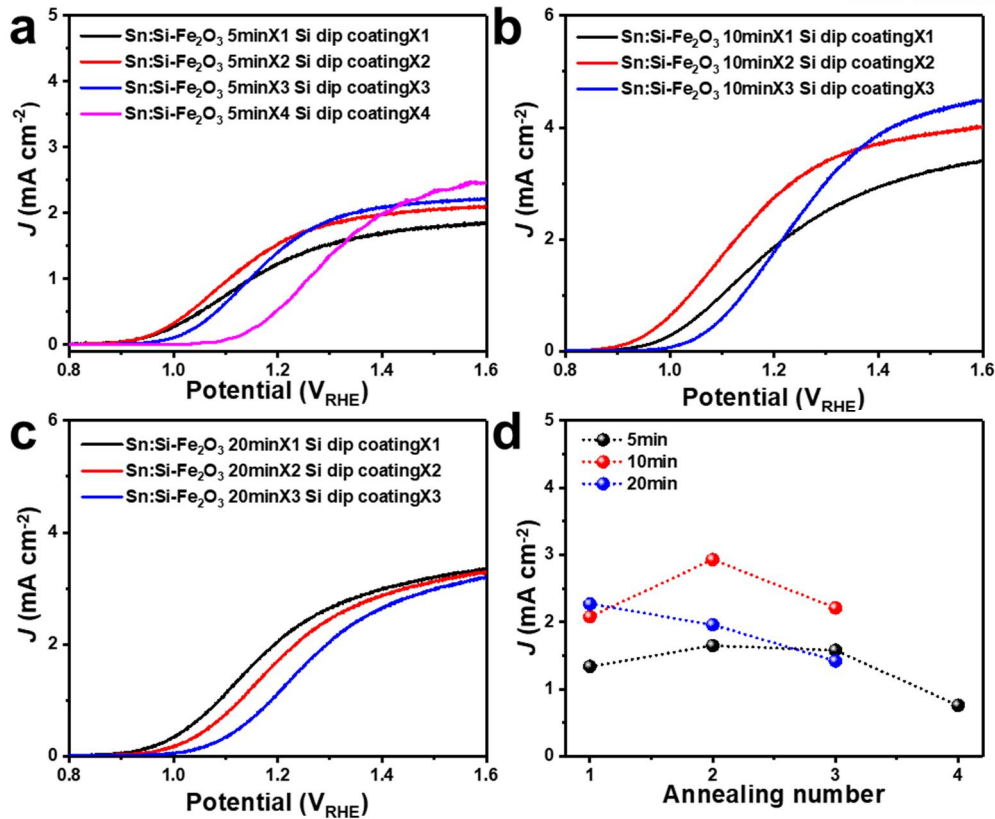


Figure 3-4. J-V curves with various annealing step and repetition number annealed (a) at 800 °C for 5 min, (b) at 800 °C for 10min, and (c) at 800 °C for 20 min of Sn:Si-Fe₂O₃. (d) Current density at 1.23 V_{RHE} according to different annealing number.

Note: We optimized Sn content in Sn:Si-Fe₂O₃ by controlling the annealing time and number at 800 °C. As shown in **Figure 3-4d**, Sn:Si-Fe₂O₃ annealed for 20 minutes show the highest photocurrent density compared to that of short time annealed samples, indicating a deficiency of dopants in the short-term annealed samples. However, Sn:Si-Fe₂O₃ annealed for 20 minutes gradually decreased after repetitions of annealing number due to an excess diffusion of Sn and Si. On the other hand, Sn:Si-Fe₂O₃ annealed for a short time (5 minutes and 10 minutes), where Sn diffusion was initially controlled, the photocurrent density gradually increased with repeated annealing number. This was due to the replacement of the Sn dopant by the more effective Si dopant. When the total annealing time exceeded 20 minutes, all the samples exhibited decreased photocurrent density and anodic shift of the onset potential, indicating an excess of dopants. Based on these findings, we selected a two-step annealing process of 10 minutes at 800 °C as the optimal condition.

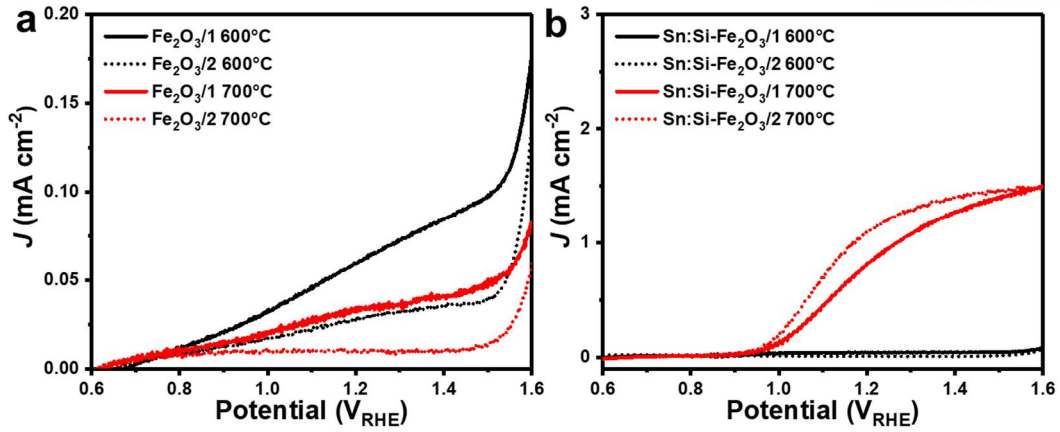


Figure 3-5. J-V curves of (a) $\text{Fe}_2\text{O}_3/1-2$ and $\text{Sn:Si-Fe}_2\text{O}_3/1-2$ annealed at 600 °C and 700 °C.

Note: Since the FTO substrate deforms over 700 °C, both Fe_2O_3 and $\text{Sn:Si-Fe}_2\text{O}_3$ annealed at 600 °C and 700 °C exhibited poor photocurrent density compared to Fe_2O_3 and $\text{Sn:Si-Fe}_2\text{O}_3$ annealed at 800 °C.

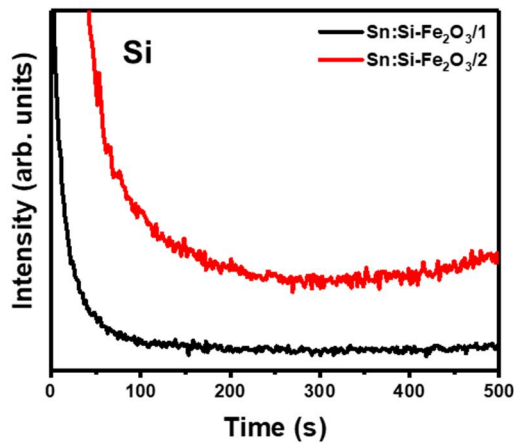


Figure 3-6. TOF-SIMS depth profiles of Si (TOF-SIMS etching rate: ~ 0.6 nm/s).

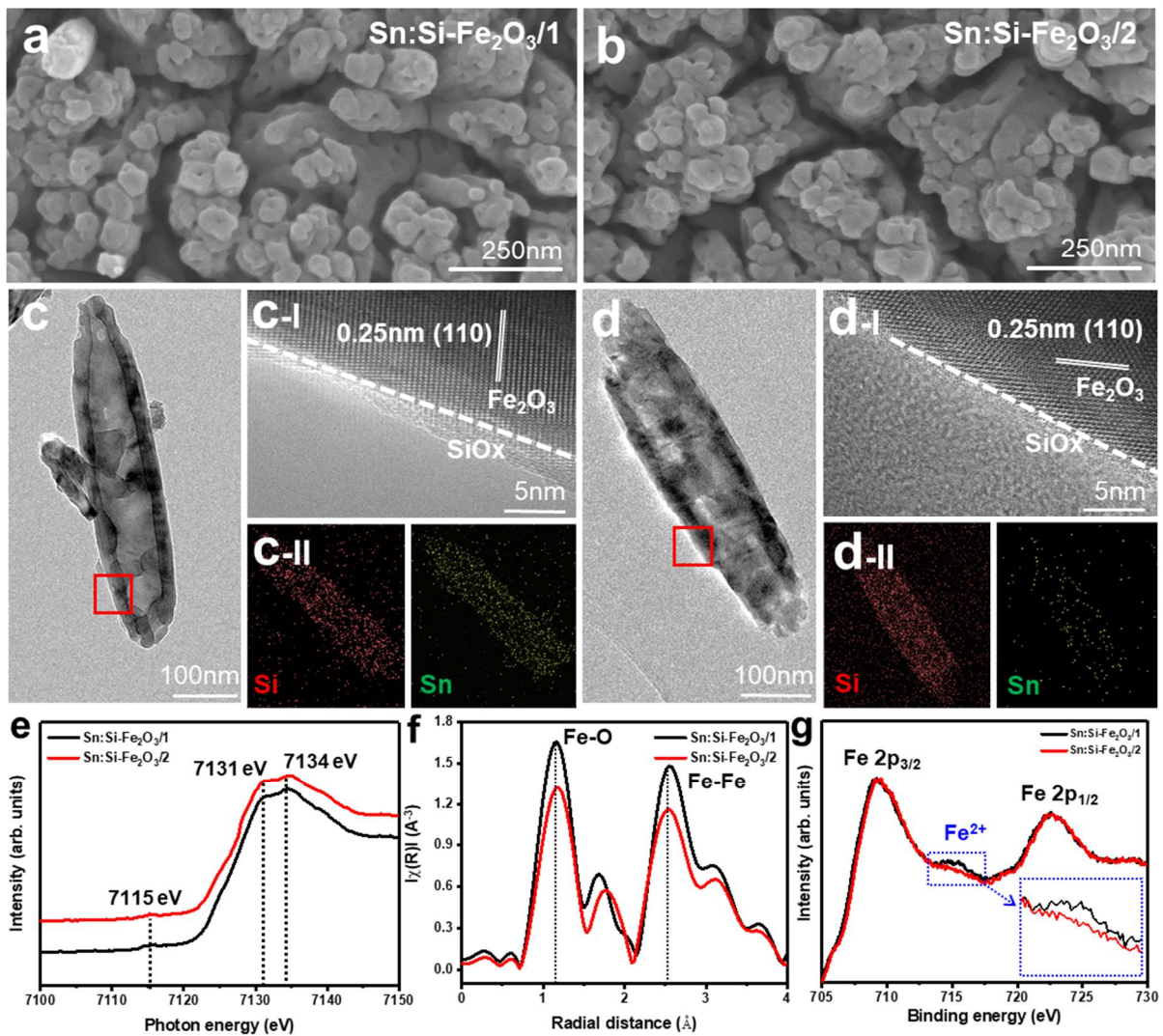


Figure 3-7. Morphological features of Sn:Si-Fe₂O₃/1-2. (a-b) SEM images. (c) HRTEM image, (c-I) close-up image of **Figure 3-7c** in the rectangular region, and (c-II) EDS mapping images of Sn:Si-Fe₂O₃/1. (d) HRTEM image, (d-I) close-up image of **Figure 3-7d** in the rectangular region, and (d-II) EDS mapping images of Sn:Si-Fe₂O₃/2. (e) Fe-K edge XANES spectra. (f) Fourier transformations of Fe K-edge EXAFS. and (g) XPS spectra of Fe 2p.

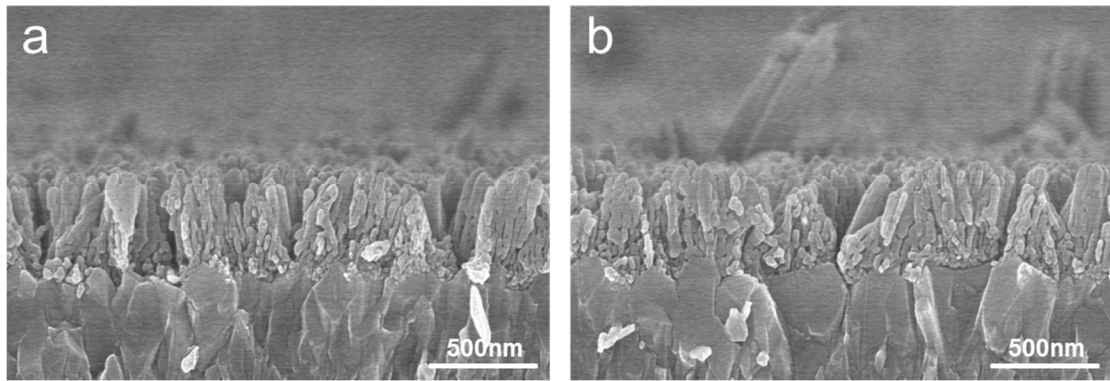


Figure 3-8. Cross-section SEM images of (a) Sn:Si-Fe₂O₃/1 and (b) Sn:Si-Fe₂O₃/2.

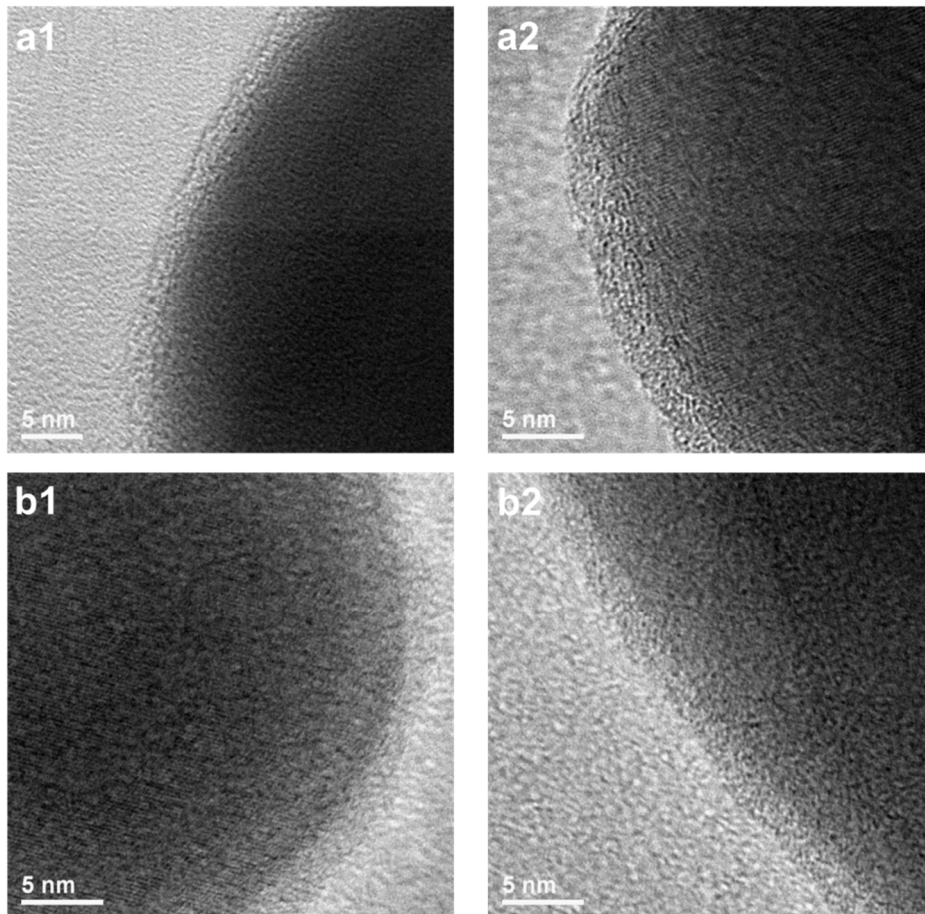


Figure 3-9. TEM images of (a1-a2) Sn:Si-Fe₂O₃/1 and (b1-b2) Sn:Si-Fe₂O₃/2.

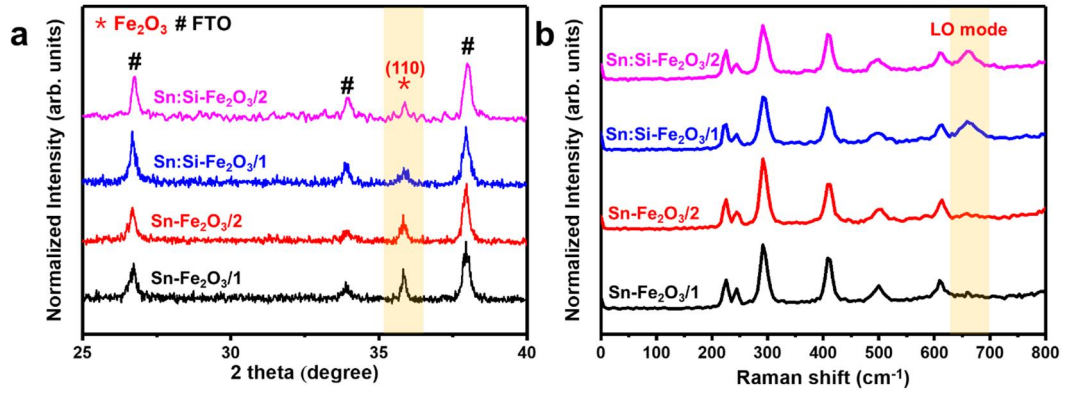


Figure 3-10. (a) XRD patterns and (b) Raman spectra of Sn-Fe₂O₃/1-2 and Sn:Si-Fe₂O₃/1-2.

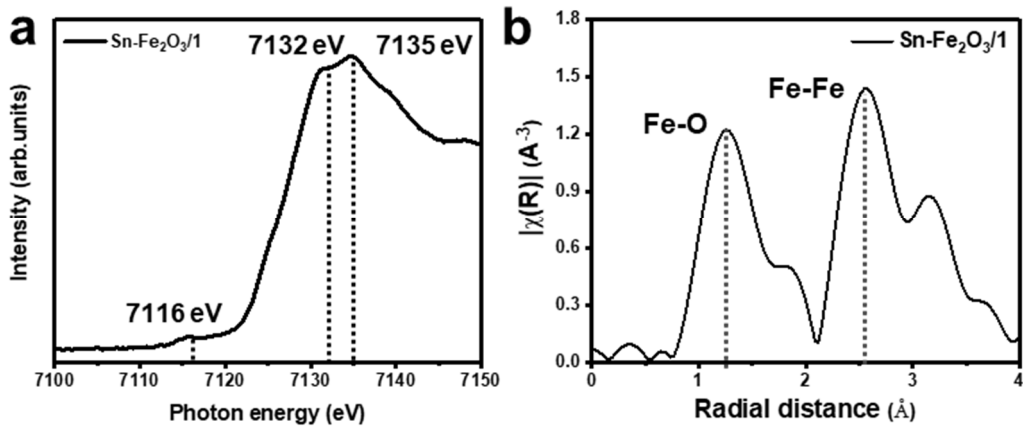


Figure 3-11. (a) Fe-K edge XANES and (b) Fourier transformations of Fe K-edge EXAFS spectra of Sn-Fe₂O₃/1.

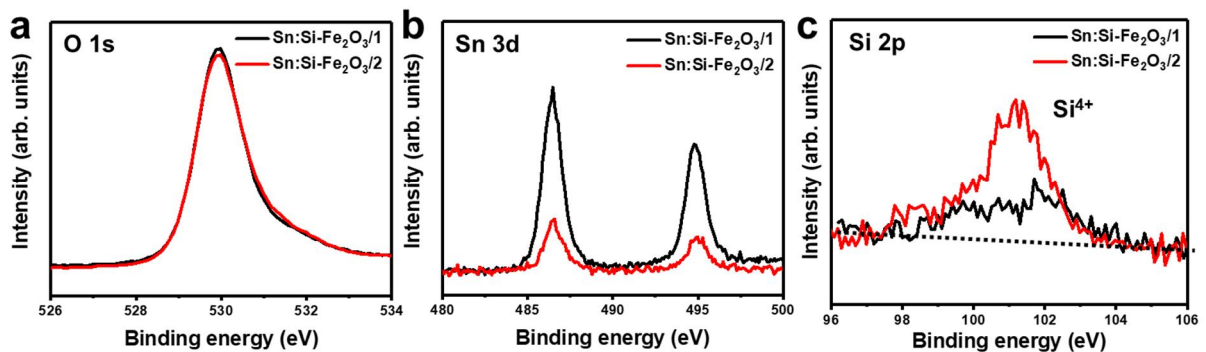


Figure 3-12. XPS (a) O 1s, (b) Sn 3d, and (c) Si 2p spectra of Sn:Si-Fe₂O₃/1-2.

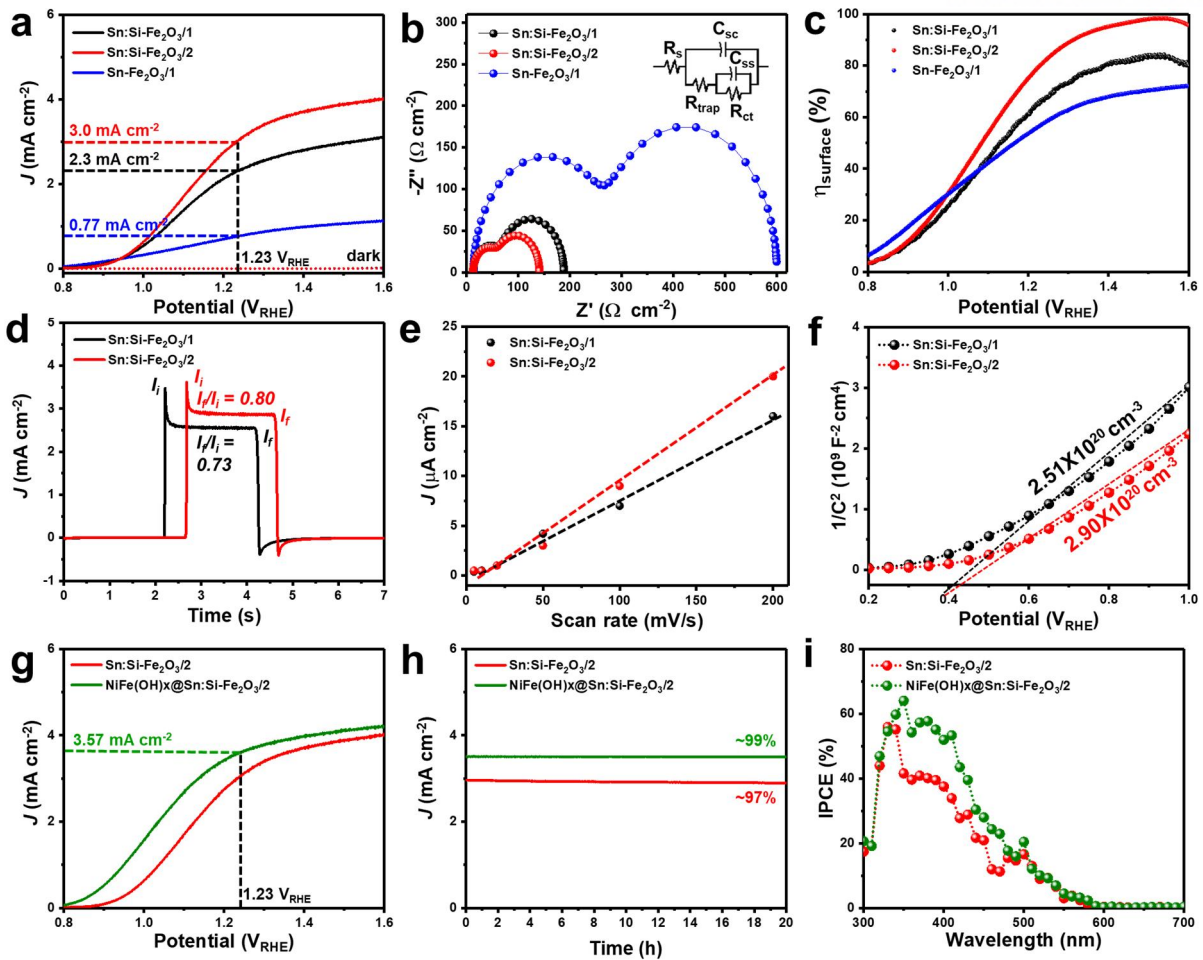


Figure 3-13. PEC activities of Sn:Si-Fe₂O₃/1-2. (a) J-V curves. (b) EIS spectra at 1.23 V_{RHE}. (c) Surface charge separation efficiencies (η_{surface}). (d) Transient photocurrent density at 1.23 V_{RHE}. (e) ECSA values with different scan rates. (f) Mott-Schottky plots under dark condition. (g) J-V curves, (h) J-t measurements during 20 hours at 1.23 V_{RHE}, and (i) IPCE spectra of Sn:Si-Fe₂O₃/2 and NiFe(OH)_x@Sn:Si-Fe₂O₃/2.

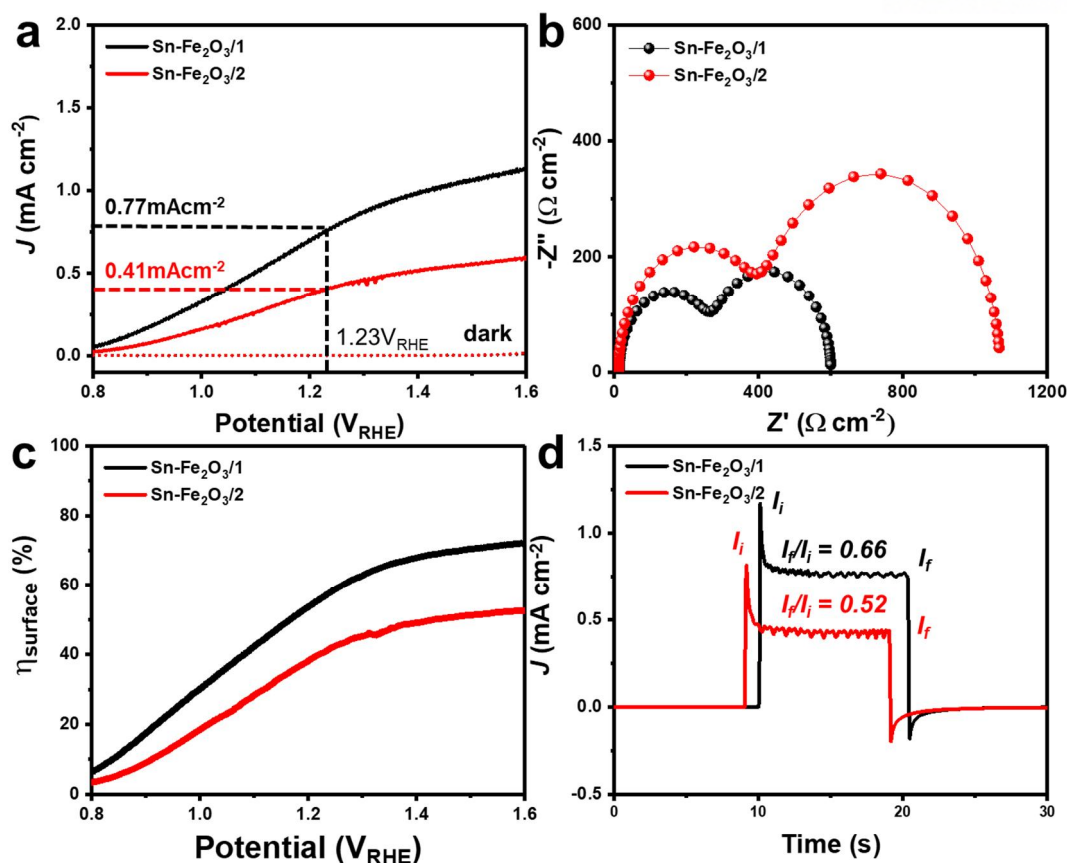
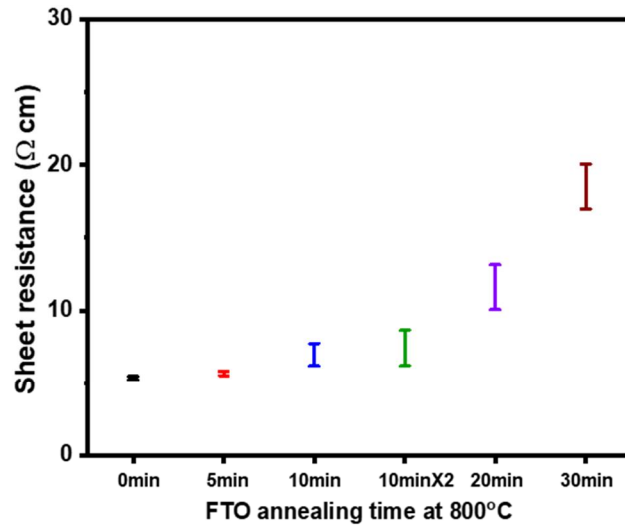


Figure 3-14. PEC activities of Sn-Fe₂O₃/1-2. (a) J-V curves. (b) EIS spectra at 1.23 V_{RHE}. (c) Surface charge separation efficiencies (η_{surface}). (d) Transient photocurrent density at 1.23 V_{RHE}.

Note: In contrast to Sn:Si-Fe₂O₃, the behavior of Sn-Fe₂O₃, where only Sn serves as an electron donor, exhibited an opposite trend. Sn-Fe₂O₃/2 demonstrated a decreased photocurrent density of 0.41 mA cm⁻² compared to that of Sn-Fe₂O₃/1 (0.77 mA cm⁻²) at 1.23 V_{RHE} due to the large surface resistance, low surface separation efficiencies, and large surface recombination rate (**Figures 3-14b-d**) It indicated that the reduced Sn concentration in Sn-Fe₂O₃ led to decreased PEC activities, emphasizing the critical role of Sn for achieving high PEC activities in the single Sn doping system.



#	0	800°C 5min	800°C 10min	800°C 10minX2	800°C 20min	800°C 30min
Min.	5.2	5.5	6.7	7	11.1	18
Max.	5.5	5.8	7.2	7.8	12.1	19
Ave.	5.4	5.7	7.0	7.4	11.6	18.5

Figure 3-15. Four-point probe sheet resistance of FTO with different annealing conditions at 800 °C.

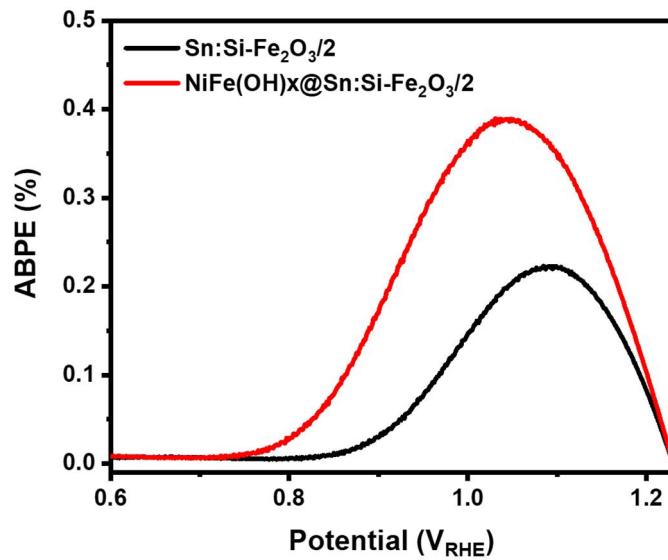


Figure 3-16. ABPE curve of Sn:Si-Fe₂O₃/2 and NiFe(OH)_x@Sn:Si-Fe₂O₃/2.

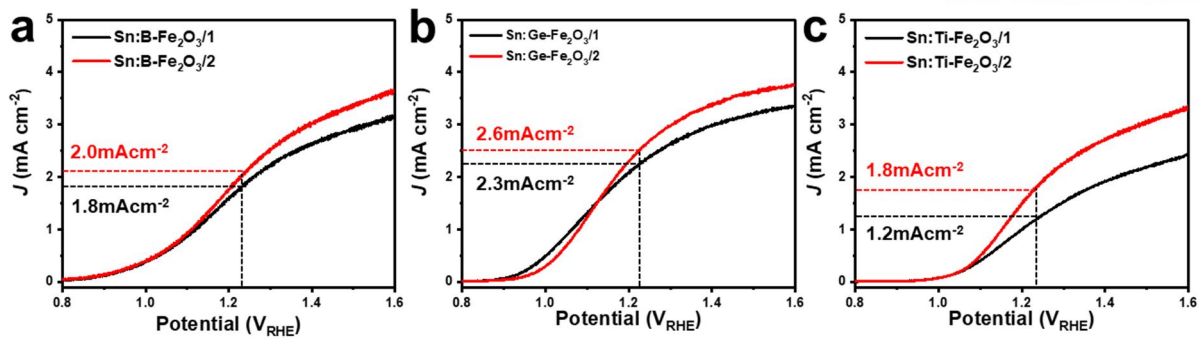


Figure 3-17. J-V curves of (a) Sn:B-Fe₂O₃/1-/2, (b) Sn:Ge-Fe₂O₃/1-/2, and (c) Sn:Ti-Fe₂O₃/1-/2.

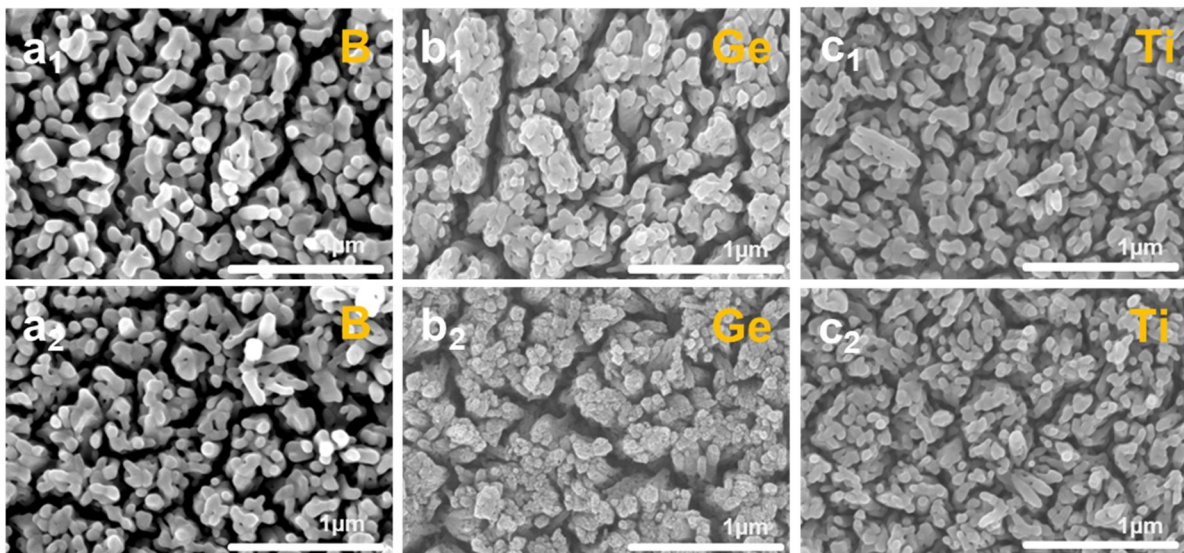


Figure 3-18. SEM images of (a₁-a₂) Sn:B-Fe₂O₃/1-/2, (b₁-b₂) Sn:Ge-Fe₂O₃/1-/2, and (c₁-c₂) Sn:Ti-Fe₂O₃/1-/2.

Note: Our strategy is not limited to Si doping but can also be applied to other dopants. As shown in **Figures 3-17a-c**, B-, Ge-, and Ti-doped hematite photoanodes with a two-step annealing process exhibited higher PEC activities compared to the samples annealed with one-step. Since there is no morphological difference between one-step and two-step annealed samples (**Figure 3-18**), the high PEC activities ascribe to reduced Sn content.

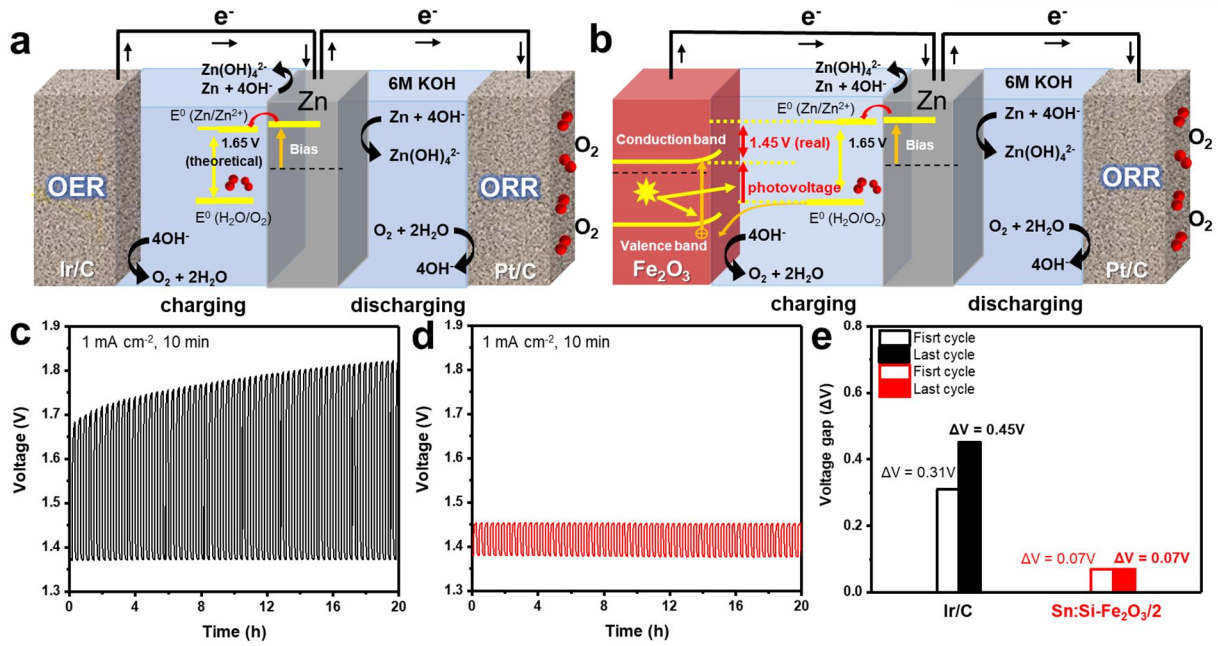


Figure 3-19. Solar-assisted zinc-air battery assembled with hematite photoelectrode. Schematic illustration of (a) zinc-air battery assembled by Ir/C and Pt/C, and (b) solar-assisted zinc-air battery assembled by Fe₂O₃ and Pt/C. Cycling performance of the (c) zinc-air battery with Ir/C and (d) solar-assisted zinc-air battery with Sn:Si-Fe₂O₃/2 under illumination for 20 hours. (e) Voltage gap of the zinc-air batteries with Ir/C and with Sn:Si-Fe₂O₃/2 at the first and last cycles for 20 hours (Electrolyte: 6 M KOH).

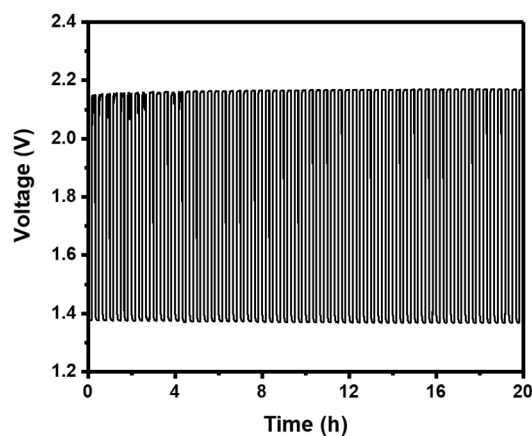


Figure 3-20. Cycling performance of zinc-air battery with Sn:Si-Fe₂O₃/2 in the dark condition (Electrolyte: 6 M KOH).

3.4 Conclusion

In conclusion, we have developed a two-step annealing method to control the Sn content of hematite photoanodes diffused from the FTO substrate. This method effectively regulates the unintentional diffusion of Sn and reduces the Sn/(Sn+Fe) ratio from 6.8% to 1.9%, which is essential for reducing surface charge recombination in heteroatom-doped systems such as B, Ge, and Ti. The reduction of Sn content resulted in less structural disorder and fast charge transport. By decorating the NiFe(OH)_x co-catalyst, we achieved a maximum photocurrent density of 3.57 mA cm⁻² at 1.23 V_{RHE}.

The optimized co-doped hematite photoelectrode can also serve as a potential substitute electrode for expensive Ir/C, which significantly reduces the fabrication cost and improve the overall energy efficiencies of zinc-air batteries.

3.5 References

1. Park, J.; Yoon, K.-Y.; Kim, T.; Jang, H.; Kwak, M.-J.; Kim, J. Y.; Jang, J.-H. *J. N. E.*, A highly transparent thin film hematite with multi-element dopability for an efficient unassisted water splitting system. **2020**, *76*, 105089.
2. Cesar, I.; Sivula, K.; Kay, A.; Zboril, R.; Grätzel, M. *J. T. J. o. P. C. C.*, Influence of feature size, film thickness, and silicon doping on the performance of nanostructured hematite photoanodes for solar water splitting. **2009**, *113* (2), 772-782.
3. Yoon, K.-Y.; Ahn, H.-J.; Kwak, M.-J.; Kim, S.-I.; Park, J.; Jang, J.-H. *J. J. o. M. C. A.*, A selectively decorated Ti-FeOOH co-catalyst for a highly efficient porous hematite-based water splitting system. **2016**, *4* (48), 18730-18736.
4. Liu, J.; Liang, C.; Xu, G.; Tian, Z.; Shao, G.; Zhang, L. *J. N. E.*, Ge-doped hematite nanosheets with tunable doping level, structure and improved photoelectrochemical performance. **2013**, *2* (3), 328-336.
5. Zhao, L.; Xiao, J.; Huang, H.; Huang, Q.; Zhao, Y.; Li, Y. *J. I. J. o. H. E.*, Enhanced efficiency of hematite photoanode for water splitting with the doping of Ge. **2018**, *43* (28), 12646-12652.
6. Yoon, K.-Y.; Park, J.; Jung, M.; Ji, S.-G.; Lee, H.; Seo, J. H.; Kwak, M.-J.; Il Seok, S.; Lee, J. H.; Jang, J.-H. *J. N. C.*, NiFeO_x decorated Ge-hematite/perovskite for an efficient water splitting system. **2021**, *12* (1), 4309.
7. Annamalai, A.; Lee, H. H.; Choi, S. H.; Lee, S. Y.; Gracia-Espino, E.; Subramanian, A.; Park, J.; Kong, K.-j.; Jang, J. S. *J. S. r.*, Sn/Be sequentially co-doped hematite photoanodes for enhanced photoelectrochemical water oxidation: effect of Be²⁺ as co-dopant. **2016**, *6* (1), 23183.
8. Cai, J.; Chen, H.; Liu, C.; Yin, S.; Li, H.; Xu, L.; Liu, H.; Xie, Q. *J. D. T.*, Engineered Sn- and Mg-doped hematite photoanodes for efficient photoelectrochemical water oxidation. **2020**, *49* (32), 11282-11289.
9. Ling, Y.; Wang, G.; Wheeler, D. A.; Zhang, J. Z.; Li, Y. *J. N. l.*, Sn-doped hematite nanostructures for photoelectrochemical water splitting. **2011**, *11* (5), 2119-2125.
10. Tamirat, A. G.; Rick, J.; Dubale, A. A.; Su, W.-N.; Hwang, B.-J. *J. N. h.*, Using hematite for photoelectrochemical water splitting: a review of current progress and challenges. **2016**, *1* (4), 243-267.
11. Zhang, H.; Park, J. H.; Byun, W. J.; Song, M. H.; Lee, J. S. *J. C. s.*, Activating the surface and bulk of hematite photoanodes to improve solar water splitting. **2019**, *10* (44), 10436-10444.
12. Li, C.; Luo, Z.; Wang, T.; Gong, J. *J. A. M.*, Surface, bulk, and interface: rational design of hematite architecture toward efficient photo-electrochemical water splitting. **2018**, *30* (30), 1707502.
13. Shinde, P. S.; Annamalai, A.; Kim, J. H.; Choi, S. H.; Lee, J. S.; Jang, J. S. *J. S. E. M.*;

Cells, S., Exploiting the dynamic Sn diffusion from deformation of FTO to boost the photocurrent performance of hematite photoanodes. **2015**, *141*, 71-79.

14. Ma, H.; Mahadik, M. A.; Park, J. W.; Kumar, M.; Chung, H. S.; Chae, W. S.; Kong, G. W.; Lee, H. H.; Choi, S. H.; Jang, J. S. J. N., Highly self-diffused Sn doping in α -Fe₂O₃ nanorod photoanodes initiated from β -FeOOH nanorod/FTO by hydrogen treatment for solar water oxidation. **2018**, *10* (47), 22560-22571.

15. Shinde, P. S.; Annamalai, A.; Kim, J. H.; Choi, S. H.; Lee, J. S.; Jang, J. S. J. D. i. b., Photoelectrochemical, impedance and optical data for self Sn-diffusion doped Fe₂O₃ photoanodes fabricated at high temperature by one and two-step annealing methods. **2015**, *5*, 796-804.

16. Ahn, H. J.; Yoon, K. Y.; Kwak, M. J.; Jang, J. H. J. A. C., A titanium-doped SiO_x passivation layer for greatly enhanced performance of a hematite-based photoelectrochemical system. **2016**, *128* (34), 10076-10080.

17. Chen, D.; Liu, Z. J. C., Dual-axial gradient doping (Zr and Sn) on hematite for promoting charge separation in photoelectrochemical water splitting. **2018**, *11* (19), 3438-3448.

18. Zhang, Z.; Karimata, I.; Nagashima, H.; Muto, S.; Ohara, K.; Sugimoto, K.; Tachikawa, T. J. N. c., Interfacial oxygen vacancies yielding long-lived holes in hematite mesocrystal-based photoanodes. **2019**, *10* (1), 4832.

19. Quiterio, P.; Apolinario, A.; Navas, D.; Magalhaes, S.; Alves, E.; Mendes, A.; Sousa, C. T.; Araujo, J. P. J. T. J. o. P. C. C., Photoelectrochemical water splitting: Thermal annealing challenges on hematite nanowires. **2020**, *124* (24), 12897-12911.

20. Tamirat, A. G.; Su, W.-N.; Dubale, A. A.; Pan, C.-J.; Chen, H.-M.; Ayele, D. W.; Lee, J.-F.; Hwang, B.-J. J. J. o. P. S., Efficient photoelectrochemical water splitting using three dimensional urchin-like hematite nanostructure modified with reduced graphene oxide. **2015**, *287*, 119-128.

21. Husain, H.; Hariyanto, B.; Sulthonul, M.; Thamkeng, P.; Pratapa, S. In *Local structure examination of mineral-derived Fe₂O₃ powder by Fe K-edge EXAFS and XANES*, IOP Conference Series: Materials Science and Engineering, IOP Publishing: 2018; p 012027.

22. Ahn, H.-J.; Yoon, K.-Y.; Kwak, M.-J.; Park, J.; Jang, J.-H. J. A. C., Boron doping of metal-doped hematite for reduced surface recombination in water splitting. **2018**, *8* (12), 11932-11939.

23. Zhang, J.; Huang, Y.; Lu, X.; Yang, J.; Tong, Y. J. A. S. C.; Engineering, Enhanced BiVO₄ photoanode photoelectrochemical performance via borate treatment and a NiFeOx cocatalyst. **2021**, *9* (24), 8306-8314.

24. Liu, X.; Yuan, Y.; Liu, J.; Liu, B.; Chen, X.; Ding, J.; Han, X.; Deng, Y.; Zhong, C.; Hu, W. J. N. c., Utilizing solar energy to improve the oxygen evolution reaction kinetics in zinc-air battery. **2019**, *10* (1), 4767.

25. Zhang, J.; Zhou, Q.; Tang, Y.; Zhang, L.; Li, Y. J. C. S., Zinc–air batteries: are they ready for prime time? **2019**, *10* (39), 8924-8929.
26. Li, L.; Wang, P.; Shao, Q.; Huang, X. J. A. M., Recent progress in advanced electrocatalyst design for acidic oxygen evolution reaction. **2021**, *33* (50), 2004243.

Chapter 4. Boosting Charge Transfer Efficiency by Nanofragment MXene for Efficient Photoelectrochemical Water Splitting of NiFe(OH)_x Co-Catalyzed Hematite

*Chapter 4 is reproduced in part with permission from J. Park, et al., *ACS Appl. Mater. Interfaces*, **2023**, 15, 7, 9341-9349.

4.1 Introduction

The practical solar-to-hydrogen (STH) conversion efficiency of hematite ($\alpha\text{-Fe}_2\text{O}_3$) is lower than the theoretical efficiency due to challenges such as high surface recombination rate, poor electrical conductivity, and short hole diffusion length. Various strategies have been explored to overcome these issues, including doping, heterojunctions, and the use of oxygen evolution co-catalysts (OECs).^{1, 2} Among these approaches, OECs have gained significant attention for their ability to enhance photoelectrochemical (PEC) performance by decreasing the water oxidation overpotential and improving oxygen evolution reaction (OER) kinetics.^{3, 4} While OECs facilitate surface charge transfer from hematite to the electrolyte, the significant bulk recombination in hematite can hinder efficient hole extraction, limiting overall PEC performance. To fully exploit the benefits of OECs in PEC water splitting, it is necessary to further enhance hole extraction in hematite by optimizing the band bending at the interface of the hematite photoanode and the electrolyte. Previous studies have proposed the formation of a p-n junction between CoAl layered double hydroxides and hematite to extract the hole⁵ or regrowth treatment onto F-doped hematite for optimal band bending at the photoanode/electrolyte interface.⁶

In recent years, two-dimensional (2D) materials such as black phosphorous (BP), graphitic carbon nitrides (GCNs), and layered double hydroxides have been extensively explored for electrochemical applications due to their excellent charge transport properties and large active sites.^{7, 8} Among these materials, 2D layered MXene ($\text{Ti}_3\text{C}_2\text{T}_x$; T: functional groups) has shown great potential for efficient PEC water splitting systems due to its high electrical properties and active functional groups.^{9, 10} However, the high reactivity of MXene to TiO_2 in aqueous solutions^{11, 12} and the challenge of integrating it into nanostructured photoanodes (typically 1D or 3D)¹³ have limited its application in PEC water splitting system.

In this study, we present a method to utilize MXene with hematite for PEC water splitting by fabricating nanofragment MXene (NFMX). The NFMX, with an average particle size of 8 nm, was obtained by centrifuge-assisted method with maintaining the superior electrical properties of the 2D MXene sheets and deposited onto $\alpha\text{-Fe}_2\text{O}_3$ using a centrifuge coating method. NFMX/ Fe_2O_3 showed

improved bulk hole extraction and surface charge transfer efficiencies. By depositing NiFe(OH)_x co-catalyst overlayer on the surface $\text{NFMX/Fe}_2\text{O}_3$, it showed an improved surface charge transfer efficiency and excellent stability for 60 hours.

4.2 Experimental section

- Fabrication of nanofragment MXene (NFMX)

Ti₃AlC₂ powder was added gradually to a solution consisting of 20 mL of 9 M HCl solution containing 1g of LiF. The beaker was sealed, and a few holes were created in the cap. The mixture was stirred at 35 °C for 24 hours, and the resulting product was washed with DI water and centrifuged (2 minutes at 3500 rpm, repeated 3 times; 5 minutes at 3500 rpm, repeated 7 times). Subsequently, the product was sonicated for 1 hour at 5 °C and centrifuged at 3500 rpm for 30 minutes. The resulting reaction product, Ti₃C₂T_x, was collected from the top of the centrifuge tubes. To fabricate NFMX, a delaminated MXene solution was centrifuged at 3000 rpm for 30 minutes, followed by centrifugation at 7000 rpm for 30 minutes at 5 °C. The NFMX solution was prepared by diluting an NFMX solution in DI water. A 1 mL NFMX solution containing 10 mg of NFMX was dissolved in 100 mL of DI water. After the centrifugation process, the supernatant was collected, and the concentration was estimated to be approximately 0.02 mg/mL.

-Fabrication of α -Fe₂O₃ and NFMX/Fe₂O₃ photoanode

The FeOOH was synthesized on FTO at 100 °C by using a 150 mM FeCl₃·6H₂O solution for 3 hours. The sample was cleaned with DI water and dried with N₂ gas before being inserted into a tube furnace and then annealed at 800 °C for 20 minutes to convert it to α -Fe₂O₃.

Using the NFMX solution (0.025 mg/mL), α -Fe₂O₃ was centrifuged at 1000 rpm for 10 min and repeated several times. As-prepared NFMX/Fe₂O₃ was washed with DI water and dried with N₂ gas and then annealed at 100 °C for 1 hour.

-Fabrication of NiFe(OH)_x/NFMX/Fe₂O₃ photoanode

To decorate the NiFe(OH)_x co-catalyst, a solution of iron(III) 2-ethylhexanoate and nickel(II) 2-ethylhexanoate in a hexane solution (total metal complex concentration of 15% w/w) was drop-casted onto the surface using 10 μ L of solution. The solution was diluted with hexane and exposed to UV light before being annealed at 100 °C for 1 hour.

-Electrochemical Measurements

All photoelectrochemical (PEC) measurements were conducted in a three-electrode under front-side simulated Air Mass 1.5 Global (AM 1.5 G) illumination. The cell comprised of an Ag/AgCl (KCl sat.) reference electrode and a Pt mesh counter electrode. The photoanode had an exposed area of 0.2 cm², and 1.0 M NaOH solution served as a pH 13.6 electrolyte. The potential vs. RHE was calculated using

the Nernst equation $E_{\text{RHE}} = E_{\text{Ag/AgCl}} + 0.0591(\text{pH}) + 0.1976 \text{ V}$. The current density-voltage (J-V) curve was recorded at a scan rate of 20 mV s^{-1} . Photocurrent stability tests were performed by measuring the photocurrent under AM 1.5 G illumination at 1.23 V vs. RHE. Electrochemical impedance spectroscopy (EIS) was carried out using a potentiostat at a frequency range of 100 kHz to 0.1 Hz . The experimental EIS data were analyzed and fitted using Zview software. The incident photon to current conversion efficiency (IPCE) was measured under monochromatic light by a Xe lamp, and the intensity of the monochromatic light was measured by a luminometer.

4.3 Results and discussion

4.3.1 Fabrication process and morphology of NFMX/Fe₂O₃

Figure 4-1a illustrates the fabrication procedures of nanofragment MXene (NFMX) and NFMX decorated α -Fe₂O₃ (NFMX/Fe₂O₃). Briefly, MXene (Ti₃C₂T_x; T: functional groups) sheets were obtained through etching MAX (Ti₃AlCl₂) in a 9 M HCl solution for 24 hours at 35 °C and a centrifuge process¹⁴ and NFMXs were collected by directly cutting MXene sheets through a centrifuge process.

The scanning electron microscopy (SEM) and transmission electron microscopy (TEM) images revealed the morphologies of MAX, MXene sheets, α -Fe₂O₃, and NFMX/Fe₂O₃. In **Figure 4-1c**, MXene sheets showed a 2D layer structure, which is different from the bulk MAX powder in **Figure 4-1b**. α -Fe₂O₃ showed a worm-like structure with ~80 nm diameter (**Figure 4-1d**) and NFMX/Fe₂O₃ exhibited similar morphological features with α -Fe₂O₃ except for the deposition of nanosize fragments on the surface of α -Fe₂O₃ (**Figure 4-1e**). The size of NFMX was further confirmed to be an average of 8 nm by dynamic light scattering (DLS; **Figure 4-2**) and TEM images (**Figure 4-3**).

NFMX was obtained by cutting 2D MXene sheets directly through a centrifuge process, resulting in a polydisperse solution of MXene fragments. Through a typical dip coating method, MXene fragments of several tens of nanometers or larger could be deposited on the surface of α -Fe₂O₃ in the form of bulky sheets¹⁵, as depicted in **Figures 4-4b,c**. It resulted in lowering the photoelectrochemical (PEC) performance of α -Fe₂O₃ by blocking water contact with the hematite and light absorption by α -Fe₂O₃ (**Figure 4-4d**).

To deposit NFMX onto α -Fe₂O₃, we first collected MXene fragments smaller than 10 nm from the supernatant as shown in **Figure 4-1a₁**. Subsequently, the centrifuge-assisted coating method was employed to fabricate NFMX/Fe₂O₃ (**Figure 4-1a₃**). During the centrifuge process, floating NFMX adhered to the surface of α -Fe₂O₃ through centrifugal force.²⁸

To verify the characteristics and size of NFMX on the α -Fe₂O₃, transmission electron microscopy (TEM) was performed. In **Figure 4-1f**, α -Fe₂O₃ shows a lattice spacing of 0.25 nm, consistent with the hematite (110) plane. The TEM image in **Figure 4-1g** clearly illustrated the deposition of NFMX on the surface of α -Fe₂O₃ and NFMX shows a lattice spacing of 0.26 nm, corresponding to the Ti₃C₂ (100) plane (**Figure 4-5**). The inverse fast Fourier-Transform (IFFT) image in the inset of **Figure 4-1g** illustrated the highly crystalline property of NFMX.¹⁶ The distribution of Ti and C, as revealed by high-angle annular dark-field scanning TEM-energy-dispersive spectroscopy (HAADF-STEM-EDS) mapping images in **Figure 4-1h**, confirmed the uniform deposition of NFMX on the surface of α -Fe₂O₃.

The atomic percentage of Ti in NFMX/Fe₂O₃, estimated from X-ray photoelectron spectroscopy (XPS) results, was found to be ~1.8% (Ti/Fe ~0.11) (**Figure 4-6**). The optimization process of NFMX solution concentration was carried out as long as the light absorption of α -Fe₂O₃ was not hindered (**Figure 4-7**).

X-ray diffraction (XRD) patterns and Raman spectra were performed to check the crystallinity and structure of the NFMX and NFMX/Fe₂O₃. In **Figure 4-8a**, both α -Fe₂O₃ and NFMX/Fe₂O₃ showed the peaks of hematite (110) and (300) plane and additional SnO₂ peaks, which arise from the FTO (fluorine-doped tin oxide) substrate. Because of the few amount of NFMX compared to α -Fe₂O₃, it is hard to distinguish the presence of XRD. These trends are similar in Raman spectra due to the much lower peak intensities of NFMX than that of α -Fe₂O₃ (**Figure 4-9**).

Further characterizations were conducted by XPS, Fourier transform infrared spectroscopy (FT-IR), X-ray absorption near edge structure (XANES), and extended X-ray absorption fine structure (EXAFS) for the Fe-K edges. In XPS O 1s spectra, three types of oxygen species were observed in α -Fe₂O₃: lattice oxygen species (O_L) at ~529.53 eV, metal-oxygen species near oxygen vacancies (O_V) at ~530.78 eV, and chemisorbed oxygen species from water molecules (O_C) at ~531.88 eV (**Figure 4-8b**). In the case of NFMX/Fe₂O₃, due to the presence of large functional groups on NFMX, higher intensities were observed at ~530.78 eV, 531.88 eV, and 533.16 eV, corresponding to the C-Ti-O_x, C-Ti-OH, and H₂O species, respectively (**Figure 4-8c**).¹⁷ Additionally, only NFMX/Fe₂O₃ exhibited peaks related to Ti-C (454.6 eV), Ti²⁺ (455.1 eV and 461.1 eV), Ti³⁺ (456.6 eV and 462.5 eV), and Ti-O (458.7 eV and 464.2 eV) in XPS Ti 2p spectra (**Figure 4-8d**), which were not shown in α -Fe₂O₃ (**Figure 4-10**).¹⁷ The FT-IR analysis revealed several peaks corresponding to hydroxide and carbonyl groups at -OH (~3420 cm⁻¹), C=O (~1646 cm⁻¹), O-H (~1370 cm⁻¹), and C-F (~1100 cm⁻¹) (**Figure 4-8e**)¹⁸, indicating a highly functionalized NFMX consistent with the XPS C 1s and F 1s spectra of MXene (**Figure 4-11**). **Figures 4-12,8f** demonstrate XANES and EXAFS spectra for the Fe-K edges, respectively. In XANES spectra, both α -Fe₂O₃ and NFMX/Fe₂O₃ exhibit a pre-edge peak at 7115 eV, corresponding to a quadrupole transition from 1s to 3d, indicating the characteristic structure of α -Fe₂O₃.^{19,20} EXAFS spectra reveal two distinct peaks at 0.8-2.0 Å (nearest Fe-O bond) and 2.1-3.9 Å (nearest Fe-O bond and Fe-Fe bond at a longer distance). The elongated Fe-O bond observed in NFMX/Fe₂O₃ compared to α -Fe₂O₃ indicates the additional Fe-O bonding between α -Fe₂O₃ and the functional groups of MXene (-O, -OH).²⁰

In addition, the surface potential of NFMX is relatively negative compared to that of α -Fe₂O₃ across the entire pH range. This suggests that trapped holes present at the surface of hematite can be readily extracted by the electrostatic force of NFMX, thereby enhancing the surface charge separation efficiencies in NFMX/Fe₂O₃ (**Figure 4-13**).

4.3.2 PEC activities of NFMX/Fe₂O₃

The PEC activities of NFMX/Fe₂O₃ were explored in **Figure 4-14**. The photocurrent density was measured through linear scan voltammetry (LSV) curves under 1 SUN (AM 1.5 G, 100 mW/cm²) and dark conditions in a 1.0 M NaOH solution. In **Figure 4-14a**, NFMX/Fe₂O₃ achieved a photocurrent density of 1.77 mA cm⁻², which is 1.59 times higher than that of α-Fe₂O₃. The enhanced photocurrent density of NFMX/Fe₂O₃ is primarily attributed to the improved charge transfer efficiency facilitated by the functionalized NFMX. This was revealed by evaluating surface (η_{surface}) and bulk (η_{bulk}) charge separation efficiencies. To calculate the η_{surface} and η_{bulk} , J-V curves are measured using the mixture solution of 1.0 M NaOH and hole scavenger (0.2M Na₂SO₃) under 1 SUN, as depicted in **Figure 4-16**. At 1.23 V_{RHE}, the calculated η_{surface} and η_{bulk} of NFMX/Fe₂O₃ showed 28% and 58%, respectively, which values are notably increased from the η_{surface} and η_{bulk} of α-Fe₂O₃ (**Figures 4-14b,c**). This improvement can be attributed to the relatively negative surface charge and high conductivity of NFMX.

These results are supported by electrochemical impedance spectroscopy (EIS), four-point probe measurements, and current-voltage (I-V) characteristics. The Nyquist plot, fitted by the inset circuit of **Figure 4-17a**, illustrates the trapping resistance (R_{trap}) and charge transfer resistance (R_{ct}).²¹ NFMX/Fe₂O₃ presented reduced values of R_{trap} and R_{ct} in the potential range from 0.9 – 1.3 V_{RHE}, verifying the efficient charge transfer effect of NFMX (**Figures 4-17a-c**), which was supplemented by the I-V characteristics and four-point probe measurements in **Figure 4-18**.

In **Figure 4-17d**, the density of mid-gap surface states (N_{ss}), associated with OH- and O-terminated surfaces, was determined by calculating C_{trap} (**Figure 4-20**). The higher N_{ss} values of NFMX/Fe₂O₃ compared to α-Fe₂O₃ near the water oxidation potential can be explained by the large functional groups of NFMX, which increase the hole-accepting species.²² Moreover, NFMX/Fe₂O₃ showed high carrier density and active surface area than that of α-Fe₂O₃, consistent with the higher N_{ss} values. The carrier density and active surface area were calculated from the Mott-Schottky plots and the electrochemically active surface area (ECSA) curves in **Figures 4-17e,f**, respectively.

Open circuit potential (OCP) measurements were conducted under 1 SUN and dark conditions to investigate the Fermi level pinning at the semiconductor/electrolyte interface (SEI) (**Figure 4-21a**). NFMX/Fe₂O₃ showed a higher OCP value, indicating reduced Fermi level pinning and enhanced charge separation at the SEI.²³ The lower spike of NFMX/Fe₂O₃ compared to α-Fe₂O₃ after the instantaneous light-off in the transient photocurrent density curve suggested a reduced surface charge recombination rate (**Figure 4-21b**) and the delay of the steady-state cathodic current (t_2) after the instantaneous light-off (t_1) of NFMX/Fe₂O₃ in the transient cathodic current analysis (**Figure 4-21c**) indicated the presence of long-lived holes at the surface due to NFMX, in contrast to α-Fe₂O₃.⁷

While NFMX enhances the PEC activities of α -Fe₂O₃, it is important to consider that NFMX is susceptible to oxidation in an aqueous solution due to its high reactivity. The cyclic voltammetry (CV) curves clearly show an oxidation signal for NFMX/Fe₂O₃, which was not observed in α -Fe₂O₃ (**Figure 4-22**).²⁴ As seen in **Figure 4-21d**, the photocurrent density of NFMX/Fe₂O₃ gradually decreased (retention 69%) over 100 minutes while α -Fe₂O₃ showed high stability after 120 minutes (retention ~94%). It elucidate the difficulty of using highly reactive MXene alone for the PEC reaction of the hematite photoanode and emphasize the need for constructing a stable system.

4.3.3 PEC activities of NiFe(OH)_x/NFMX/Fe₂O₃

Considering the role of NFMX for PEC activities and resolving the poor stability of NFMX, a highly efficient NiFe(OH)_x co-catalyst was deposited in the form of a thin overlayer on the surface of α -Fe₂O₃ and NFMX/Fe₂O₃ using a photochemical method (**Figures 4-23b,c**). It is well known that NiFe(OH)_x co-catalyst can improve the surface charge transfer rate (K_{surf} , red arrow) of α -Fe₂O₃ by passivating the surface states and reducing Fermi level pinning as shown in **Figure 4-23a**.²⁵ The NiFe(OH)_x with an optimized amount was deposited, and due to the transparent nature of NiFe(OH)_x, its deposition on NFMX/Fe₂O₃ did not affect the light absorption region (**Figure 4-24**). The characterization of NiFe(OH)_x was further conducted by XPS as shown in **Figure 4-25**.

By incorporating NFMX as a hole transport medium between NiFe(OH)_x and α -Fe₂O₃, not only was the surface transfer rate improved, but also the large bulk recombination rate was effectively minimized. This notable enhancement can be attributed to the superior hole extraction and transport properties of NFMX, which are facilitated by its negative surface charge (**Figure 4-13**) and high electrical conductivity (**Figure 4-18**). In **Figure 4-23d**, NiFe(OH)_x/NFMX/Fe₂O₃ exhibited a photocurrent density of 3.09 mA cm⁻² at 1.23 V_{RHE}, which is 2.78 and 1.4 times higher than that of α -Fe₂O₃ and NiFe(OH)_x/Fe₂O₃, respectively due to the improved surface and bulk charge separation efficiencies as shown in **Figure 4-26**. Furthermore, NiFe(OH)_x/NFMX/Fe₂O₃ showed an onset potential of 0.62 V_{RHE}, which was ~0.2 V cathodic shifted compared to α -Fe₂O₃, indicating a significant decrease in thermodynamic overpotential (the onset potential was determined at the voltage when the photocurrent density reached 0.2 mA cm⁻², **Figure 4-27**). These results revealed the synergistic effect of NiFe(OH)_x and NFMX catalyst.

As seen in **Figures 4-23b,c**, NiFe(OH)_x is deposited as an overlayer on the surface of α -Fe₂O₃ and NFMX/Fe₂O₃, blocking intimate contact with the NaOH electrolyte. Thus, unlike the NFMX/Fe₂O₃, NiFe(OH)_x/NFMX/Fe₂O₃ showed an excellent stability of ~100% for 60 hours in J-t measurement

(**Figure 4-23e**), which was proved by the CV curves shown in **Figure 4-28**. According to the gas chromatography (GC) measurements in **Figure 4-23f**, a notable faradaic efficiency of ~90% was observed for 150 minutes. The incident photon to electron conversion efficiency (IPCE) curves illustrated a substantial improvement in photo-response within the 300 to 400 nm range for NiFe(OH)_x/NFMX/Fe₂O₃ compared to α-Fe₂O₃, suggesting an enhanced photo-response achieved through the decoration of NiFe(OH)_x and NFMX (**Figure 4-29**).

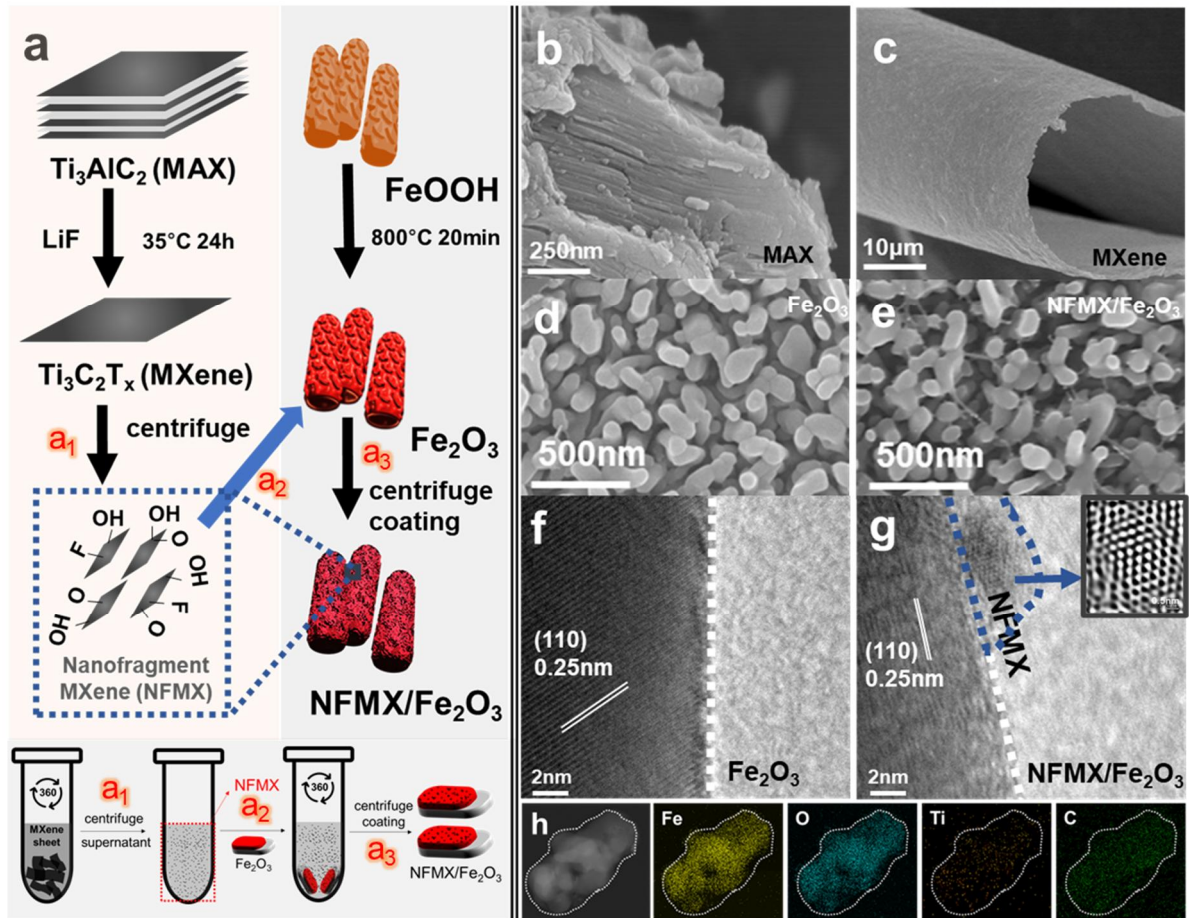


Figure 4-1. Fabrication process and morphology of NFMX/Fe₂O₃. (a) Fabrication process of NFMX/Fe₂O₃. SEM images of (b) MAX, (c) MXene sheets, (d) α -Fe₂O₃, and (e) NFMX/Fe₂O₃. TEM images of (f) α -Fe₂O₃, and (g) NFMX/Fe₂O₃ (the inset image shows the IFFT image of the selected area of **Figure 4-1g**). (h) HAADF-STEM-EDS mapping images of each element of NFMX/Fe₂O₃.

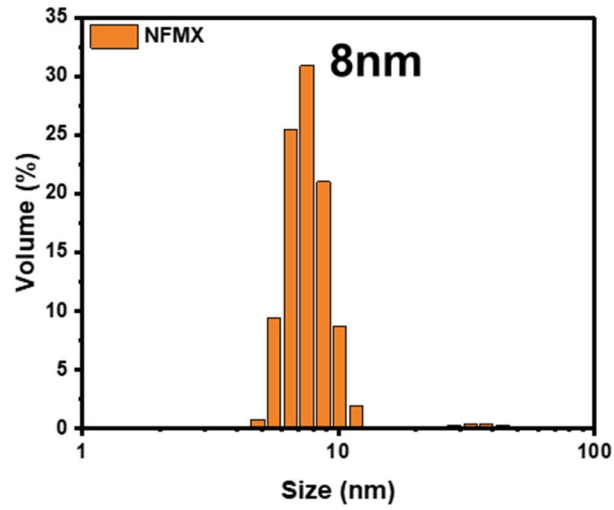


Figure 4-2. DLS measurement of an optimized NFMX solution.

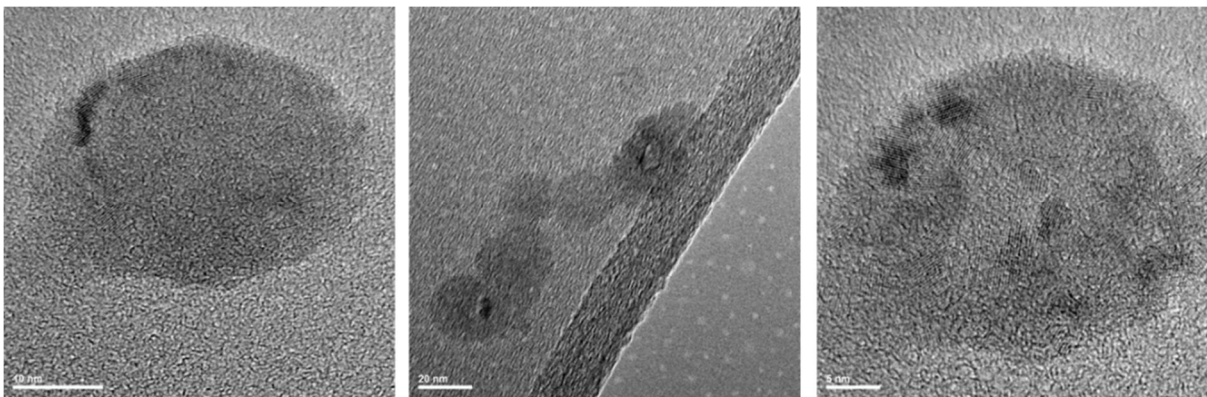


Figure 4-3. TEM images of NFMX.

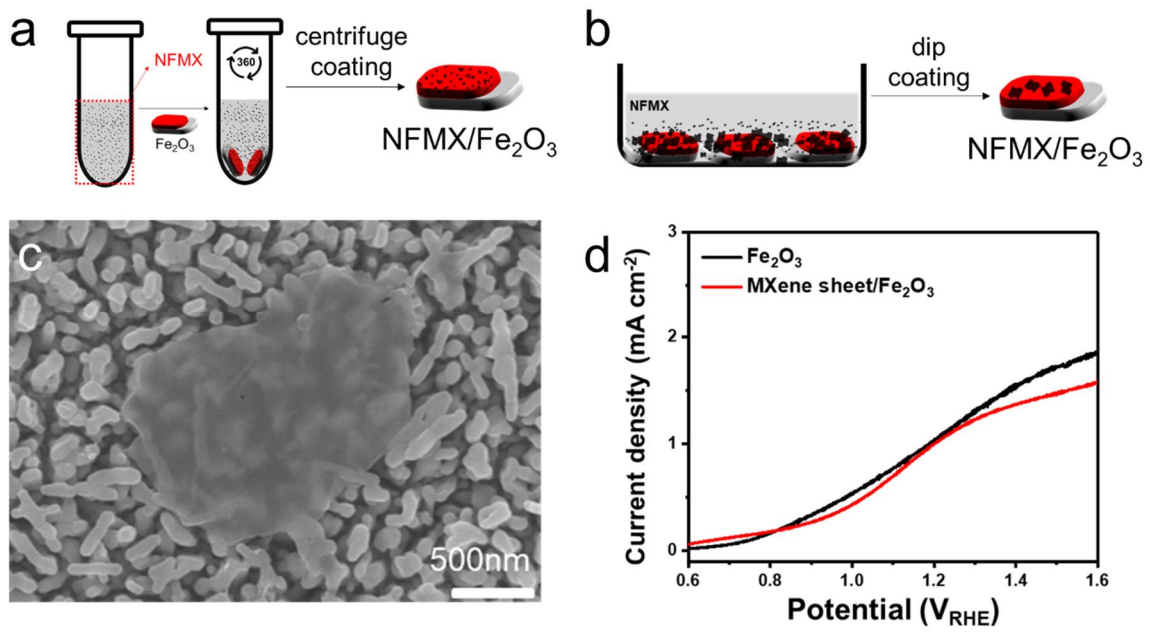


Figure 4-4. Fabrication methods of NFMX/Fe₂O₃. (a) Centrifuge coating method and (b) dip coating method. (c) SEM image of MXene sheet/Fe₂O₃. (d) J-V curves of α -Fe₂O₃ and MXene sheet/Fe₂O₃.

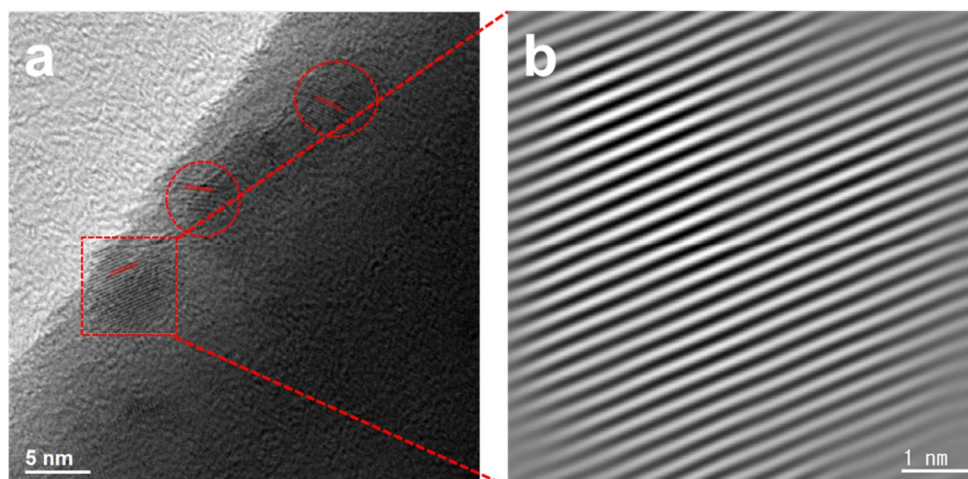


Figure 4-5. (a) TEM image, and (b) IFFT image of NFMX/Fe₂O₃.

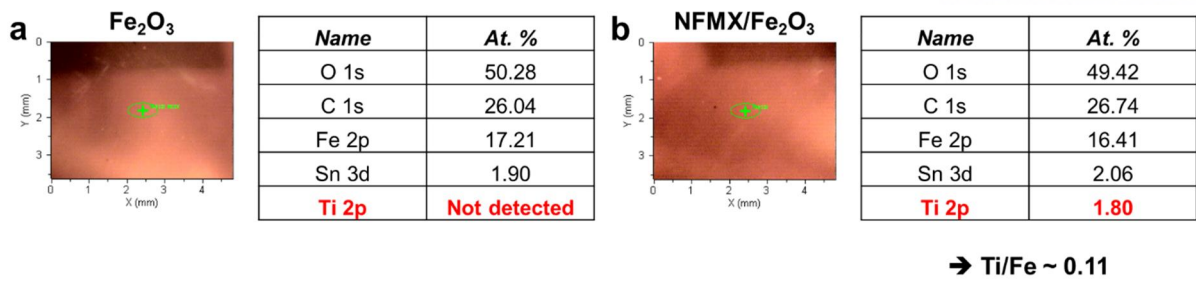


Figure 4-6. XPS atomic percentage of (a) $\alpha\text{-Fe}_2\text{O}_3$ and (b) NFMX/ Fe_2O_3 .

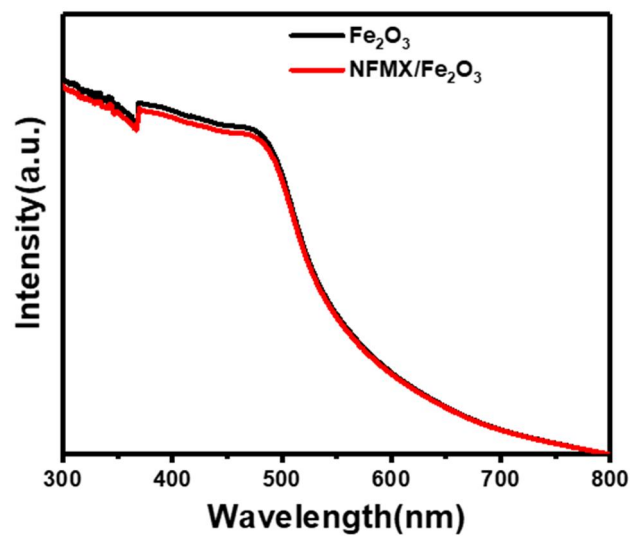


Figure 4-7. UV-Vis absorption spectra of $\alpha\text{-Fe}_2\text{O}_3$ and NFMX/ Fe_2O_3 .

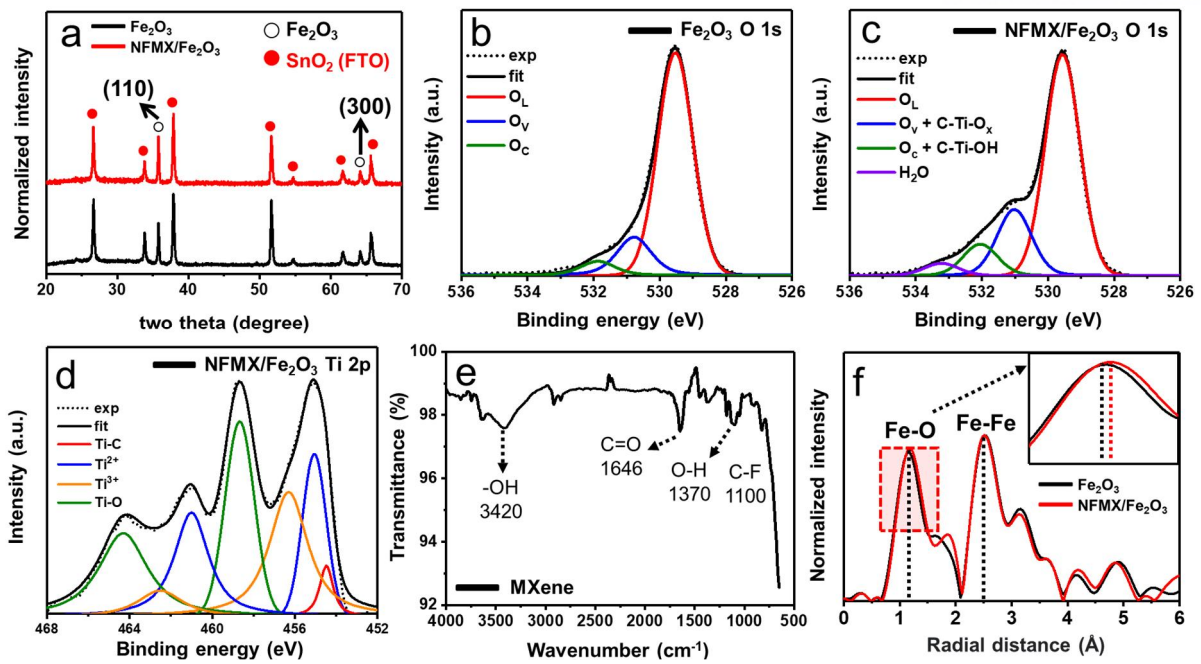


Figure 4-8. Characterization of NFMX/Fe₂O₃. (a) XRD patterns of α -Fe₂O₃ and NFMX/Fe₂O₃. XPS O 1s spectra of (b) α -Fe₂O₃ and (c) NFMX/Fe₂O₃. (d) XPS Ti 2p spectra of NFMX/Fe₂O₃. (e) FT-IR spectrum of MXene. (f) Fourier transformations of Fe K-edge EXAFS spectra of α -Fe₂O₃ and NFMX/Fe₂O₃.

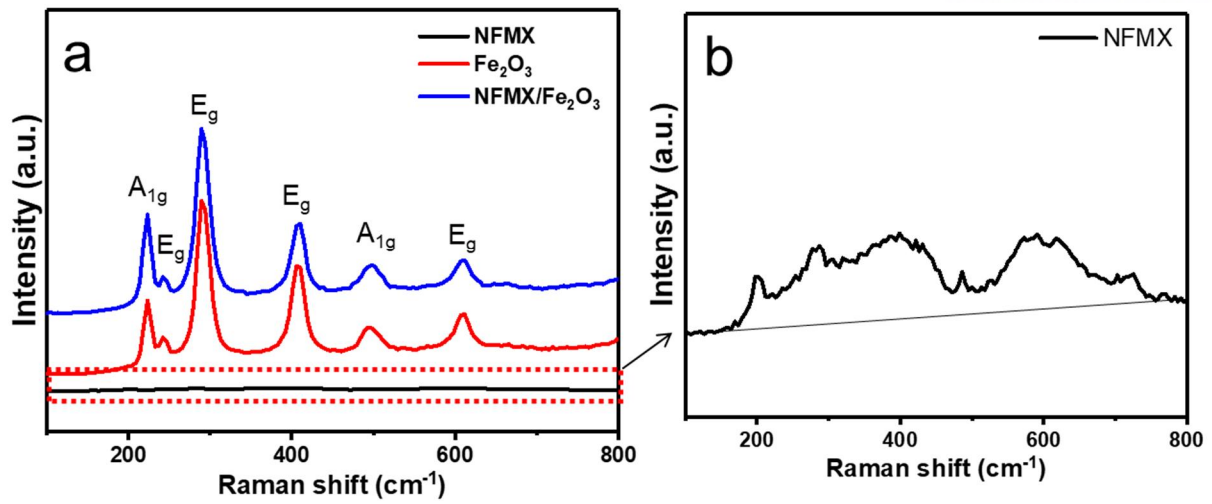


Figure 4-9. (a) Raman spectra and (b) close-up image of the selected area in Figure 4-9a.

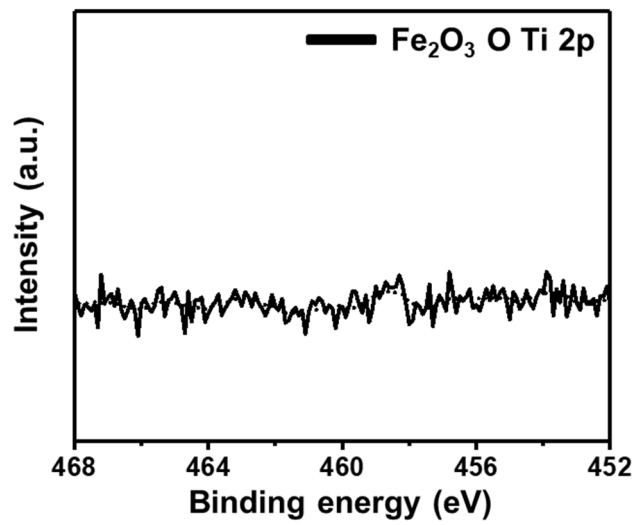


Figure 4-10. XPS Ti 2p spectrum of α -Fe₂O₃.

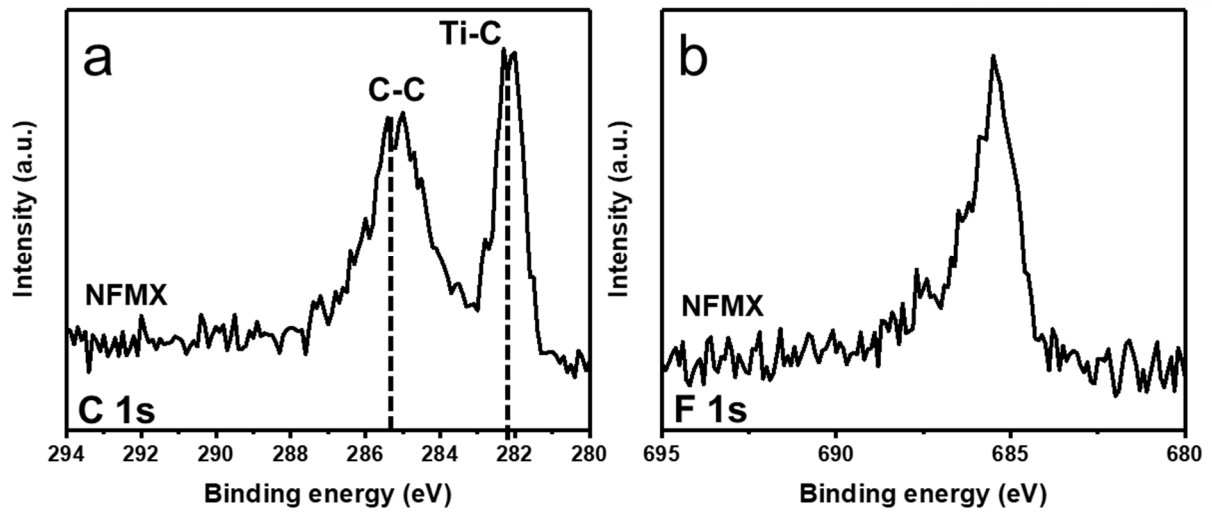


Figure 4-11. XPS spectra of (a) C 1s, and (b) F 1s of NFMX.

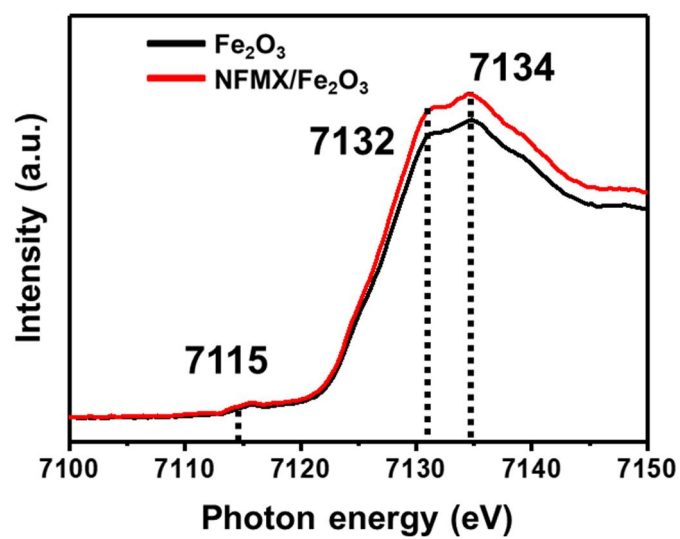


Figure 4-12. Fe-K edge XANES spectra of $\alpha\text{-Fe}_2\text{O}_3$, and NFMX/ Fe_2O_3 .

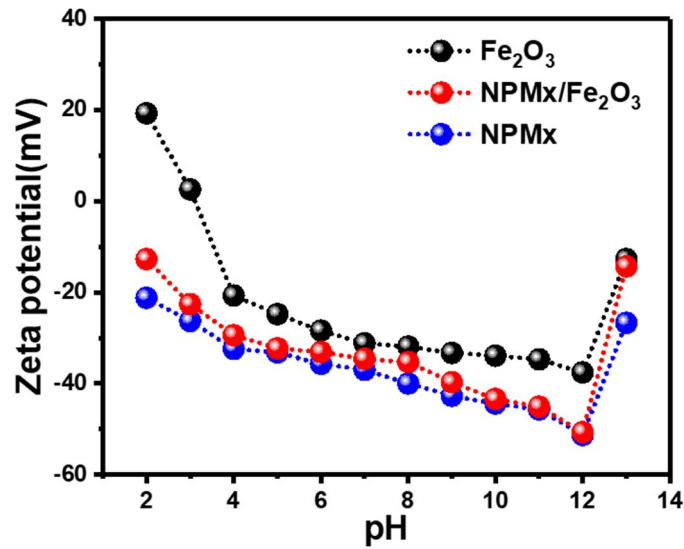


Figure 4-13. Zeta potential of α - Fe_2O_3 , NFMX/ Fe_2O_3 , and NFMX.

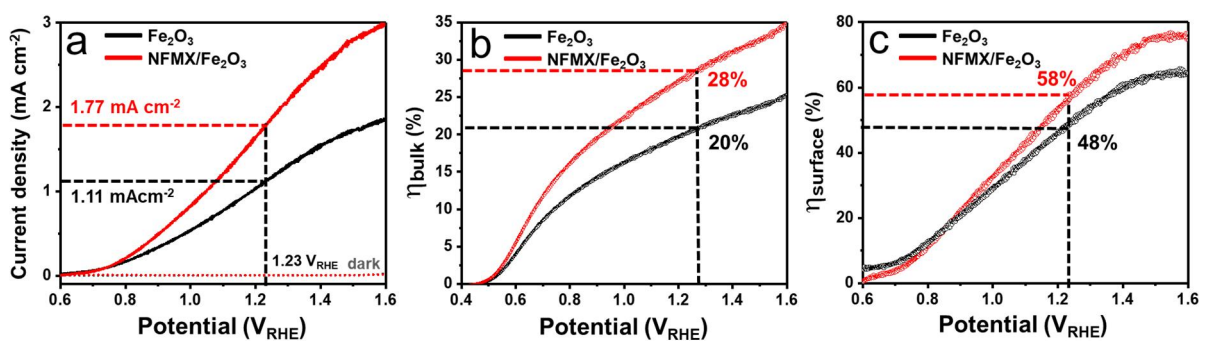


Figure 4-14. PEC activities of NFMX/ Fe_2O_3 . (a) J-V curves under 1 SUN and dark conditions. Charge separation efficiencies at the (b) bulk (η_{bulk}), and (c) surface (η_{surface}) region of α - Fe_2O_3 and NFMX/ Fe_2O_3 .

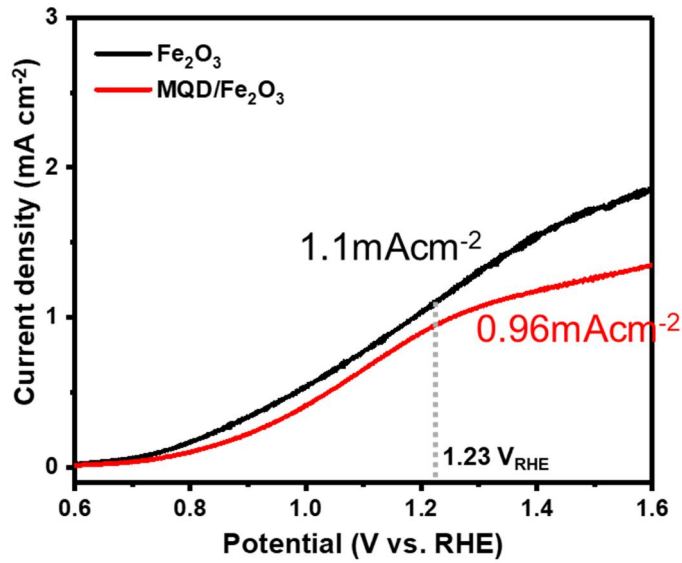


Figure 4-15. J-V curves of α -Fe₂O₃ and MQD/Fe₂O₃.

Note: To compare the charge transfer properties of MXene quantum dots (MQDs) with NFMX, we decorated MQDs on the surface of α -Fe₂O₃. MQD/Fe₂O₃ exhibited a reduced photocurrent density at 1.23 V_{RHE} compared to α -Fe₂O₃, attributed to the sluggish surface charge transfer caused by the polyethyleneimine passivation layer and it reveals the superior surface charge transfer property of NFMX than MQD.

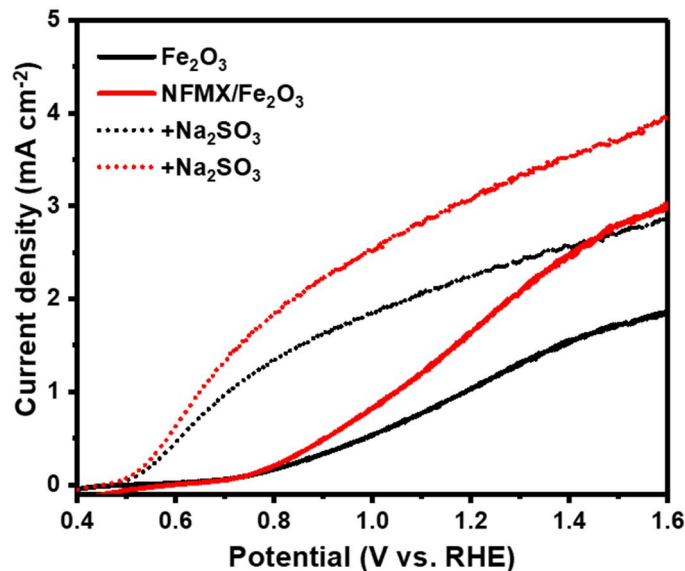


Figure 4-16. J-V curves of α -Fe₂O₃ and NFMX/Fe₂O₃ with 1.0 M NaOH (solid line) and with a solution mixture of 1.0 M NaOH and 0.2 M Na₂SO₃ (dotted lines).

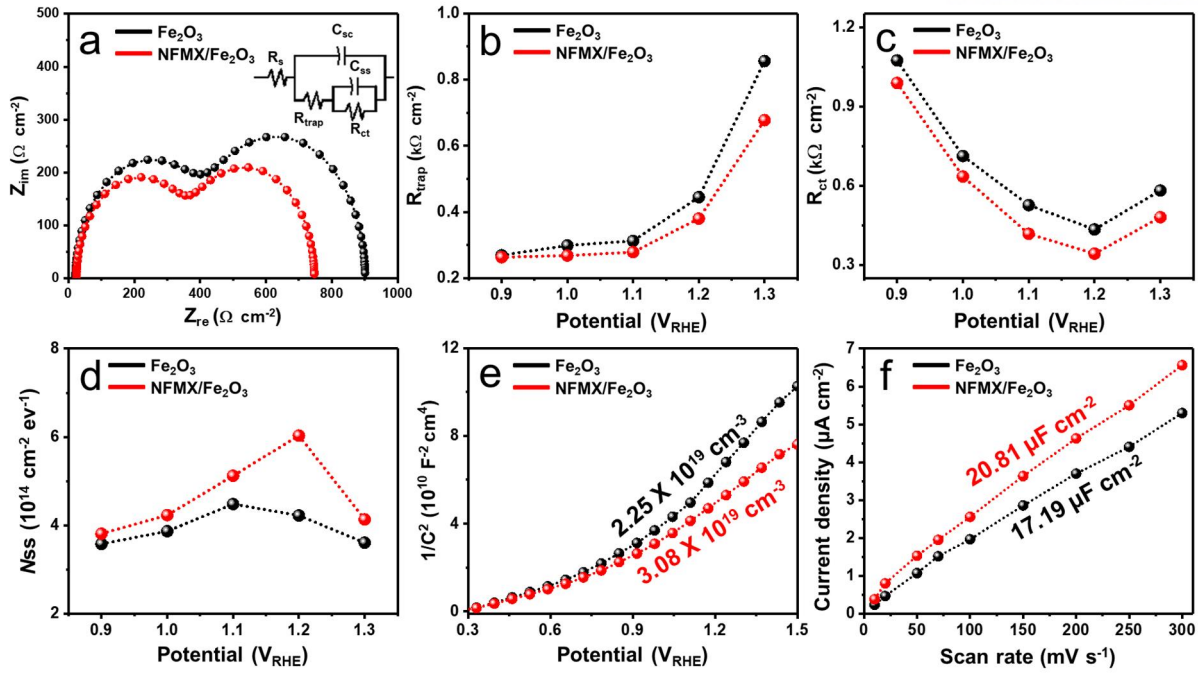


Figure 4-17. PEC activities of NFMX/Fe₂O₃. (a) EIS measurements at 1.23 V_{RHE} (inset image shows the circuit model), (b) R_{trap}, (c) R_{ct}, (d) N_{ss} at different applied potentials under 1 SUN, (e) Mott-Schottky plots under dark condition, and (f) ECSA curves of α-Fe₂O₃, and NFMX/Fe₂O₃.

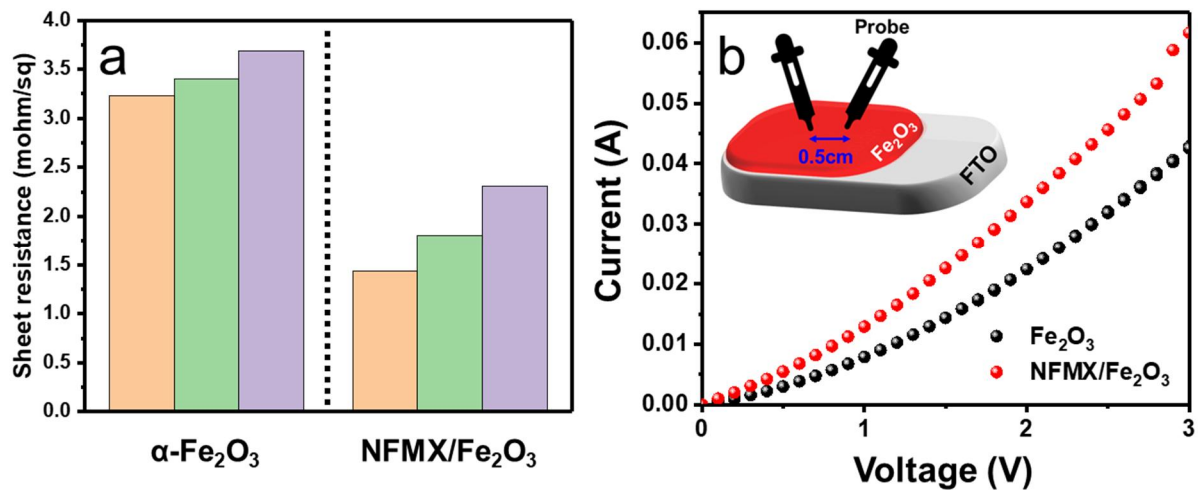


Figure 4-18. (a) Four-point-probe measurements, and (b) I-V characteristics of α-Fe₂O₃, and NFMX/Fe₂O₃.

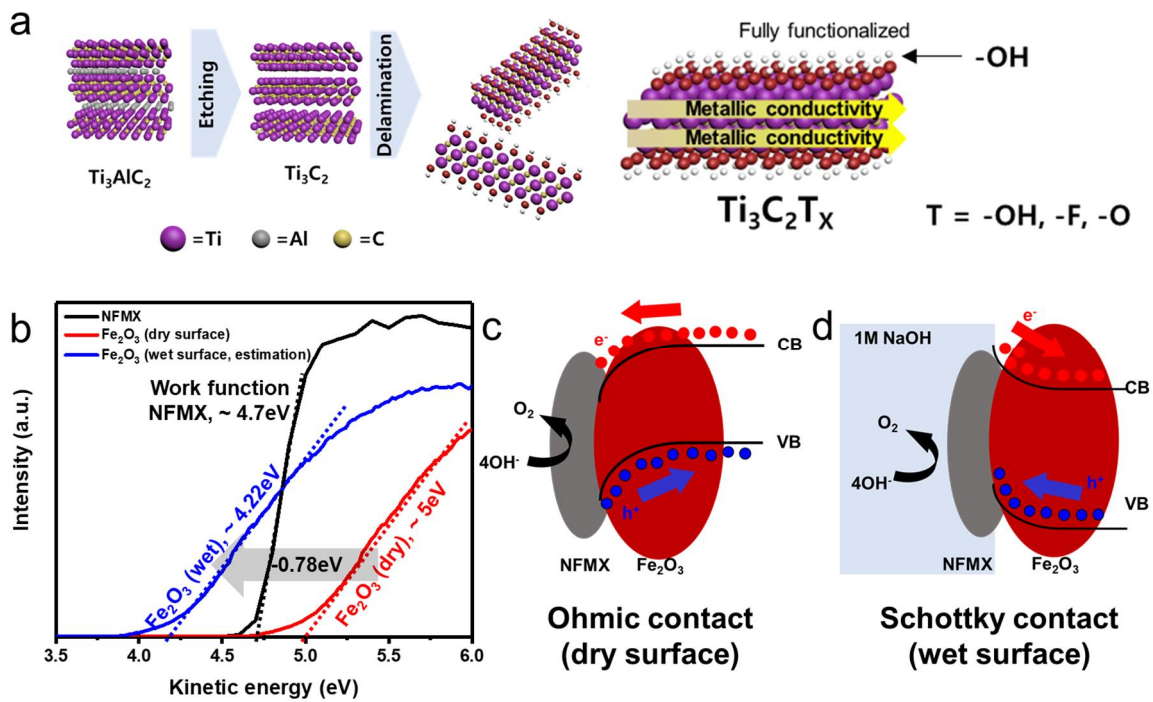


Figure 4-19. (a) Fabrication procedure of MXene and electronic structure. (b) UPS of NFMX, and α - Fe_2O_3 under dry and wet surface conditions. Schematics of (c) Ohmic contact and (d) Schottky contact of NFMX/ Fe_2O_3 .

Note: When the metallic material (MXene, **Figure 4-19a**) and semiconductor (hematite) are combined, the Ohmic or Schottky contact can be formed, which is determined by considering the work function of each material. In air condition, the work function of α - Fe_2O_3 (5.0 eV) is larger than that of NFMX (4.7 eV), constructing an unfavorable Ohmic contact (**Figures 4-19b,c**). However, as reported before²⁶²⁷, the water exposure of α - Fe_2O_3 (dry surface to wet surface) creates a favorable alignment of the heterojunction by decreasing the work function of α - Fe_2O_3 ~ -0.78 eV (**Figure 4-19b**)²⁸. In that case, a desirable Schottky contact can be formed as shown in **Figure 4-19d**. In other words, during the PEC water splitting reaction, the NFMX/ Fe_2O_3 showed a Schottky contact, which is favorable for a photoelectrochemical water oxidation reaction.

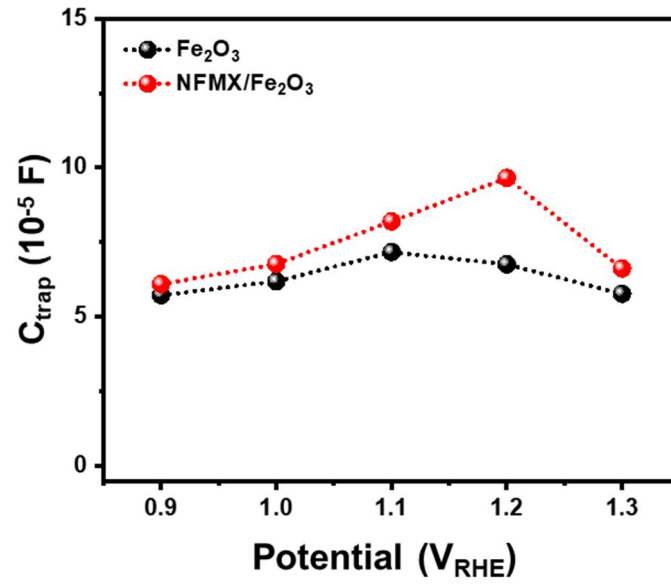


Figure 4-20. C_{trap} at different applied potentials.

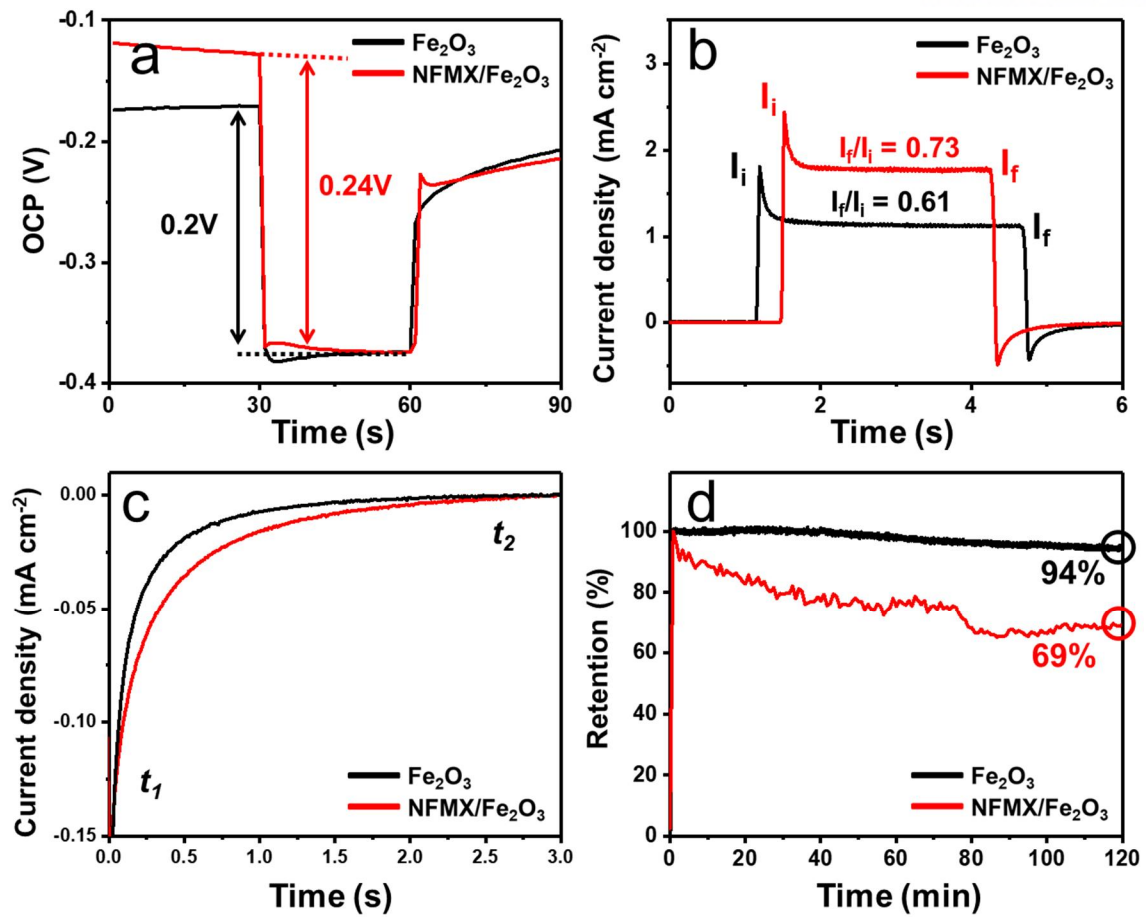


Figure 4-21. (a) OCP measurements, (b) transient photocurrent density curves at 1.23 V_{RHE} , (c) cathodic photocurrent density at 1.23 V_{RHE} after instantaneous light-off condition, and (d) retention (%) of photocurrent density at 1.23 V_{RHE} for 120 minutes of $\alpha\text{-Fe}_2\text{O}_3$ and NFMX/ Fe_2O_3 .

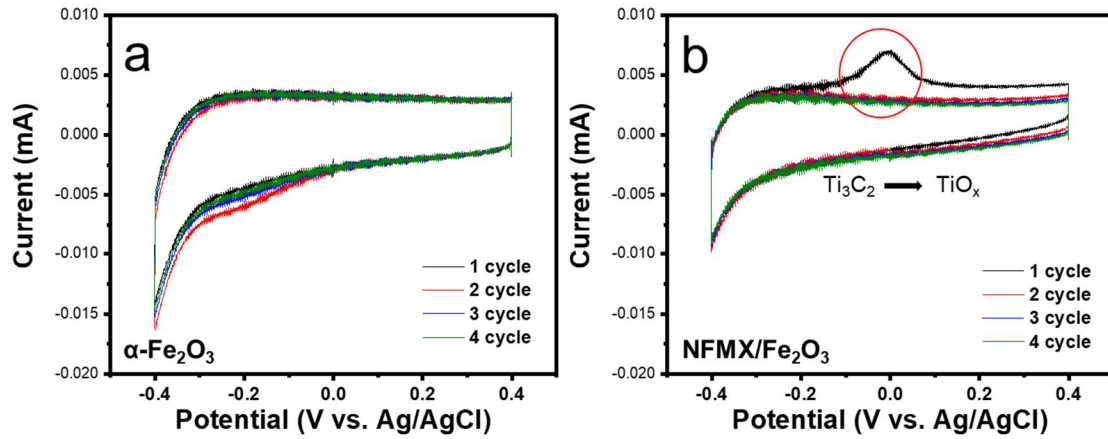


Figure 4-22. CV curves at 100 mV/s scan rate of (a) $\alpha\text{-Fe}_2\text{O}_3$ and (b) NFMX/ Fe_2O_3 .

Note: Oxidation reaction of Ti_3C_2 : $\text{Ti}_3\text{C}_2 + 3\text{O}_2 = 3\text{TiO}_2 + 2\text{C}$

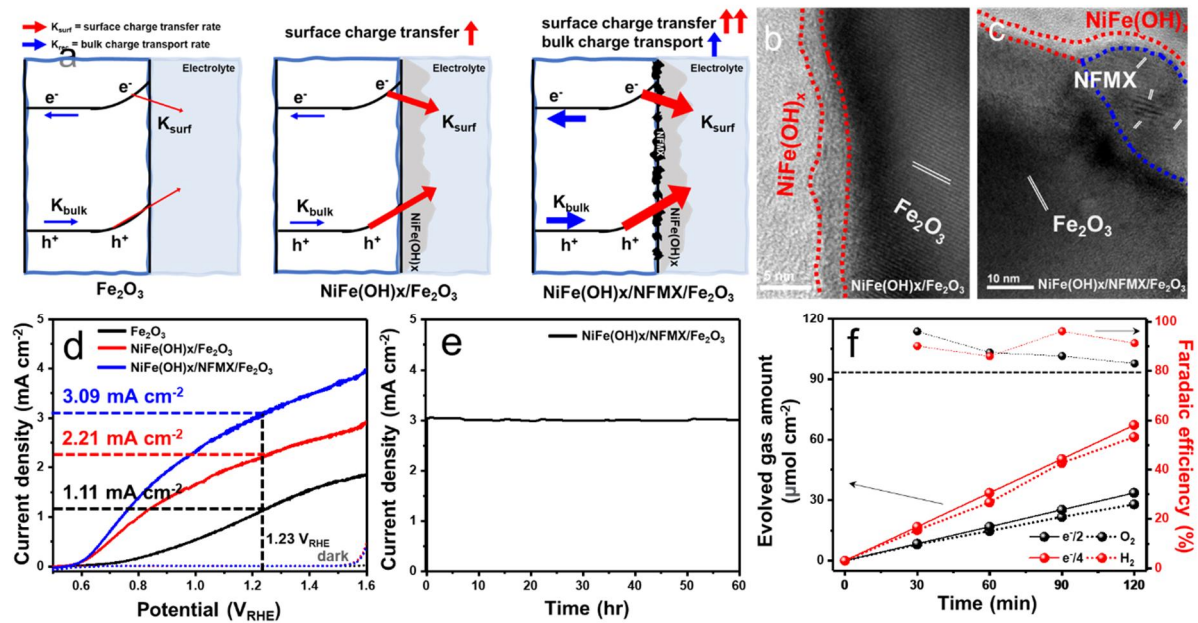


Figure 4-23. PEC activities of $\text{NiFe(OH)}_x/\text{NFMX}/\text{Fe}_2\text{O}_3$. (a) PEC reaction process of $\alpha\text{-Fe}_2\text{O}_3$, $\text{NiFe(OH)}_x/\text{Fe}_2\text{O}_3$, and $\text{NiFe(OH)}_x/\text{NFMX}/\text{Fe}_2\text{O}_3$ (red arrow: surface charge transfer rate to the electrolyte, blue arrow: bulk charge transport rate, the thickness of each arrow illustrates the intensity of each process). TEM images of (b) $\text{NiFe(OH)}_x/\text{Fe}_2\text{O}_3$ and (c) $\text{NiFe(OH)}_x/\text{NFMX}/\text{Fe}_2\text{O}_3$. (d) J-V curves under 1 SUN and dark conditions. (e) J-t measurement for 60 hours, and (f) Evolved gases and faradaic efficiency for 120 minutes of $\text{NiFe(OH)}_x/\text{NFMX}/\text{Fe}_2\text{O}_3$ at $1.23 V_{\text{RHE}}$.

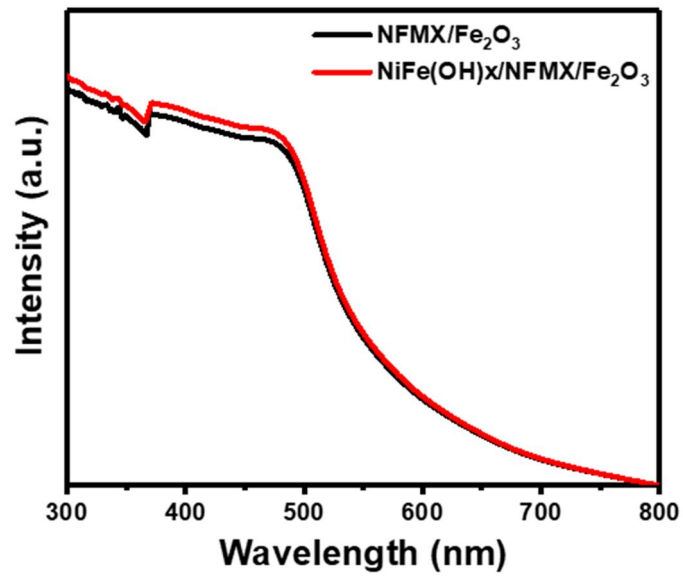


Figure 4-24. UV-Vis absorption spectra of NFMX/Fe₂O₃, and NiFe(OH)_x/NFMX/Fe₂O₃.

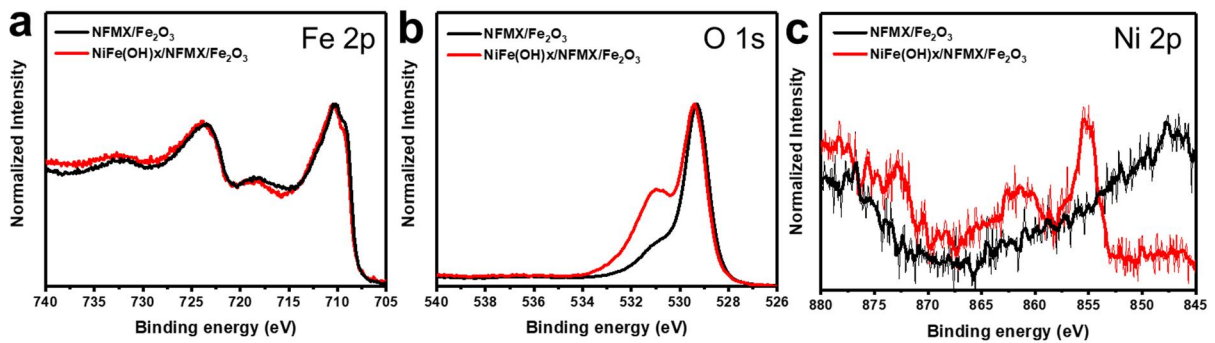


Figure 4-25. XPS spectra of (a) Fe 2*p*, (b) O 1*s*, and (c) Ni 2*p* of NFMX/Fe₂O₃ and NiFe(OH)_x/NFMX/Fe₂O₃.

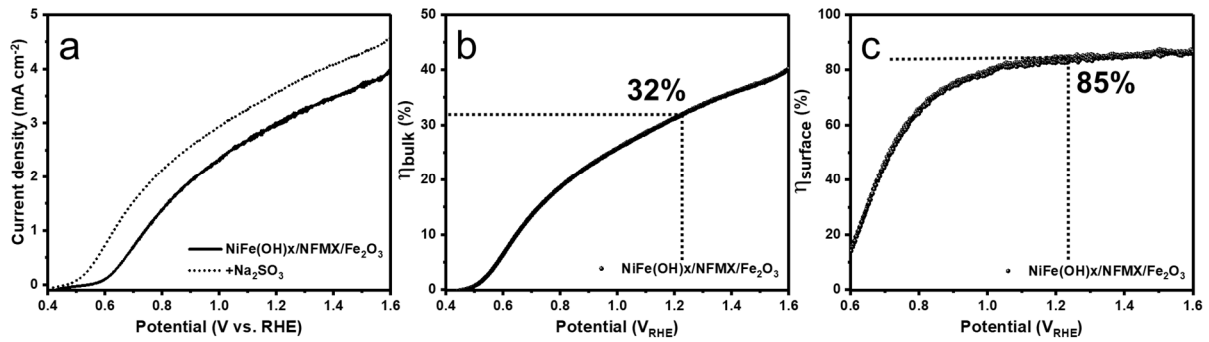


Figure 4-26. (a) J-V curves of NiFe(OH)_x/NFMX/Fe₂O₃ with 1.0 M NaOH (solid line) and with a solution mixture of 1.0 M NaOH and 0.2 M Na₂SO₃ (dotted lines), charge separation efficiencies at the (b) bulk (η_{bulk}), and (c) surface (η_{surface}) region of NiFe(OH)_x/NFMX/Fe₂O₃.

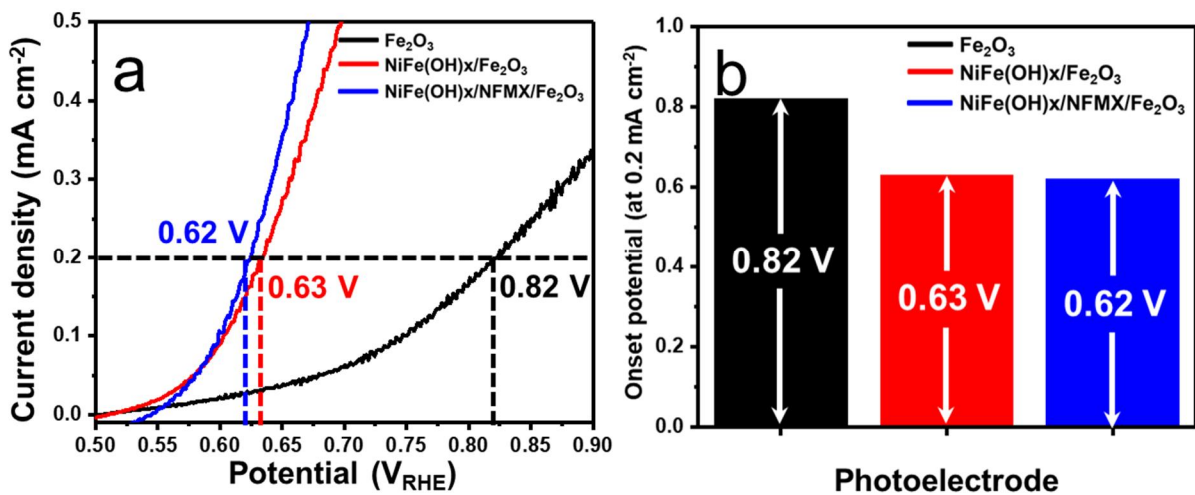


Figure 4-27. (a) J-V curves and (b) onset potential (determined at 0.2 mA cm⁻² from Figure 4-27a) of α-Fe₂O₃, NiFe(OH)_x/Fe₂O₃, and NiFe(OH)_x/NFMX/Fe₂O₃.

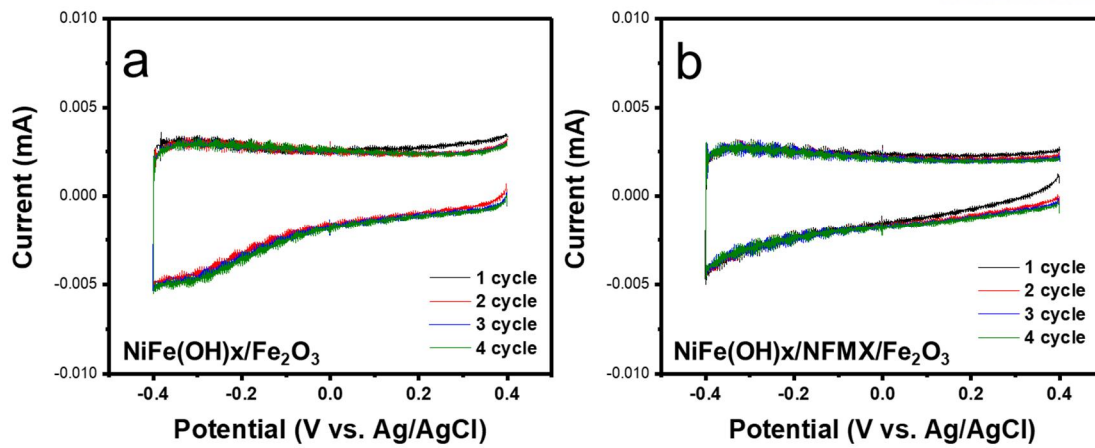


Figure 4-28. CV curves at 100 mV/s scan rate of (a) NiFe(OH)_x/Fe₂O₃ and (b) NiFe(OH)_x/NFMX/Fe₂O₃.

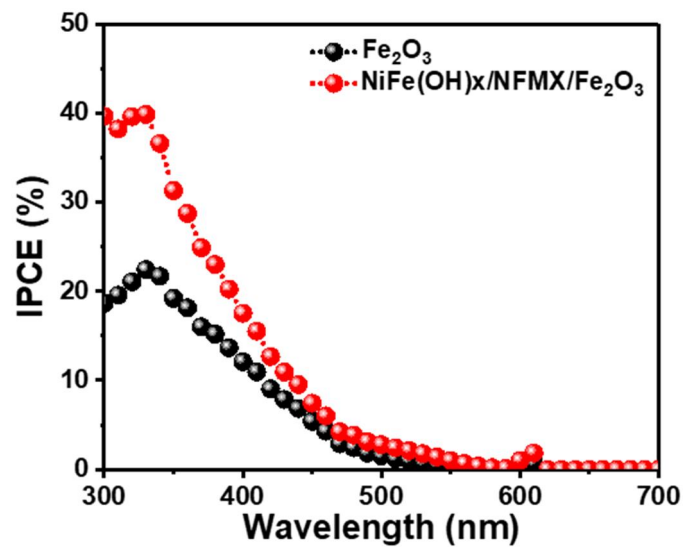


Figure 4-29. IPCE spectra of α -Fe₂O₃ and NiFe(OH)_x/NFMX/Fe₂O₃ at 1.23 V_{RHE}.

Photoanode	Co-catalyst	Photocurrent density
NiFe-Phosphate/Fe ₂ O ₃	NiFe-Phosphate	~1.20 mA cm ⁻²
NiCoAl-LDH/Fe ₂ O ₃	NiCoAl	~2.56 mA cm ⁻²
Co-Pi/Ti-Fe ₂ O ₃	Co-Pi	~0.76 mA cm ⁻²
NiFe(OH) ₂ /citrate/Fe ₂ O ₃	NiFe(OH) ₂	~0.55 mA cm ⁻²
FeO _x /Fe ₂ O ₃	FeO _x	~1.39 mA cm ⁻²
FeOOH/Fe ₂ O ₃	FeOOH	~2.40 mA cm ⁻²
Co-Pi/FeOOH/Fe ₂ O ₃	Co-Pi and FeOOH	~1.31 mA cm ⁻²
NiFeS _x /Ti-Fe ₂ O ₃	NiFeS _x	~3.0 mA cm ⁻²
NiMnO ₃ /Fe ₂ O ₃	NiMnO ₃	~2.96 mA cm ⁻²
Co-Pi/NiFeO _x /Fe ₂ O ₃	NiFeO _x and Co-Pi	~0.49 mA cm ⁻²
NFMX/Fe₂O₃	NFMX	~1.77 mA cm⁻²
NiFe(OH)_x/NFMX/Fe₂O₃	NFMX and NiFe(OH)_x	~3.09 mA cm⁻²

Table 4-1. PEC performance comparison table on hematite-based photoanodes with co-catalyst²⁹⁻³⁸. The photocurrent density was confirmed at 1.23 V_{RHE}.

4.4 Conclusion

In summary, we successfully synthesize the nanofragment MXene (NFMX) by a simple centrifuge process and demonstrate the effective utilization of NFMX as a hole transport material in conjunction with an oxygen evolution catalyst to enhance the oxygen evolution reaction performance of hematite, which is hindered by poor surface charge transfer. NFMX, with its high reactivity and efficient hole extraction and transport capabilities, proved to be an excellent hole transport material and the poor stability of NFMX in a water environment was addressed by introducing a protective NiFe(OH)_x layer, which coated on the surface of NFMX. The resulting $\text{NiFe(OH)}_x/\text{NFMX}/\text{Fe}_2\text{O}_3$ composite achieved a remarkable photocurrent density of 3.09 mA cm^{-2} at $1.23 \text{ V}_{\text{RHE}}$ and it exhibited superior stability of $\sim 100\%$ for 60 hours. This work opens up possibilities for harnessing the benefits of highly conductive MXene materials incorporated into three-dimensional photoanode materials such as BiVO_4 , $\alpha\text{-Fe}_2\text{O}_3$, and TiO_2 , leading to an efficient photoelectrochemical water splitting system.

4.5 References

1. Yi, S. S.; Wulan, B. R.; Yan, J. M.; Jiang, Q., Highly efficient photoelectrochemical water splitting: surface modification of cobalt-phosphate-loaded $\text{Co}_3\text{O}_4/\text{Fe}_2\text{O}_3$ p–n heterojunction nanorod arrays. *Advanced Functional Materials* **2019**, *29* (11), 1801902.
2. Hufnagel, A. G.; Hajiyani, H.; Zhang, S.; Li, T.; Kasian, O.; Gault, B.; Breitbach, B.; Bein, T.; Fattakhova-Rohlfing, D.; Scheu, C., Why tin-doping enhances the efficiency of hematite photoanodes for water splitting—the full picture. *Advanced functional materials* **2018**, *28* (52), 1804472.
3. Zhang, S.; Liu, Z.; Chen, D.; Yan, W., An efficient hole transfer pathway on hematite integrated by ultrathin Al_2O_3 interlayer and novel CuCoO_x cocatalyst for efficient photoelectrochemical water oxidation. *Applied Catalysis B: Environmental* **2020**, *277*, 119197.
4. Liardet, L.; Katz, J. E.; Luo, J.; Grätzel, M.; Hu, X., An ultrathin cobalt–iron oxide catalyst for water oxidation on nanostructured hematite photoanodes. *Journal of Materials Chemistry A* **2019**, *7* (11), 6012-6020.
5. Chong, R.; Wang, G.; Du, Y.; Jia, Y.; Wang, X.; Li, C.; Chang, Z.; Zhang, L., Anion engineering of exfoliated CoAl layered double hydroxides on hematite photoanode toward highly efficient photoelectrochemical water splitting. *Chemical Engineering Journal* **2019**, *366*, 523-530.
6. Li, F.; Li, J.; Gao, L.; Hu, Y.; Long, X.; Wei, S.; Wang, C.; Jin, J.; Ma, J., Construction of an efficient hole migration pathway on hematite for efficient photoelectrochemical water oxidation. *Journal of Materials Chemistry A* **2018**, *6* (46), 23478-23485.
7. Zhang, K.; Jin, B.; Park, C.; Cho, Y.; Song, X.; Shi, X.; Zhang, S.; Kim, W.; Zeng, H.; Park, J. H., Black phosphorene as a hole extraction layer boosting solar water splitting of oxygen evolution catalysts. *Nature communications* **2019**, *10* (1), 1-10.
8. Zhao, Y.; Zhang, X.; Jia, X.; Waterhouse, G. I. N.; Shi, R.; Zhang, X.; Zhan, F.; Tao, Y.; Wu, L.-Z.; Tung, C.-H.; O'Hare, D.; Zhang, T., Sub-3 nm Ultrafine Monolayer Layered Double Hydroxide Nanosheets for Electrochemical Water Oxidation. *Advanced Energy Materials* **2018**, *8* (18), 1703585.
9. Hou, C.; Yu, H.; Huang, C., Solution-processable $\text{Ti}_3\text{C}_2\text{T}_x$ nanosheets as an efficient hole transport layer for high-performance and stable polymer solar cells. *Journal of Materials Chemistry C* **2019**, *7* (37), 11549-11558.
10. Anasori, B.; Lukatskaya, M. R.; Gogotsi, Y., 2D metal carbides and nitrides (MXenes) for energy storage. *Nature Reviews Materials* **2017**, *2* (2), 1-17.
11. Zhao, X.; Vashisth, A.; Blivin, J. W.; Tan, Z.; Holta, D. E.; Kotasthane, V.; Shah, S. A.;

- Habib, T.; Liu, S.; Lutkenhaus, J. L., pH, nanosheet concentration, and antioxidant affect the oxidation of Ti₃C₂T_x and Ti₂C_{T_x} MXene dispersions. *Advanced Materials Interfaces* **2020**, *7* (20), 2000845.
12. Wu, X.; Wang, Z.; Yu, M.; Xiu, L.; Qiu, J., Stabilizing the MXenes by carbon nanoplating for developing hierarchical nanohybrids with efficient lithium storage and hydrogen evolution capability. *Advanced Materials* **2017**, *29* (24), 1607017.
13. Yang, Y.; Niu, S.; Han, D.; Liu, T.; Wang, G.; Li, Y., Progress in developing metal oxide nanomaterials for photoelectrochemical water splitting. *Advanced Energy Materials* **2017**, *7* (19), 1700555.
14. Xie, X.; Zhang, N.; Tang, Z.-R.; Anpo, M.; Xu, Y.-J., Ti₃C₂T_x MXene as a Janus cocatalyst for concurrent promoted photoactivity and inhibited photocorrosion. *Applied Catalysis B: Environmental* **2018**, *237*, 43-49.
15. Yang, G.; Li, S.; Wang, X.; Ding, B.; Li, Y.; Lin, H.; Tang, D.; Ren, X.; Wang, Q.; Luo, S.; Ye, J., A universal strategy boosting photoelectrochemical water oxidation by utilizing MXene nanosheets as hole transfer mediators. *Applied Catalysis B: Environmental* **2021**, *297*, 120268.
16. Guo, Y.; Zhang, D.; Yang, Y.; Wang, Y.; Bai, Z.; Chu, P. K.; Luo, Y., MXene-encapsulated hollow Fe₃O₄ nanochains embedded in N-doped carbon nanofibers with dual electronic pathways as flexible anodes for high-performance Li-ion batteries. *Nanoscale* **2021**, *13* (8), 4624-4633.
17. Chen, W. Y.; Jiang, X.; Lai, S.-N.; Peroulis, D.; Stanciu, L., Nanohybrids of a MXene and transition metal dichalcogenide for selective detection of volatile organic compounds. *Nature communications* **2020**, *11* (1), 1-10.
18. Hou, T.; Luo, Q.; Li, Q.; Zu, H.; Cui, P.; Chen, S.; Lin, Y.; Chen, J.; Zheng, X.; Zhu, W., Modulating oxygen coverage of Ti₃C₂T_x MXenes to boost catalytic activity for HCOOH dehydrogenation. *Nature communications* **2020**, *11* (1), 1-11.
19. Quiterio, P.; Apolinario, A.; Navas, D.; Magalhaes, S.; Alves, E.; Mendes, A.; Sousa, C. T.; Araujo, J. P., Photoelectrochemical water splitting: Thermal annealing challenges on hematite nanowires. *The Journal of Physical Chemistry C* **2020**, *124* (24), 12897-12911.
20. Annamalai, A.; Lee, H. H.; Choi, S. H.; Lee, S. Y.; Gracia-Espino, E.; Subramanian, A.; Park, J.; Kong, K.-j.; Jang, J. S., Sn/Be sequentially co-doped hematite photoanodes for enhanced photoelectrochemical water oxidation: effect of Be²⁺ as co-dopant. *Scientific reports* **2016**, *6* (1), 1-11.
21. Ruoko, T.-P.; Hiltunen, A.; Iivonen, T.; Ulkuniemi, R.; Lahtonen, K.; Ali-Löytty, H.; Mizohata, K.; Valden, M.; Leskelä, M.; Tkachenko, N. V., Charge carrier dynamics in tantalum oxide overlayers and tantalum doped hematite photoanodes. *Journal of Materials Chemistry A* **2019**, *7* (7), 3206-3215.
22. Zhang, Z.; Karimata, I.; Nagashima, H.; Muto, S.; Ohara, K.; Sugimoto, K.; Tachikawa,

- T., Interfacial oxygen vacancies yielding long-lived holes in hematite mesocrystal-based photoanodes. *Nature communications* **2019**, *10* (1), 1-12.
23. Moir, J. W.; Sackville, E. V.; Hintermair, U.; Ozin, G. A., Kinetics versus charge separation: Improving the activity of stoichiometric and non-stoichiometric hematite photoanodes using a molecular iridium water oxidation catalyst. *The Journal of Physical Chemistry C* **2016**, *120* (24), 12999-13012.
24. Xia, F.; Lao, J.; Yu, R.; Sang, X.; Luo, J.; Li, Y.; Wu, J., Ambient oxidation of Ti₃C₂ MXene initialized by atomic defects. *Nanoscale* **2019**, *11* (48), 23330-23337.
25. Thorne, J. E.; Jang, J.-W.; Liu, E. Y.; Wang, D., Understanding the origin of photoelectrode performance enhancement by probing surface kinetics. *Chemical science* **2016**, *7* (5), 3347-3354.
26. Schnur, S.; Groß, A., Properties of metal–water interfaces studied from first principles. *New Journal of Physics* **2009**, *11* (12), 125003.
27. Ping, Y.; Goddard III, W. A.; Galli, G. A., Energetics and solvation effects at the photoanode/catalyst interface: ohmic contact versus Schottky barrier. *Journal of the American Chemical Society* **2015**, *137* (16), 5264-5267.
28. Pabisiak, T.; Kiejna, A., Incipient adsorption of water and hydroxyl on hematite (0001) surface. *Journal of Physics Communications* **2019**, *3* (3), 035023.
29. Liu, G.; Zhao, Y.; Wang, K.; He, D.; Yao, R.; Li, J., Ultrasmall NiFe-phosphate nanoparticles incorporated α -Fe₂O₃ nanoarrays photoanode realizing high efficient solar water splitting. *ACS Sustainable Chemistry & Engineering* **2018**, *6* (2), 2353-2361.
30. Wang, G.; Wang, B.; Su, C.; Li, D.; Zhang, L.; Chong, R.; Chang, Z., Enhancing and stabilizing α -Fe₂O₃ photoanode towards neutral water oxidation: Introducing a dual-functional NiCoAl layered double hydroxide overlayer. *Journal of Catalysis* **2018**, *359*, 287-295.
31. Mo, R.; Liu, Q.; Li, H.; Yang, S.; Zhong, J., Photoelectrochemical water oxidation in α -Fe₂O₃ thin films enhanced by a controllable wet-chemical Ti-doping strategy and Co–Pi co-catalyst modification. *Journal of Materials Science: Materials in Electronics* **2019**, *30* (24), 21444-21453.
32. Li, M.; Liu, T.; Yang, Y.; Qiu, W.; Liang, C.; Tong, Y.; Li, Y., Zipping up NiFe(OH)_x-encapsulated hematite to achieve an ultralow turn-on potential for water oxidation. *ACS Energy Letters* **2019**, *4* (8), 1983-1990.
33. Walsh, D.; Zhang, J.; Regue, M.; Dassanayake, R.; Eslava, S., Simultaneous Formation of FeO_x Electrocatalyst Coating within Hematite Photoanodes for Solar Water Splitting. *ACS Applied Energy Materials* **2019**, *2* (3), 2043-2052.
34. Wei, Y.; Liao, A.; Wang, L.; Wang, X.; Wang, D.; Zhou, Y.; Zou, Z., Room temperature surface modification of ultrathin feooh cocatalysts on Fe₂O₃ photoanodes for high photoelectrochemical

water splitting. *Journal of Nanomaterials* **2020**, 2020.

35. Xiao, J.; Fan, L.; Huang, Z.; Zhong, J.; Zhao, F.; Xu, K.; Zhou, S.-F.; Zhan, G., Functional principle of the synergistic effect of co-loaded Co-Pi and FeOOH on Fe₂O₃ photoanodes for photoelectrochemical water oxidation. *Chinese Journal of Catalysis* **2020**, 41 (11), 1761-1771.

36. Wang, H.; Zhang, R.; Li, Y. Y.; Wang, D.; Lin, Y.; Xie, T., Simple electrodeposition to synthesize a NiFeS_x-modified Ti-Fe₂O₃ photoanode: an effective strategy to improve the photoelectrochemical water oxidation reaction. *Dalton Transactions* **2021**, 50 (43), 15551-15557.

37. Singh, A.; Tejasvi, R.; Karmakar, S.; Basu, S., α -Fe₂O₃ nanorods decorated with NiMnO₃ co-catalyst as photoanode for enhanced oxygen evolution reaction in photoelectrochemical water splitting. *Materials Today Communications* **2021**, 27, 102231.

38. Kim, J. H.; Lee, N. K.; Kim, H. W.; Pan, Z.; Sohn, W. Y., Sequential Modifications of the Surface of Hematite (α -Fe₂O₃) Photoanodes with Amorphous Nickel Iron Oxide (NiFeO_x) and Cobalt Phosphate (Co-Pi). *Journal of Photochemistry and Photobiology A: Chemistry* **2022**, 114478.

Acknowledgements

길다면 길고 짧다면 짧았던 박사 학위 과정을 마치게 되었습니다. 이 한 부분을 빌려 저를 도와 주신 모든 분께 감사의 인사 전합니다.

먼저 학부 과정부터 박사과정 마무리까지 값진 지도와 가르침을 주신 장지현 지도교수님께 감사드립니다. 교수님의 가르침을 이정표 삼아 이제 한 명의 연구자로서 나아가도록 하겠습니다. 또한, 바쁘신 와중에도 논문 심사에 참여해 주신 김진영 교수님, 박종남 교수님, 류정기 교수님, 장지욱 교수님께도 감사의 말씀을 드립니다.

학위 과정 중 기쁜 일과 힘든 일을 함께하고 저의 부족함을 채워주었던 연구실 사람들, 김선이 박사님, 김광현 박사님, 윤기용 박사님, 곽명준 박사님, Aninyda 박사님, Balaji 박사님, Sourav, Bibhuti, 두진이형님, 종철이형, 종하형, 경남이형, 지훈이형, 성지누나, 현민, 진호, 민경 모두에게 감사 인사를 드립니다.

긴 시간 동안 희로애락을 함께했던 양천고 친구들, 동한, 기욱, 경훈, 진규, 승민, 원준, 재성, 민수 그리고 12학번 동기들, 정환, 성식, 용준, 경렬, 상수, 정우, 성경, 동현에게도 정말 고맙다고 말하고 싶습니다. 고민이 있거나 힘든 일이 있을 때 큰 버팀목이 되었습니다. 또한, 우연한 계기로 시작해 지금은 나의 인생에 떨 수 없는 운동으로 자리매김한 테니스를 같이하였던 권봉석 교수님, 원경이형, 승민이형, 호영이형, 진수, 성진, 우진, 동현, 정훈, 문진 등 모든 유니스트 테니스 클럽 사람들에게 감사의 인사를 드립니다. 운동을 통해 긍정적인 에너지와 좋은 추억을 많이 쌓을 수 있어 정말 행복했습니다.

마지막으로 저의 생활을 지탱해 준 우리 가족들에게 깊은 감사의 말을 전합니다. 못난 아들을 위해 모든 것을 내어주시고 지지해 준 아버지와 어머니 덕분에 학위를 잘 마무리하였습니다. 언제나 학위를 한다는 핑계로 가족에게 소홀했던 저를 대신해 몇 배로 힘써주고 고생했던 누나에게도 고맙고 항상 미안한 마음을 전합니다.

끝으로, 나의 모든 일들을 함께 도와주었던 모든 분에게 다시 한번 깊은 감사의 말씀을 전합니다.

2023년 6월 8일

박주형 드림

